AD NUMBER

ADB036761

NEW LIMITATION CHANGE

TO
Approved for public release, distribution unlimited

FROM
Distribution authorized to U.S. Gov't. agencies only; Test and evaluation; Oct 1978. Other requests shall be referred to AFAPL/POD, Wright-Patterson AFB, OH, 45433.

AUTHORITY

AFAPL ltr, 7 Aug 1979

AFAPL-TR-78-107

LEVEL Ⅱ

NEAR INFRARED GAS LASERS

S. LAWTON
T. A. DeTEMPLE

UNIVERSITY OF ILLINOIS
DEPARTMENT OF ELECTRICAL ENGINEERING
URBANA, ILLINOIS 61801

DDC
RECEIVED
MAY 7 1979
C
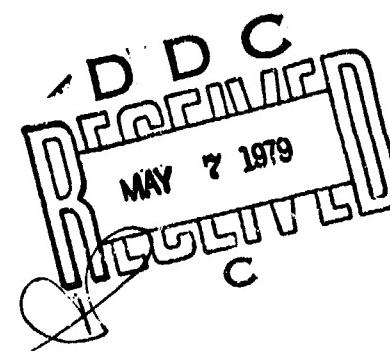
DECEMBER 1978

TECHNICAL REPORT AFAPL-TR-78-107
Final Report 1 March 1976 — 30 September 1978

AIR FORCE WRIGHT AERONAUTICAL LABORATORIES
AIR FORCE SYSTEMS COMMAND
AIR FORCE AERO PROPULSION LABORATORY
WRIGHT-PATTERSON AIR FORCE BASE, OHIO 45433

79 05 03 113

NOTICE

When Government drawings, specifications, or other data are used for any purpose other than in connection with a definitely related Government procurement operation, the United States Government thereby incurs no responsibility nor any obligation whatsoever; and the fact that the government may have formulated, furnished, or in any way supplied the said drawings, specifications, or other data, is not to be regarded by implication or otherwise as in any manner licensing the holder or any other person or corporation, or conveying any rights or permission to manufacture, use, or sell any patented invention that may in any way be related thereto.

This technical report has been reviewed and is approved for publication.
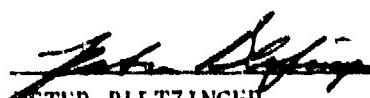
PETER BLETZINGER
Project Engineer

PHILIP E. STOVER
Chief, High Power Branch
Aerospace Power Division

FOR THE COMMANDER
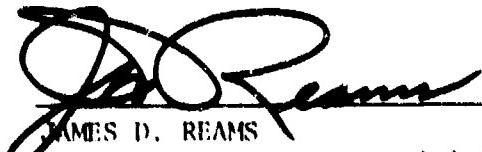
JAMES D. REAMS
Chief, Aerospace Power Division
AF Aero Propulsion Laboratory

If your address has changed, if you wish to be removed from our mailing list, or if the addressee is no longer employed by your organization please notify AFAPL/POD-2, W-PAFB, OH 45433 to help us maintain a current mailing list.

Copies of this report should not be returned unless return is required by security considerations, contractual obligations, or notice on a specified document.

AIR FORCE/56780/6 April 1979 — 160

REPORT DOCUMENTATION PAGE	READ INSTRUCTIONS BEFORE COMPLETING FORM

1. REPORT NUMBER	2. GOVT ACCESSION NO.	3. RECIPIENT'S CATALOG NUMBER
AFAPL-TR-78-107		

4. TITLE (and Subtitle)

NEAR INFRARED GAS LASERS.

5. TYPE OF REPORT & PERIOD COVERED

Final
1 Mar 1976-30 Sep 1978

6. PERFORMING ORG. REPORT NUMBER

7. AUTHOR(s)	8. CONTRACT OR GRANT NUMBER(s)
S. A. Lawton — T. A. DeTemple	F33615-76-C-2089

9. PERFORMING ORGANIZATION NAME AND ADDRESS	10. PROGRAM ELEMENT, PROJECT, TASK AREA & WORK UNIT NUMBERS
University of Illinois Dept. of Electrical Engineering Urbana, IL 61801	Program Element: 62203F Proj/Task/W.U.: 2301S217

11. CONTROLLING OFFICE NAME AND ADDRESS	12. REPORT DATE
	December 78
	13. NUMBER OF PAGES
	152

14. MONITORING AGENCY NAME & ADDRESS(if different from Controlling Office)	15. SECURITY CLASS. (of this report)
Air Force Aero Propulsion Lab/POD-2 Wright-Patterson AFB, OH 45433	UNCLASSIFIED
	15a. DECLASSIFICATION/DOWNGRADING SCHEDULE

16. DISTRIBUTION STATEMENT (of this Report)

Distribution limited to U.S. Government agencies; test and evaluation; October 1978. Other requests for this document must be referred to AFAPL/POD, Wright-Patterson AFB, OH 45433

17. DISTRIBUTION STATEMENT (of the abstract entered in Block 20, if different from Report)

18. SUPPLEMENTARY NOTES

19. KEY WORDS (Continue on reverse side if necessary and identify by block number)

Rare Gas Lasers	Line Profiles	Free Carrier Absorption
Argon-Xenon	Discharge Modeling	Metastable Densities
Helium-Xenon	Boltzmann Code	Recirculation Pumping
Electron Beam Pumped	Ar-Xe Reactions	
Xenon Energy Levels	He-Xe Rate Constants	

20. ABSTRACT (Continue on reverse side if necessary and identify by block number)

The near infrared laser emission from Xe in Ar and He mixtures has been investigated experimentally, in a ionizer-sustainer mode, and theoretically. An efficiency of 1.3% has been achieved from Ar:Xe, 150:1, at 1900 torr with approximately 75% of the output occurring on a single line at 1.73 microns; the efficiency for He:Xe being approximately a factor-of-ten lower with the dominant emission at 2.03 microns and 3.43 microns. Based on a detailed

DD FORM 1473 EDITION OF 1 NOV 65 IS OBSOLETE

kinetic study of the discharge, the strong laser emission in Ar:Xe is attributed to a two-stage excitation in which a large excited state population is created during the first portion of the discharge followed by excitation and ionization of these excited states with subsequent strong lasing during the remaining, low field, portion. The processes leading to strong emission include electron impact excitation from low lying excited states, dissociative recombination and cascade pumping from higher lying levels; all of which mean that the original metastable excitation energy is being recirculated. The He:Xe mixtures appear dominated by dissociative recombination pumping. The desired high Ar pressure is explained on the basis of providing an impedance match to the sustainer circuit and because the elastic (momentum) losses, at low fields (E/N) are nominal allowing a small excited state density to dominate the fractional loss spectra.

PREFACE

TABLE OF CONTENTS

LIST OF ILLUSTRATIONS

LIST OF TABLES

SECTION I

INTRODUCTION

Investigations of high pressure rare gas systems have shown that they can be relatively efficient sources of laser emission on the rare gas atomic transitions. The xenon atom is of particular interest in this respect since a number of atomic transition lines fall within the atmospheric transmission windows between 1.7 and 4 microns.

In the rare gas atoms the radiative lifetimes of the lowest p states are about an order of magnitude shorter than the lifetimes of the lowest d levels, and it is therefore a straightforward process to invert the populations and achieve lasing on the d to p transitions. As a result, lasing on these transitions was observed in early investigations of low pressure CW and pulsed discharges.

Targ and associates[1,2] initiated the high pressure studies in atomic xenon. They were primarily interested in obtaining high average powers and were able to obtain 10 watts from corona preionized discharges operating at 1 kHz. The single pulse energy on their systems was only 9 mJ however, and they confined their investigations to helium/xenon mixtures.

Chapovsky et al.[3] investigated high pressure discharges in rare gas mixtures in a TEA laser configuration. They observed lasing in mixtures of argon and xenon but reported no laser

1

energy measurements except to note that the maximum output occurred at about one atmosphere total pressure.

Olson and Grosjean[4] have investigated lasing in both helium/xenon and argon/xenon mixtures in a closed cycle, U-V preionized discharge configuration. The highest energy pulses, 3 mJ, were reported for argon/xenon mixtures.

Newman and DeTemple[5] have investigated lasing in helium/xenon and argon/xenon mixtures in e-beam preionized discharges at pressures up to 1 atmosphere. These low pressure measurements indicated that higher energies per pulse can be obtained in argon-xenon than in helium-xenon mixtures. The measurements also indicated that pulse energies in excess of 100 mJ at efficiencies of better than 1% could be obtained at pressures in excess of one atmosphere.

In this report we describe the results of continuing these latter investigations at pressures up to 4 atmospheres. Since argon/xenon mixtures yield higher laser powers and higher efficiencies than helium/xenon mixtures at these pressures, our efforts have been directed at understanding the characteristics of the argon/xenon laser. In Section 2 we summarize the experimental measurements: the laser power vs mixture and pressure, the time dependence of the energy in individual laser laser lines and of the fluorescence from the discharge, and the free electron density. Section 3 deals with our

modeling of the argon/xenon discharge and summarizes our
understanding of the kinetics of the argon/xenon system. The
results of our investigations into lasing in helium/xenon
mixtures is presented in Section 4, while Section 5 summarizes
all of our results and suggests methods for improving the
atomic xenon lasers.

SECTION II

EXPERIMENTAL RESULTS

2.1 Apparatus

The apparatus, shown schematically in Figure 1, consists
of an electron beam source, a high pressure discharge cavity
and a sustainer voltage supply. The source of the preionizing
electron beam is a cold-cathode gun which supplies a 200 nsec
pulse of 150 kV electrons at 250 amperes. The electrons enter
the laser cavity through a 13 micron thick titanium foil sup-
ported on a 'Hibatchi' type structure and pass through 1.3 cm
of the target gas to a semitransparent copper mesh cathode
which is separated by 3 cm from a profiled aluminum anode. The
transverse sectional dimensions of the electron beam inside the
cavity are approximately 100 cm $\times$ 2 cm.

At a variable time, typically 100-300 nanoseconds, after
e-beam preionization, a sustainer voltage is applied to the
anode through a low-inductance vacuum feedthrough. The return
path for the resulting discharge current is through the grounded
aluminum vacuum wall.

The sustainer supply is either a low inductance 0.64 μF
capacitor or a parallel arrangement of fifteen 3600 pf 'door-
knob' capacitors. The capacitors are spark-gap switched onto
the laser and the resulting discharge current is monitored
with a Pearson wide-band current transformer with a response
of .1 volt/amp and a frequency response to 35 MHz.

4

IONIZER-SUSTAINER APPARATUS

e-beam aperture

e-beam

Anode

Feed-Thru

Mesh cathode

Ti-Foil

⊘ Delrin

▦ Brass

■ 'O'-Ring
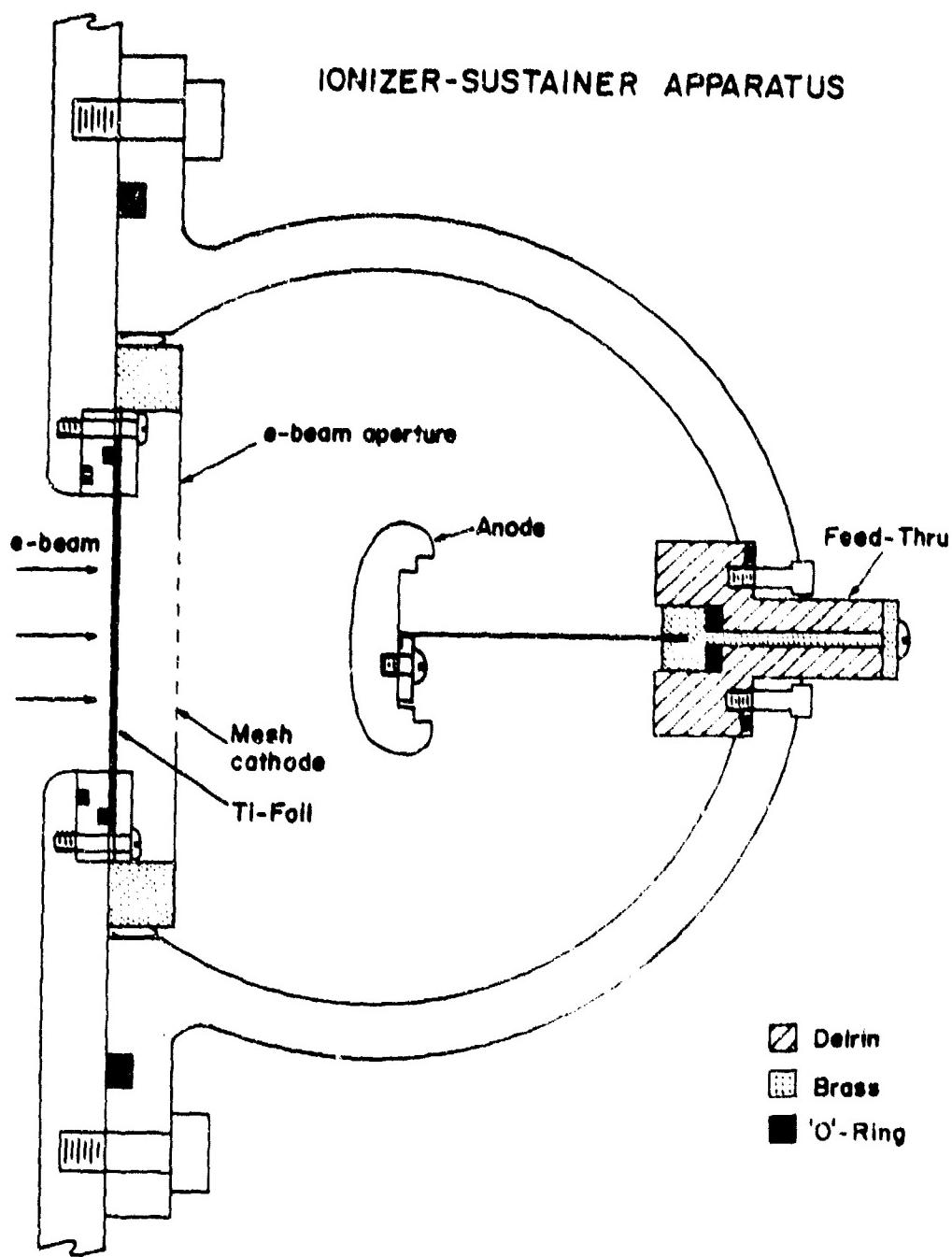
Figure 1.   Cross section through laser discharge chamber.

5

The discharge voltage, taken to be the potential between the feedthrough outside the vacuum and the aluminum vacuum wall at the base of the capacitors, is measured with a Tektronix P-6015, 1000x high voltage probe, which has a frequency response to 75 MHz. Single shot pulses were observed on a 100 MHz storage oscilloscope (Tektronix 466).

For some measurements illustrated in this report, eight 3600 pf doorknob peaking capacitors were placed across the discharge, that is, outside the vacuum wall and between the feedthrough and ground. These capacitors were ultimately shown to have no significant effect on the laser output energy.

Research grade xenon (99.995%), high purity argon (99.996%) and helium (99.995%) are mixed in a bomb for 24 hours and used without further purification. The laser cavity can be evacuated to $<7 \times 10^{-5}$ torr although the pressure will rise rapidly due to outgassing from the surfaces when the system is sealed. The laser mixture is held statically in the cell until the laser output degrades below a useful level. In addition to power degradation arising from the holding time the power degrades $\sim 10\%$ after 50 pulses.

The laser cavity is formed at one end by a 4 meter radius of curvature aluminum mirror and at the output end by an uncoated quartz flat (Infrasil) which transmits radiation out to 4 μm as measured with an IR spectrometer. If an uncoated

6

silicon flat is used as an output coupler the laser output energy is observed to increase by $\sim$ 10% indicating large gains and efficient saturation with the use of the Infrasil mirror.

In order to enhance the gain on transitions other than the very strong 1.73 μm, a Jobin-Yvon grating blazed at 3.7 μm can be inserted in the vacuum cavity to replace the gold back reflector. It is only by using this grating that the weak 3.3676 μm, $5d(5/2)_2 - 6p(3/2)_1$ transition can be observed.

The energy in a laser pulse is measured with a pyroelectric joulemeter (Gentec ED-500), and the pulse shapes are observed with a Au:Ge detector with $\sim$ 10 nsec rise time. A one meter spectrometer with a grating blazed at 3.75 μm allows selection of laser wavelengths for identification and separate time domain studies.

In order to determine the laser efficiency it is necessary to know the energy initially stored in the sustainer capacitor. The stored energy was determined by discharging the capacitor through a low impedance switch and a 155 ohm load resistor. The power dissipated in the resistor was determined from voltage and current measurements and was integrated to obtain the total energy. This technique was used only for the doorknob capacitors which had a nonlinear C-V response.

In order to determine the LRC parameters of the external discharge circuit a wide, low inductance copper shorting strap

7

is used to short the vacuum feedthrough to ground, thereby bypassing the discharge, and the laser gas was removed. The LRC characteristics of this circuit consisting of the sustainer capacitor, spark-gap, and ground return indicate a 300 mΩ resistance and 140 nH inductance in series with the capacitor. These RL values can be ascribed to the sparkgap, the connecting straps and the dynamic resistance of the capacitors.

2.2   Atomic Xenon Laser Lines

The atomic xenon lines which we have observed to lase are shown in Figure 2. In helium/xenon mixtures the dominant laser transition is $5d(3/2)_1$ - $6p(3/2)_1$ at 2.02 μm whereas in argon/ xenon mixtures the $5d(3/2)_1$ - $6p(5/2)_2$ transition at 1.73 μm dominates. Table 1 illustrates the relative line strengths which we observe in xenon mixtures with helium and argon. Also tabulated are the branching ratios calculated in the Coulomb approximation of Bates and Damgaard, as described later in this report.

It is clear from this table that the most intense laser lines originate from the $5d(3/2)_1$ levels in both argon and helium/xenon mixtures. This is not particularly surprising since the $5d(3/2)_1$ level is one of the two 5d levels with electric dipole allowed transitions to the xenon ground state. Since transitions with large electric dipole moments generally have relatively large electron excitation cross sections, one

8
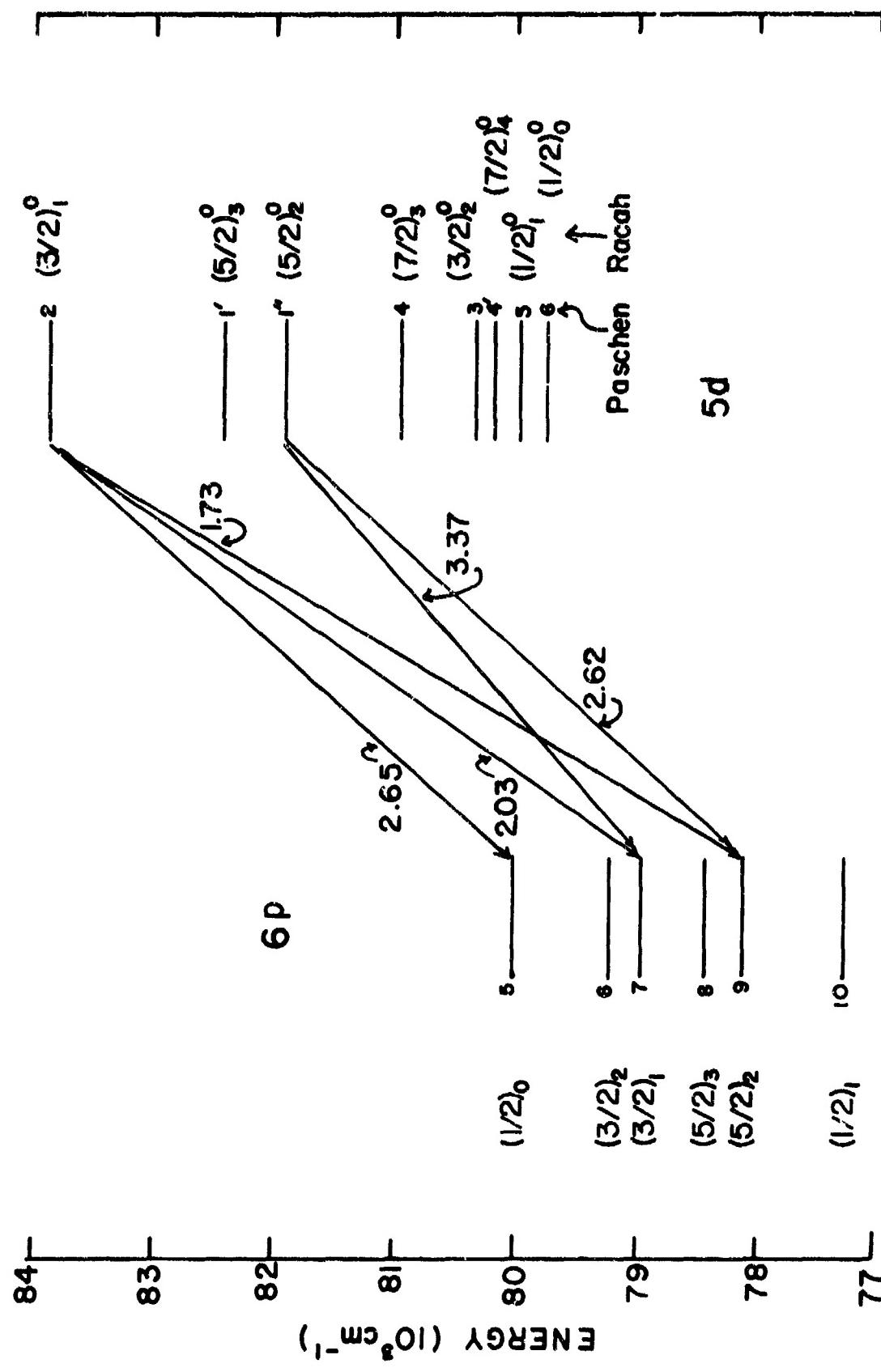
Figure 2.   Enlargement of the 5d and 6p states of Xe. The states are classified by both the Paschen and Racah notation. Observed laser transitions and corresponding wavelength (μm) are indicated.

TABLE 1

HELIUM AND ARGON/XENON LASER TRANSITIONS

TRANSITION	λ (μm)	BRANCHING RATIO	RELATIVE INTENSITY He/Xe	Ar/Xe
$5d(3/2)_1^\circ$ to $6p(1/2)_1$	1.51	.288	–	–
$(5/2)_2$	1.73	.073	–	.75
$(3/2)_1$	2.03	.434	.65	$.03^*$
$(3/2)_2$	2.14	.075	–	–
$(1/2)_0$	2.65	.130	.04	$.06^*$
$5d(5/2)_2^\circ$ to $6p(5/2)_3$	2.84	.026	–	–
$(5/2)_2$	2.62	.445	–	.15
$(3/2)_1$	3.37	.488	–	$WEAK^+$
$(3/2)_2$	3.68	.042	–	–
$7p(5/2)_2$ to $7s(3/2)_1^\circ$	3.43	.433	.23	–
$7p(1/2)_1$ to $7s(3/2)_2^\circ$	3.65	.473	.08	–

[+]Observed only with grating as back reflector.

[*]Will lase on e-beam alone at low pressures in Ar/Xe.

would expect an enhanced population in $5d(3/2)_1$ if the level is populated by electron impact excitation of xenon. Similarly one would expect that the population of the $5d(3/2)_1$ level would be enhanced if the 5d manifold were populated by energy transfer from some other excited species in the gas, Ar_2^* for example, since the lowest order rate constant for the transfer process is proportional to the dipole moment connecting the initial and final states.

The only other state of the 5d manifold which has an allowed electric dipole transition to the ground state is the $(1/2)_1$ level. Laser transitions can occur from $5d(1/2)_1$ to the $(1/2)_1$, $(3/2)_1$ and $(3/2)_2$ levels of the 6p manifold at 3.68 μm, 9.71 μm and 12.9 μm respectively. It is unlikely that the 3.68 μm transition, which has the largest branching ratio, would lase since the $6p(1/2)_1$ level is rapidly populated by collisional energy transfer from the 6s' levels.[6] The two longer wavelength transitions would be unlikely to lase since our electron density measurements, which are discussed later, indicate a large free carrier absorption of radiation beyond 4 μm.

From the wavelengths and branching ratios in Table 1 we can calculate that the gain on the 2.03 μm line should be approximately 8 times larger than that on 1.73 μm assuming equal broadening rates. Thus one would not anticipate that the 1.73 μm would dominate in the Ar/Xe discharge unless the lower level

11

populations were perturbed in such a manner as to suppress
the 2.03 μm transition. In our discussion f the fluorescence
measurements we will note the possibili that the 6p to 6s
transitions are radiatively trapped. In this case some other
mechanism must depopulate the lower laser levels. Such a mech-
anism could be three-body formation of a state of Xe_2^{**} or $ArXe^{**}$
which would predissociate to the 6s state of the atom. Such
predissociative states have been invoked to explain the de-
crease in fluorescence from Xe^{**} states in high pressure ex-
cimer lasers. Indeed, Mulliken's[7,8]calculations of the
potential energy curves of Xe_2^{**} indicate that the lowest two
6p levels, including the $(5/2)_2$ will form predissociative Xe_2^{**}
states whereas the higher 6p levels, including the $(3/2)_1$ will
not. Thus there is a mechanism which will afford a selective
quench of the 1.73 μm lower level.

2.3   Pressure Dependence of Ar/Xe Laser Output

2.3.1   Total Pulse Energy

Measurements were made of the dependence of the output
energy, on all lines, as a function of total pressure and ratio
of argon to xenon. The results for pressures below 1 atmos-
phere have been reported previously[5] and we note simply that
for low pressures the optimal energy output occurs for Ar/Xe
ratios of ᷉ 50:1. Figure 3 indicates the results at higher
pressures for a sustainer capacitor voltage of 27 kV. The

12

Ar/Xe LASER OUTPUT
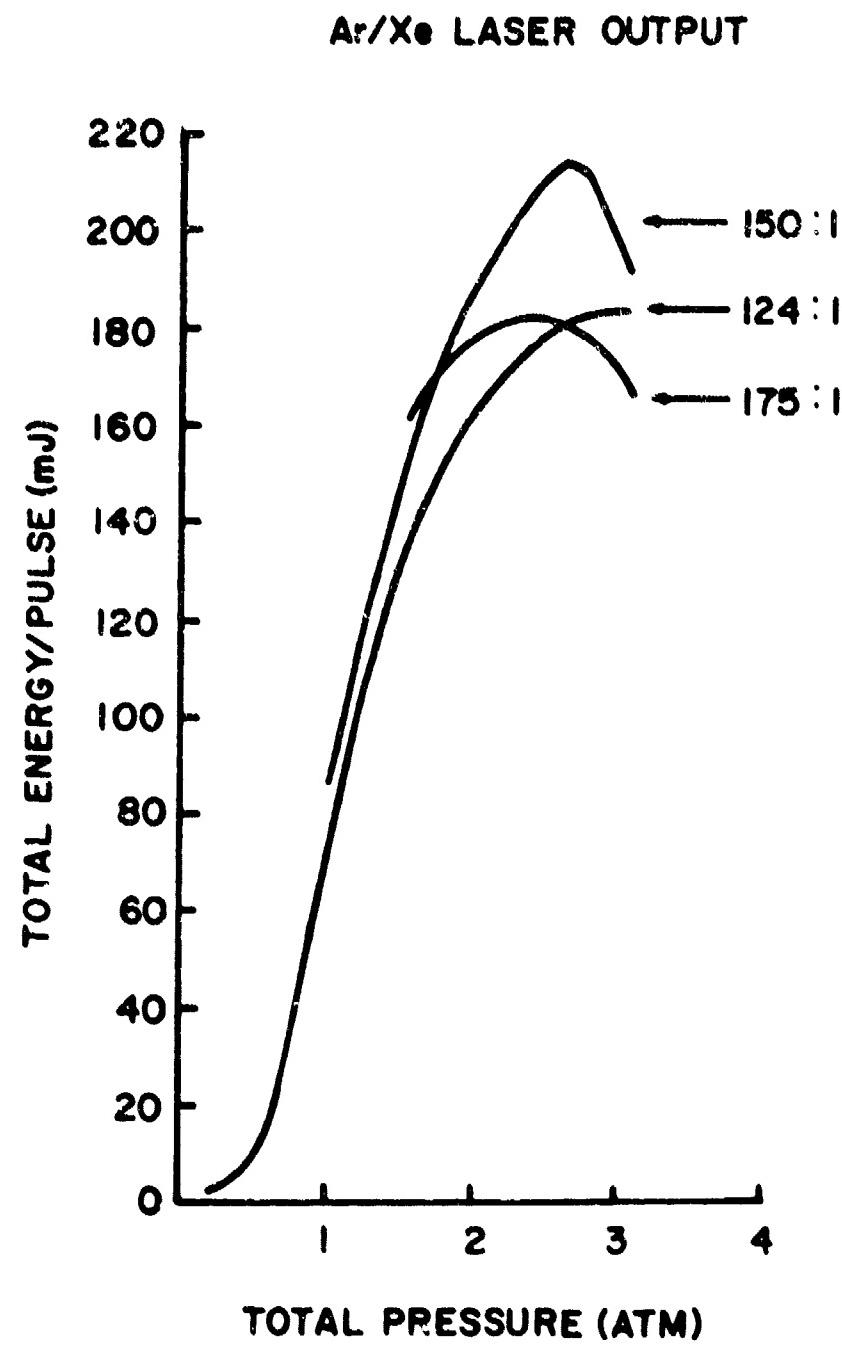
Figure 3. Output versus pressure for Ar-Xe, 27 kV sustainer, for various ratios of Ar:Xe.

optimum output energy of 210 mJ is achieved with a 150:1 ratio
of Ar:Xe at 2.5 atm (1900 torr) total pressure. Under these
conditions the e-beam deposits $\sim$ 2.5 joules of energy while
the sustainer capacitor can supply 13.5 joules. If the energy
lost in the 300 mΩ series resistor is neglected, the efficiency
at the optimum pressure is 1.3%. Preliminary modeling of the
discharge indicates that about half of the sustainer power may
be dissipated in the external circuit so that the true ef-
ficiency is probably 2.5%, or about a third of the 7% quantum
efficiency for the 1.73 μm transition. Such a large efficiency
suggests that some mechanism other than direct excitation of
the ground state may lead to excitation of the laser levels.

If the sustainer voltage is increased the output energy
increases, although the efficiency decreases. For a 34 kV
sustainer voltage a quarter joule output has been attained
at 3/4% efficiency at 1900 torr. We attempted to increase
the laser efficiency by halving the discharge length, thereby
doubling the discharge impedance with respect to the
external circuit resistance. However since the impedance of
the sparkgap, which is one source of the external impedance,
is inversely proportional to the current, the sparkgap imped-
ance doubled when the discharge impedance doubled and the rela-
tive power lost to the external circuit and discharge remained
fixed. Thus the observed efficiency remained constant.

14

The lasing observed in He:Xe mixtures is weak compared to Ar:Xe and shows no marked dependence upon either relative or total pressures. The energy per pulse is essentially unchanged for ratios of 124:1 or 175:1 of helium to xenon. The output energy peaks broadly at 15 mJ at approximately 2 atm total pressure resulting in a lasing efficiency of $\sim$ .1%.

2.3.2 Line Profiles

Figures 4 to 7 illustrate the pressure dependence of the temporal output for four of the laser lines. All of these curves were taken with the secondary capacitors across the discharge. The presence of the secondaries causes an initial pronounced peak to occur when the sustainer discharge is switched on. This peak is significantly reduced or disappears if the secondaries are removed, as can be seen by comparing Figure 4 with Figure 10 for which the secondaries were removed.

A small transient, which occurs in each trace at the time when the e-beam was triggered, allows one to determine the timing sequence for each pulse. For example, on the 1.73 µm curve at 1.8 atmospheres the e-beam fires 400 nsec into the trace. Since the e-beam is 200 nsec in duration, there is a 200 nsec delay between the end of the e-beam and the triggering of the sustainer voltage, at which time the power output rises rapidly.

15

1.73 μm
.2 μsec/div.
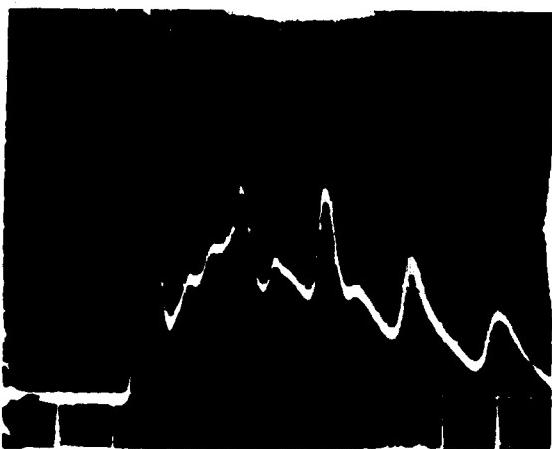
1.0 ATM   .5V/div.   1.8 ATM   IV/div.
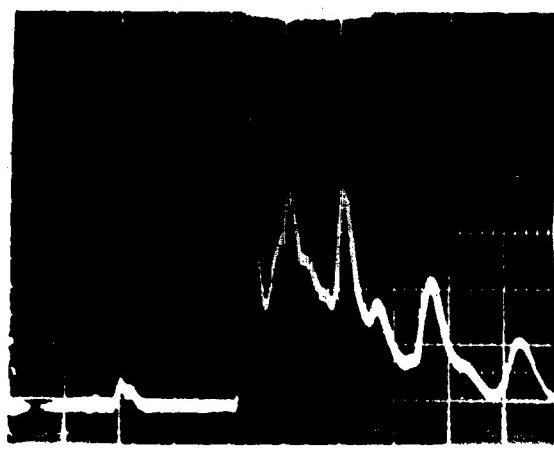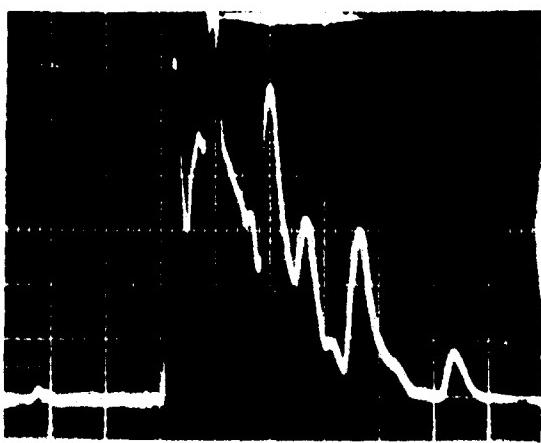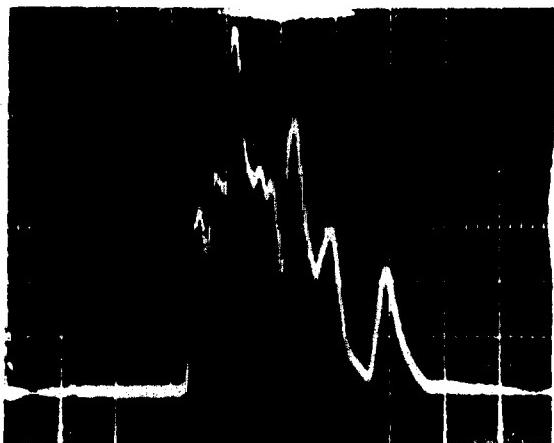
2.5 ATM   IV/div.   3.0 ATM   IV/div.

Figure 4.   Pressure dependence of 1.73 μm radiation for 150:1
            mixture of Ar/Xe, 27 kvolt sustainer and with the
            secondary capacitors.

2.65 μm

.2 μsec/div.

1.0 atm.   .05 V/div.   1.8 atm.   .1 V/div.

2.5 atm.   .2 V/div.   3.0 atm.   .2 V/div.

Figure 5.   Pressure dependence of 2.65 μm radiation for 150:1
            mixture of Ar/Xe, 27 kvolt sustainer and with the
            secondary capacitors.

2.03 μm
.2 μsec/div.
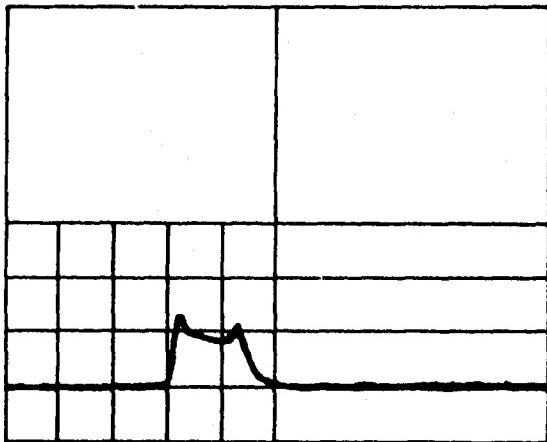
1.0 ATM   .05V/div.
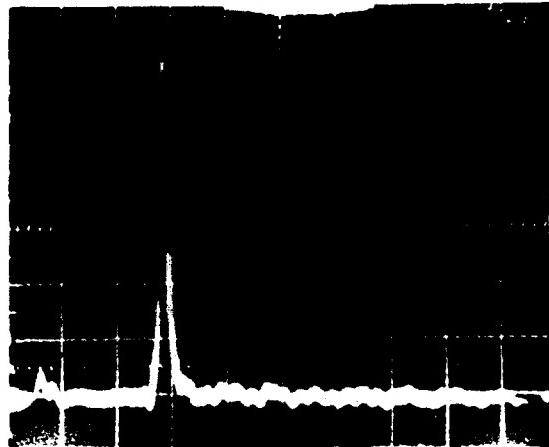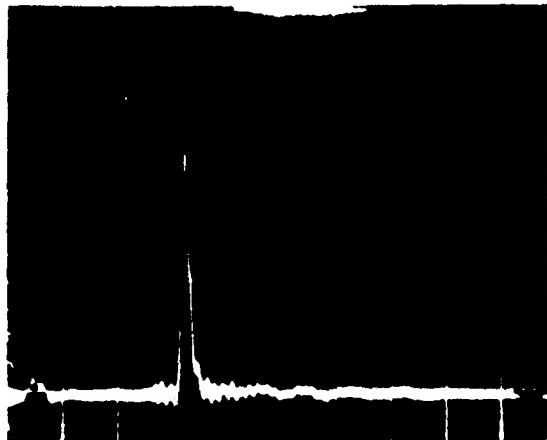
1.8 ATM   .1V/div.

2.5 ATM   .5V/div.
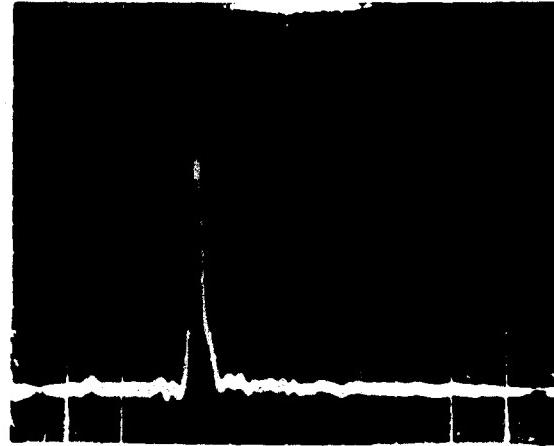
3.0 ATM   .5V/div.

Figure 6.   Pressure dependence of 2.03 μm radiation for 150:1 mixture of Ar/Xe, 27 kvolt sustainer and with the secondary capacitors.

2.62 μm

.2 μsec/div.
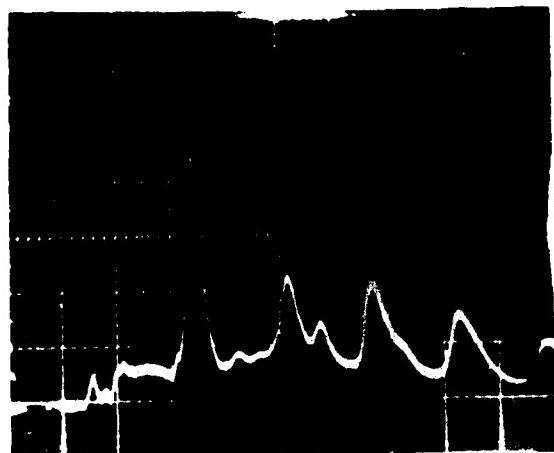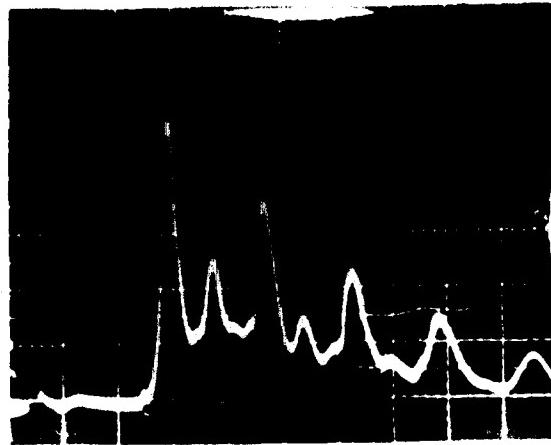
1.0 ATM   .1V/div.   1.8 ATM   .2V/div.
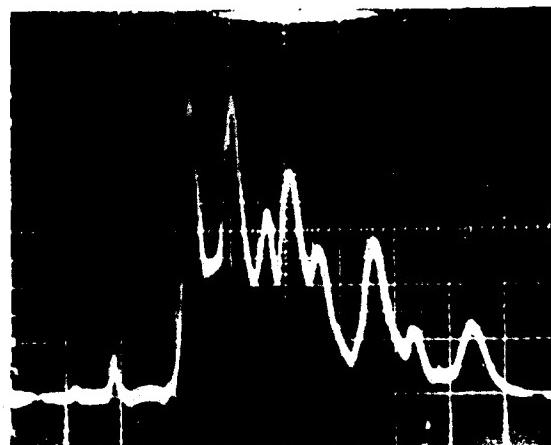
2.5 ATM   .2V/div.   3.0 ATM   .2V/div.

Figure 7.   Pressure dependence of 2.62 μm radiation for 150:1 mixture of Ar/Xe, 27 kvolt sustainer and with the secondary capacitors.

Two lines, 2.65 μm and 2.62 μm are observed to lase on
e-beam excitation alone, but only at pressures below ∿ 1.8
atm. The 1.73 μm transition, although dominant with a sus-
tainer discharge, does not lase with e-beam excitation alone.

The most noticeable characteristic of the laser output
during the sustained discharge is the repetitive series of
large peaks. The 2.65 μm curves at low pressures indicate
the presence of a single series of peaks spaced at ∿ 300 nsec
intervals. These peaks are presumably present at the higher
pressures but are lost in the noise. From the 2.62 μm and 1.73
μm curves it can be seen that a second, smaller series of peaks
is also present at the higher pressures. This second series of
peaks also has a spacing of ∿ 300 nsec. As the pressure in-
creases the relative size of these second-series peaks in-
creases so that at 2.5 atm. they dominate the first series and
at 3 atm. they rival the initial peak. The amplitudes of both
series of peaks at larger times decreases for pressures above
2 atm. and, as a result, the pulse compresses in time.

The behavior of the 2.03 μm transition is unique in that
there is no lasing following the single initial sustainer peak.
If the secondary capacitors are removed the single peak is re-
duced significantly and virtually no lasing is observed.

2.3.3 Voltage and Current Profiles

Figures 8 and 9 illustrate the pressure dependence of
the voltage and current profiles. For the current profiles

20
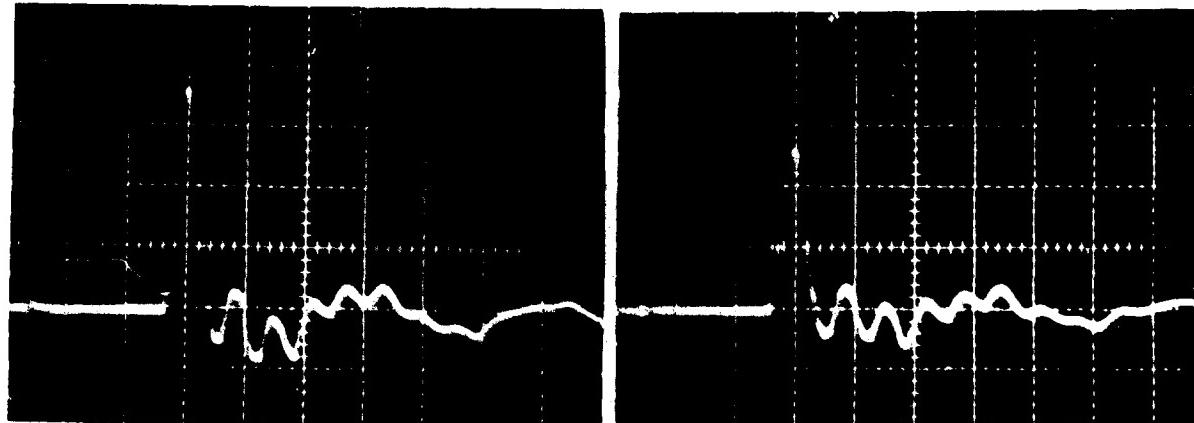
VOLTAGE

.2 μsec/div.

1.0 ATM   2 KV/div.   1.8 ATM   5 KV/div.
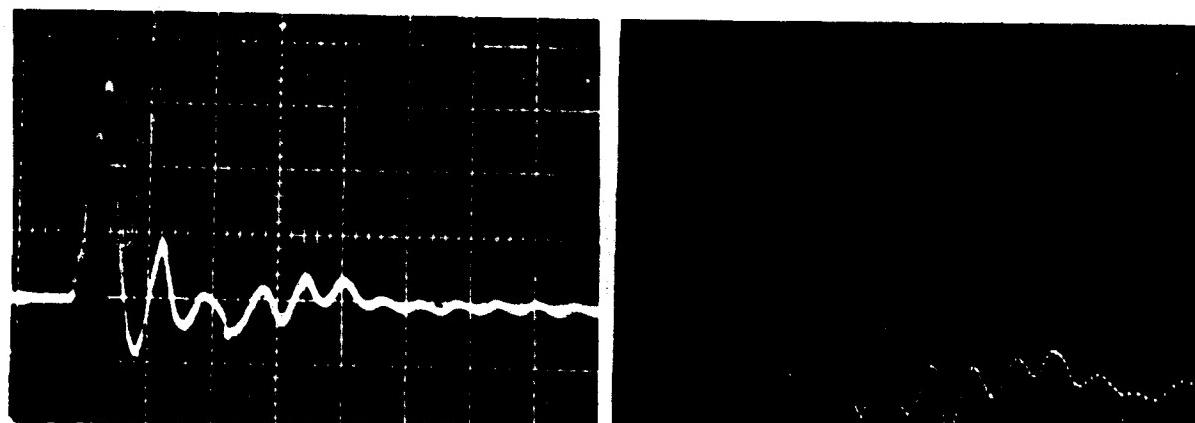
2.5 ATM   5 KV/div.   3.0 ATM   5 KV/div.

Figure 8. Voltage across laser electrodes vs. pressure for 150:1 mixture of Ar/Xe, 27 kV sustainer and with the secondary capacitors.

CURRENT

.2 μsec/div.
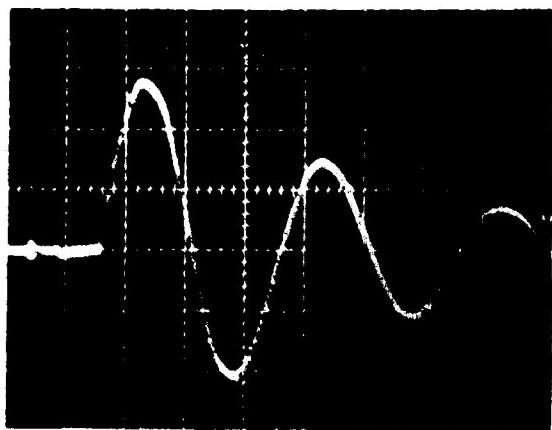
1.0 ATM   5 KA/div.
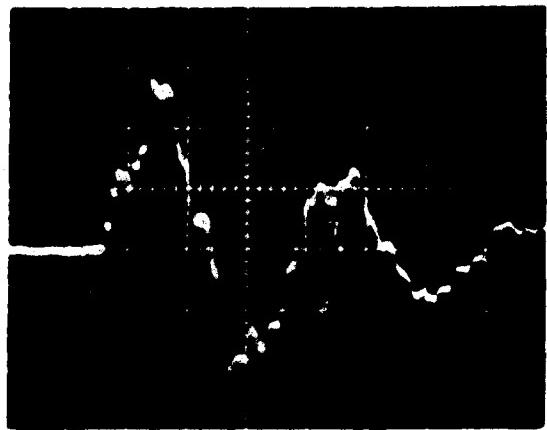
1.8 ATM   5 KA/div.

2.5 ATM   5 KA/div.
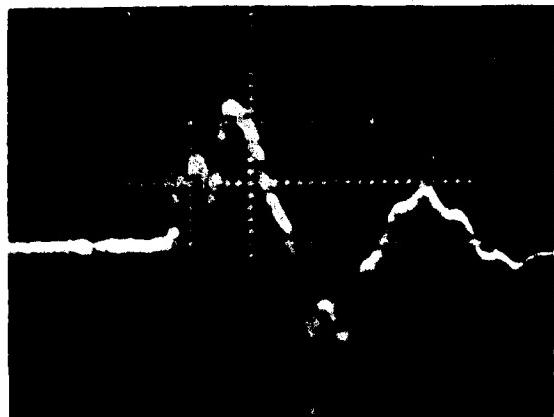
3.0 ATM   5 KA/div.

Figure 9.   Current through gas as a function of pressure for
            150:1 mixture of Ar/Xe, 27 kV sustainer and with
            the secondary capacitors.

22

smooth curves could be obtained periodically for pressures below 2 atm. At higher pressures the profiles become very irregular, although the modulations were reproducible.

The low pressure current curve resembles that for the current in a LRC circuit. From this curve it is possible to calculate the bulk circuit parameters. The net series impedance is 350 mΩ, which is dominated by the external circuit and the net inductance is 140 nH. The period of oscillation of the current is $\sim$ 600 nsec, twice that of the laser output peaks.

The time dependence of the voltage across the discharge shows a negligible variation with pressure. There is typically a large voltage peak followed by a low voltage oscillation with a $\sim$ 300 nsec period. Additionally there is a superimposed irregular modulation similar to that observed for the current which is due to ringing associated with the secondaries. Removal of the latter, eliminates this high frequency oscillation as can be seen in Figure 10.

Figure 10 shows a correlation of the temporal dependence of the current, discharge voltage, and laser output at 1 atm. The initial spike on the voltage, which rose to $\sim$ 23 kV was truncated in order to show the structure at longer times. The peaks in the current and voltage correlate nicely, and the current and voltage appear to rise simultaneously. The onset
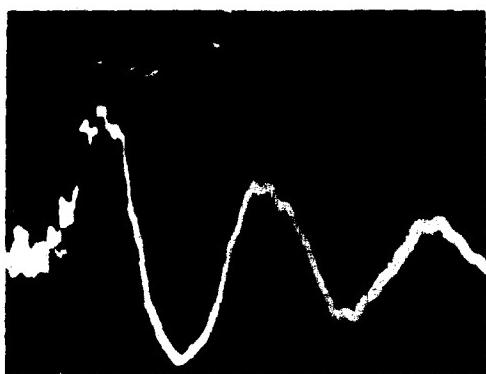
CURRENT

5 KA/div.
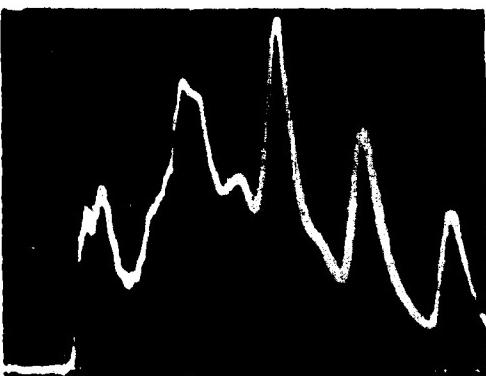
LASER   OUTPUT

1.73 μm
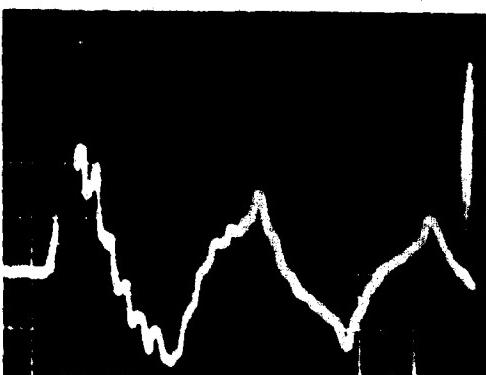
VOLTAGE

500 V/div.

→| |← .2 μsec

Figure 10.   Time correlation of discharge current, 1.73 μm laser
output and sustainer voltage for e-beam initiated
discharge in a 150:1 mixture of ArXe at 1 atm with
no secondary capacitors across discharge. The
voltage rises to ∿ 20 kV in the first 50-75 nsec.

of lasing appears to lag the sustainer onset by $\sim$ 100 nsec. The peaks in the laser output do not correlate clearly with either the extrema or zero crossings of the current and voltage. The delay between the voltage extrema and large laser peaks is $\sim$ 40 nsec.

An estimate of the electron density can be made from the correlated current and voltage diagrams if the electron drift velocity is known. In Section III we discuss the method by which we calculate the transport coefficients in the discharge. For an E/N of 8.5×10^{-18} volt-cm^2, corresponding to the second positive voltage peak in Figure 10, Figure 21 indicates a drift velocity of 4.5×10^{15} cm$\cdot$sec^{-1} if the fractional metastable xenon population is taken to be 10^{-3} of the total xenon population. From this drift velocity and the measured current of 7 kAmp we estimate an electron density of 5×10^{14} cm^{-3}. However, since the laser has some inductance, the true voltage across the plasma may be considerably different than indicated by the voltage probe measurements hence the electron density inferred from V-I should only be viewed as an estimate. An alternate measurement is discussed in the next section.

2.4 Free Carrier Absorption

In order to determine whether the decrease in efficiency at pressures above 2000 torr is due to a decrease in the free electron density, we have measured the electron density as a

25

function of pressure for a 150:1 mixture of argon and xenon at a constant sustainer voltage of 27 kV. At 2000 torr these parameters result in the optimum efficiency.

The free electron density was measured by observing the free-free [invserse Bremstrahlung] absorption of the radiation from a CO_2 laser. Initial attempts at observing the absorption at 10.6 μm using a spectrometer as a filter were unsuccesful because the intensity in the sixth order of the 1.7 μm line was sufficient to interfer with the 10 μm signal. The laser was subsequently forced to oscillate on the 9.6 μm P(20) line by inserting an SF_6 gas cell in the laser cavity to reduce the gain at 10 μm. The 9.6 μm signal was isolated with a spectrometer and detected with a fast HgCdTe detector.

Figure 11 is an example of the absorption observed at 9.6 μm and the voltage across the discharge as a function of time. The electron densities were calculated from the absorption observed at the first peak. The measurements were made with the secondary capacitors across the discharge and as a result the voltage profiles were irregularly modulated.

The electron density η_e is related to the plasma frequency ω_p by[9]

$$\omega_p^2 = \frac{\eta_e e^2}{m_e \epsilon_o} \ .$$

The optical frequency ω_o of the 9.6 μm radiation is 1.97×10^{14}

ABSORPTION
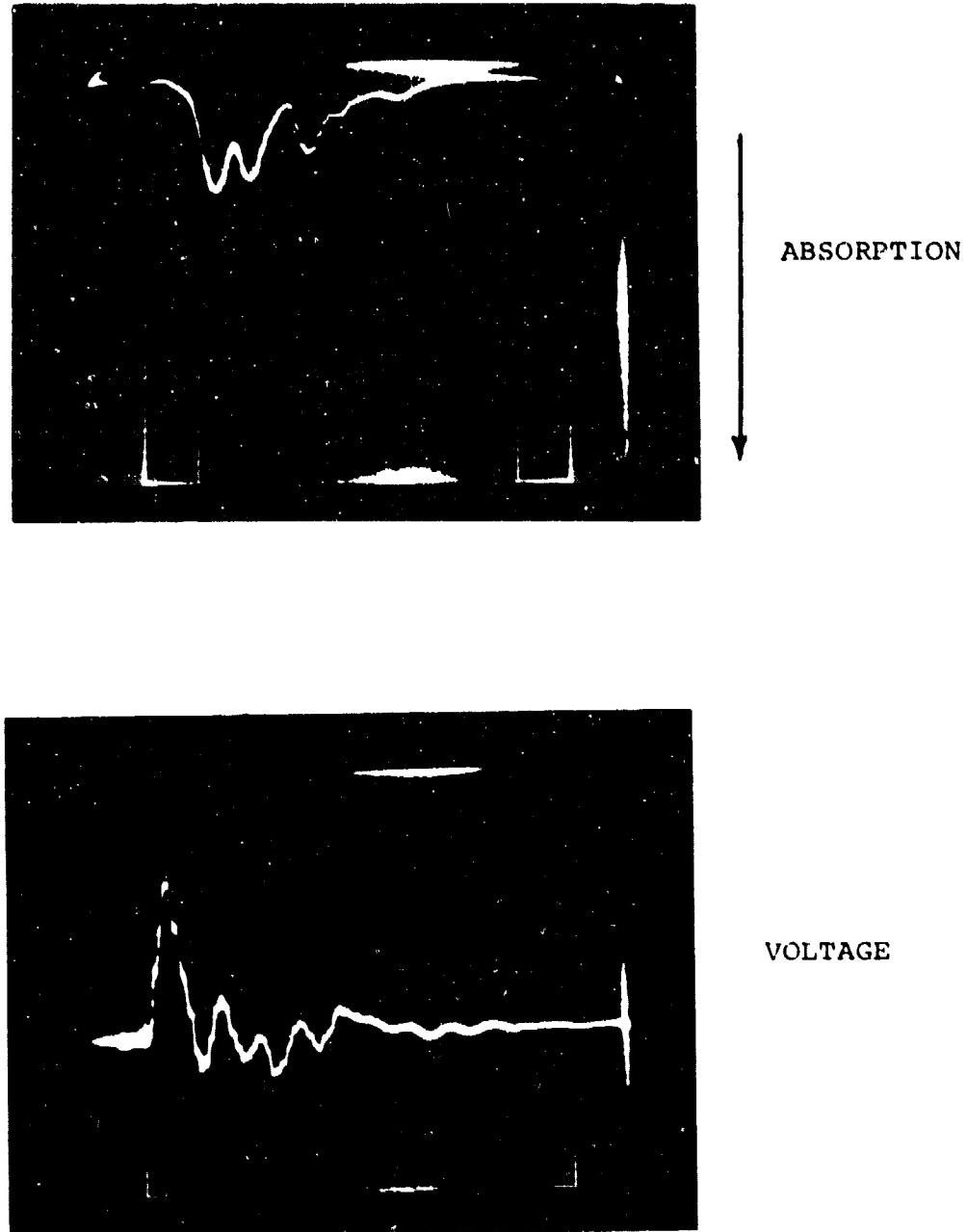
VOLTAGE

Figure 11.   9.6 μm absorption and discharge voltage profile at
3.5 atm and a 15 kV sustainer.   The time scale is
.2 μsec/division.

27

$\sec^{-1}$ and the plasma frequency ω_p proves to be on the order of 10^{11} $\sec^{-1}$ so that the approximation $\omega_p^2 << \omega_o^2$ is valid. In this case the free-free absorption α is given by

$$\alpha = \frac{\omega_p^2 \nu_e}{c(\omega_o^2 + \nu_e^2)}$$

where ν_e is the effective momentum transfer collision frequency. Thus the absorption is proportional to the product of the electron density and momentum transfer collision frequency:

$$\alpha = \eta_e \nu_e \frac{e^2}{m_e \epsilon_o c(\omega_o^2 + \nu_e^2)} \quad .$$

Figure 12 indicates the absorption per meter as a function of probe wavelength for various values of $\eta_e \nu_e$.

In the optical limit, $\nu_e^2 << \omega_o^2$, which pertains to this situation, the collision frequency is given by

$$\nu_e = -\frac{4\pi}{3} \int \nu(v) \frac{df_o(v)}{dv} v^3 dv$$

where f_o is the spherical part of the electron distribution function and $\nu(v)$ is the velocity dependent momentum transfer collision frequency. A Boltzmann code, to be described later, was used to derive the electron distribution function and to calculate ν_e.

28

FREE CARRIER ABSORPTION
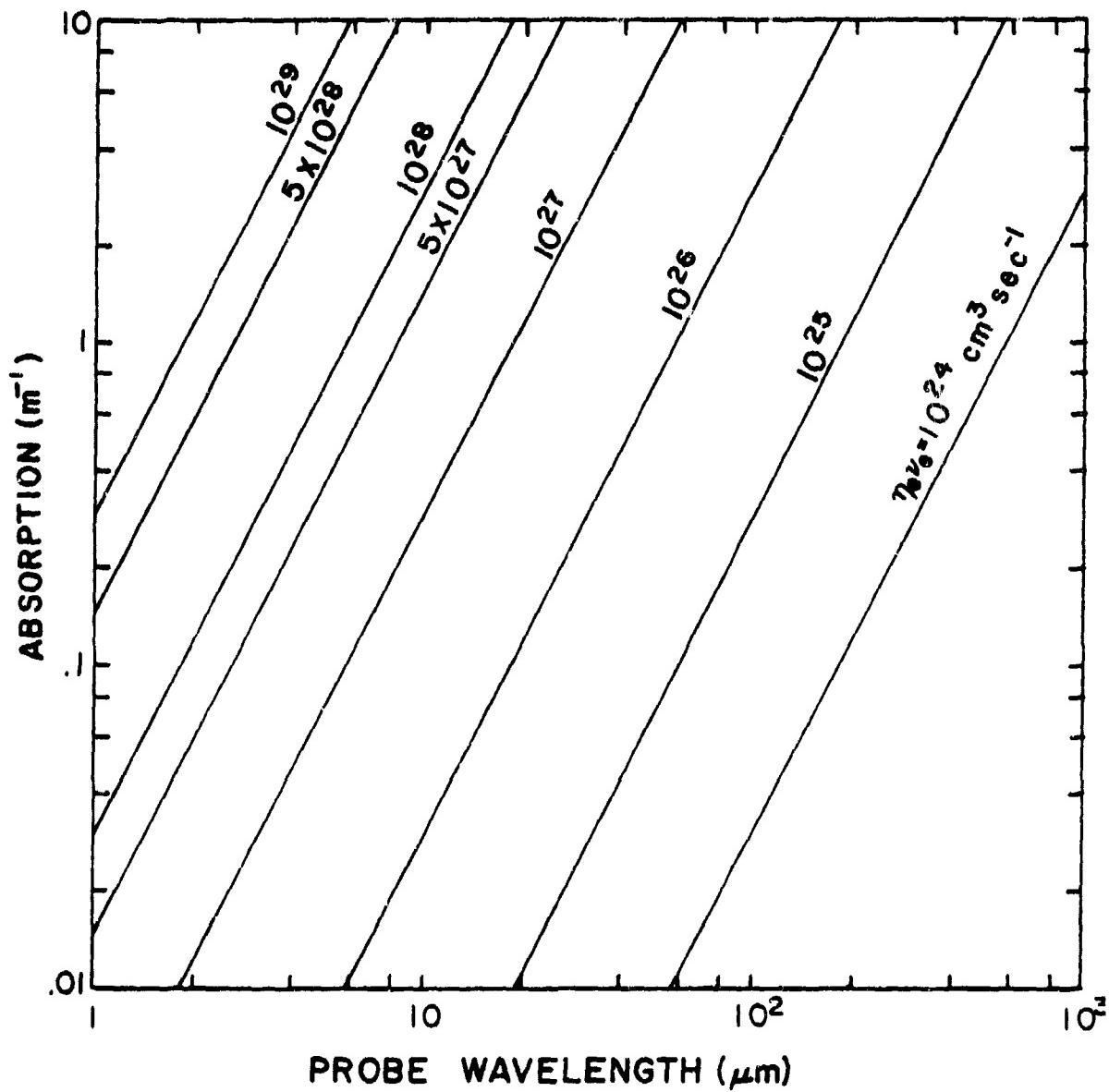
Figure 12. Free carrier absorption versus probe wavelength
for various products of free carrier density and
mean collision frequency.

Figure 13 illustrates the results of this calculation for various discharge conditions. The data points are the results of d.c. and optical limit calculation in a 150:1 ratio of argon to xenon for various discharge conditions. The d.c. and optical results agree within a factor of 1.5, the optical result being higher. The effective D/μ in our discharge is probably between 3 and 5 eV.

In Figure 14 we illustrate the fractional absorption of the 9.6 μm beam and the calculated free electron densities as a function of the total gas pressure. The free electron densities are anticipated to be accurate within a factor of 3 and differ from the V-I estimates by $\sim$ 5-10. The electron density peaks near 40 psi absolute, in the region where the laser efficiency is observed to peak. We will discuss this result in terms of e-beam energy deposition in a later section.

2.5 Fluorescence Measurements

In order to understand the kinetics of the Ar/Xe laser discharge it would be of interest to know which atomic and molecular states have large population densities at various times during the discharge. A survey of the time integrated emission from the discharge was made using a one meter spectrometer (8 $\overset{o}{A}$ mm^{-1} dispersion) with a film plate attachment. The twelve strongest lines observed are listed in Table 2.

30
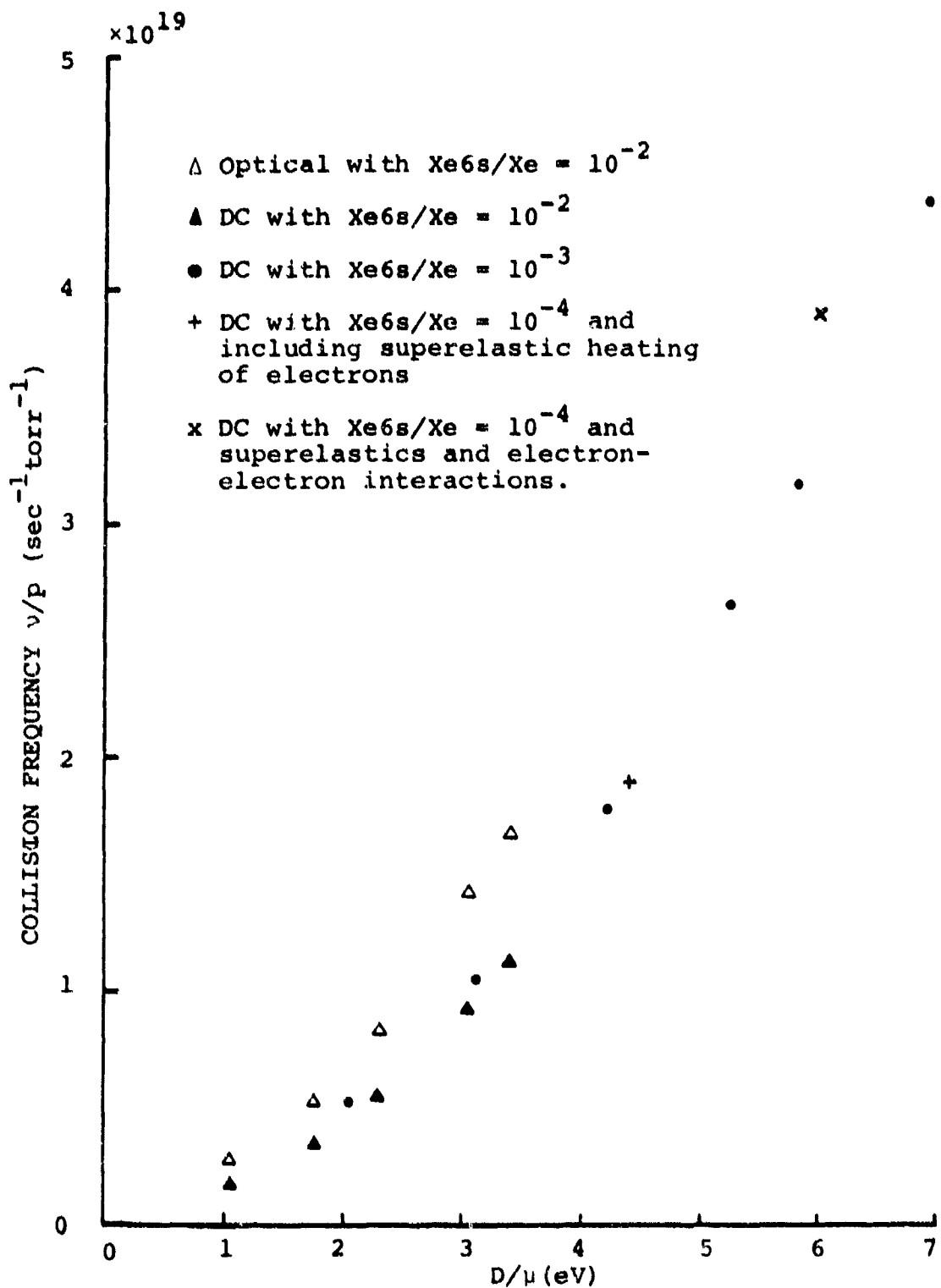
Figure 13. Optical and DC collision frequencies for 150:1
argon/xenon mixtures. The superelastic and
electron-electron calculation were performed
by Lowell Morgan at J.I.L.A.

31
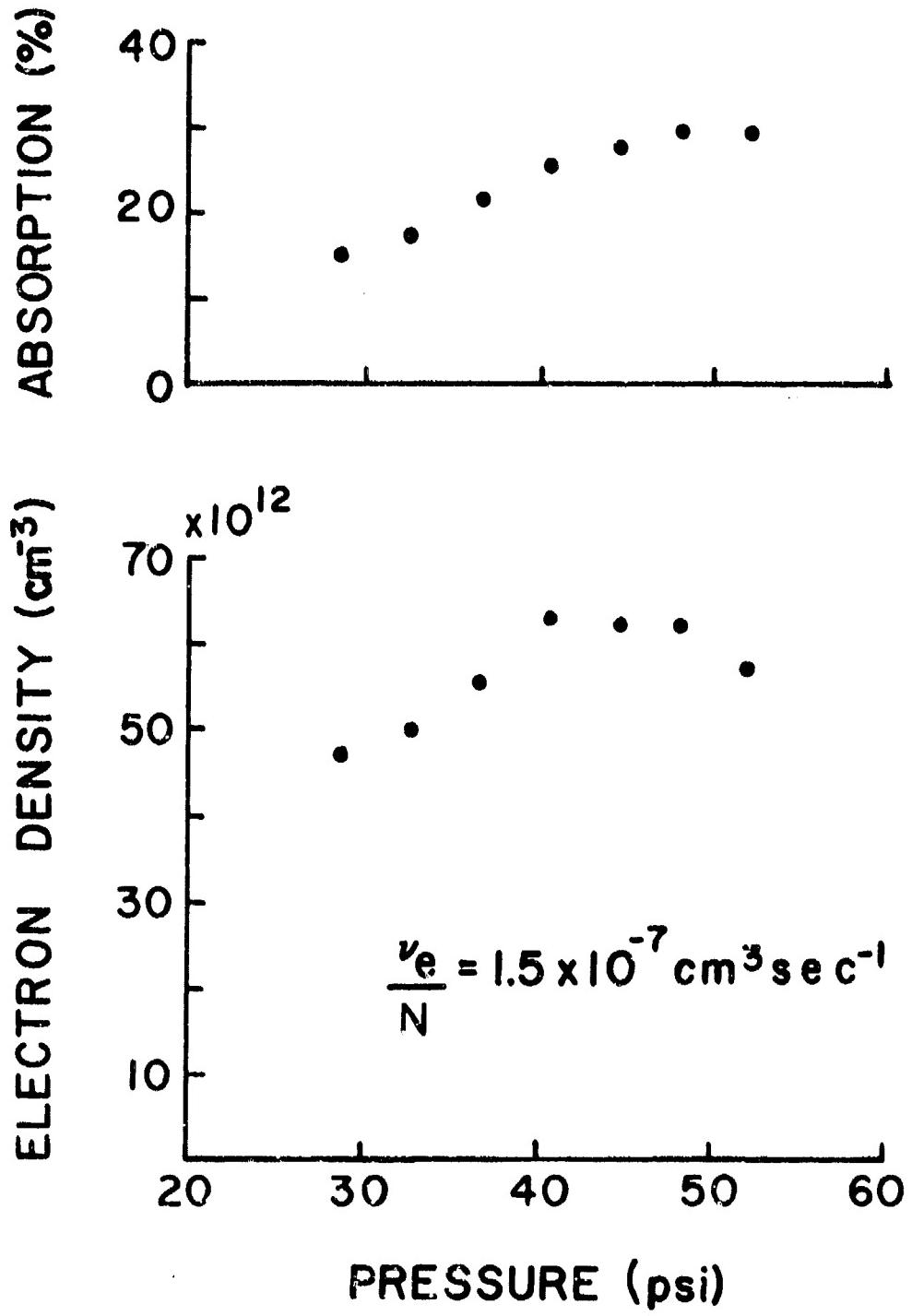
Figure 14. Observed free carrier absorption of 9.6 μm radiation by the 1 m long ArXe discharge and calculated electron densities as a function of total gas pressure.

TABLE 2

TWELVE MOST INTENSE LINES FROM Ar/Xe DISCHARGE
(350 to 600 nm)

λ (nm)	SPECIES	TRANSITION
358.8	Ar^+	$4d\,^4F_{9/2} - 4p\,^4D^{\circ}_{7/2}$
467.1	Xe	$7p(5/2)_3 - 6s(3/2)_2$
462.4	Xe	$7p(3/2)_2 - 6s(3/2)_2$
357.7	Ar^+	$4d\,^4F_{7/2} - 4p\,^4D^{\circ}_{5/2}$
473.4	Xe	$6p'(3/2)_2 - 6s(3/2)_1$
380.3	Ar^+	$4d'\,^2D_{5/2} - 4p'\,^2D^{\circ}_{5/2}$
469.7	Xe	$7p(5/2)_2 - 6s(3/2)_2$
420.1	Ar	$5p(5/2)_3 - 4s(3/2)_2$
450.1	Xe	$6p'(1/2)_1 - 6s(3/2)_2$
415.9	Ar	$5p(3/2)_2 - 4s(3/2)_2$
480.7	Xe	$7p(1/2)_0 - 6s(3/2)_1$
452.5	Xe	$6p'(3/2)_2 - 6s(3/2)_2$

They correspond to transitions terminating on the metastable states of Ar and Xe along with three lines from Ar^+. No molecular emission and no strong Xe^+ emission was observed. Curiously, two strong lines from the discharge at 394.4 and 396.1 nm correspond to the strongest transitions in atomic aluminum. It is not clear whether this emission came from the discharge volume in general or whether it was concentrated near the surface of the aluminum anode, however the emission presumably was due to e-beam impact on the anode.

The remainder of the lines have been assigned to various argon and xenon neutral or ion transitions. The intensities of these lines and those which are somewhat weaker indicate observable populations in levels up to at least the 8d states of xenon.

In order to determine the time evolution of the densities of the excited states, various fluorescence lines were observed with a photomultiplier tube. In general, the fluorescence exhibited peaks corresponding to peaks in the discharge current and some states showed mild fluorescence from e-beam pumping. Fluorescence curves characteristic of some states are shown in Figures 15 and 16.

We attribute the intense line at 358.8 nm to the relatively strong $4d\,^4F_{9/2} \rightarrow 4p\,^4D^o_{7/2}$ transition in Ar^+ since the alternative transition, $7p(3/2)_2 \rightarrow 4s'(1/2)_1$, in argon is weak.

34
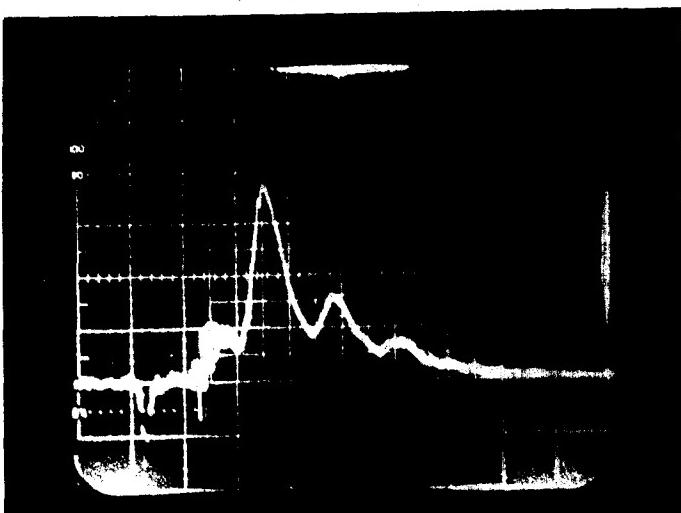
$$Ar^+$$
$$4d\,^4F_{9/2} \rightarrow 4p\,^4D^{\,o}_{7/2}$$
$$358.8 \text{ nm}$$
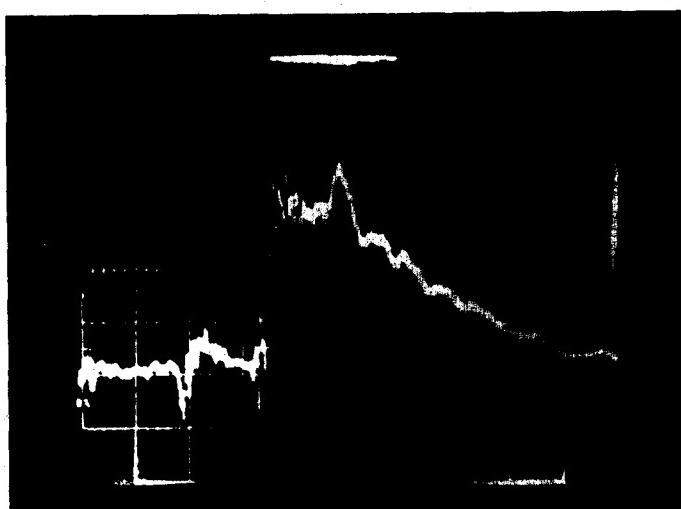
$$Xe$$
$$7d(7/2)_3 \rightarrow 6p(5/2)_2$$
$$688.2 \text{ nm}$$
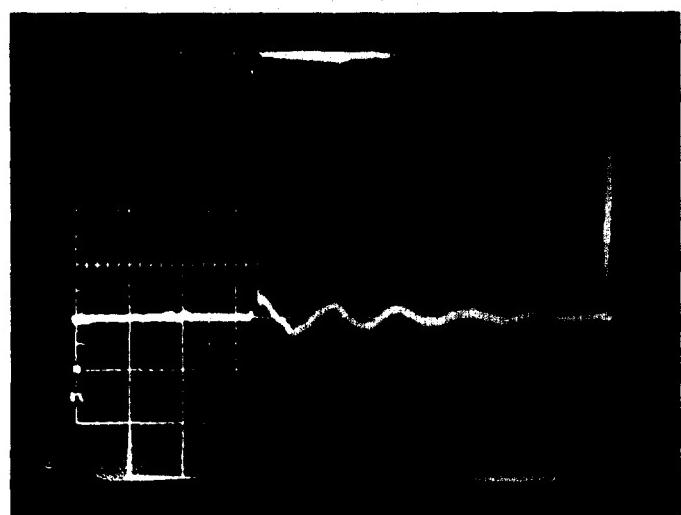
VOLTAGE PROFILE

150:1 Ar:Xe

Figure 15.   Voltage profile and fluorescence on various argon and xenon transitions.   150:1 ratio of Ar:Xe at 1 atmosphere and 500 nsec/division.

Xe
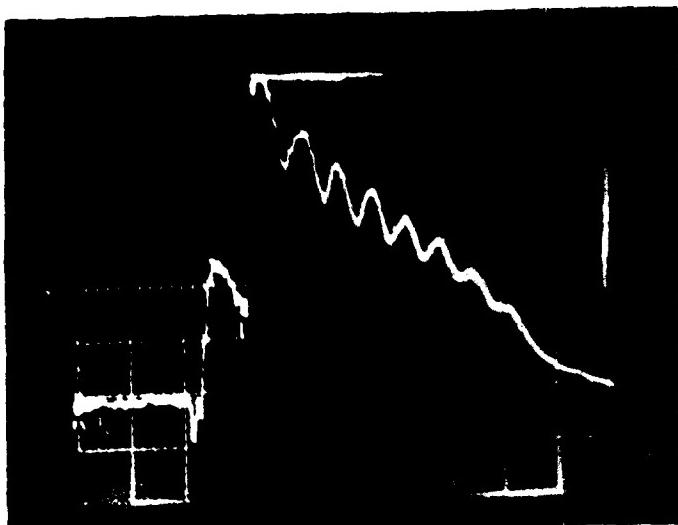
$6p(1/2)_1 \cdot 6s(3/2)_1^\circ$

1083.8 nm
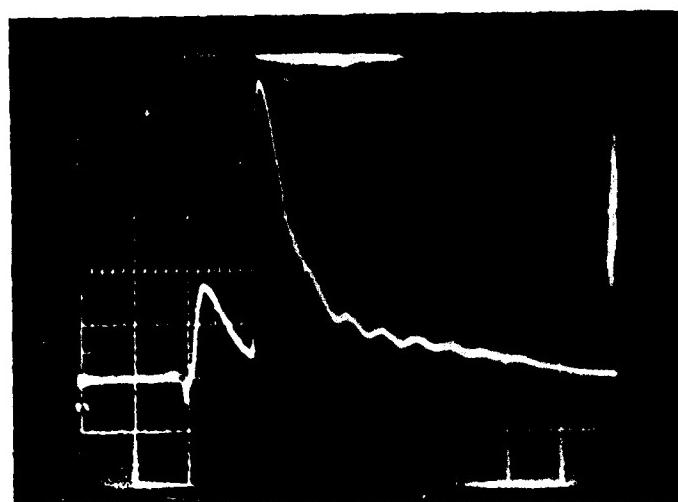
Xe

$6p(1/2)_1 \cdot 6s(3/2)_2$

980.0 nm
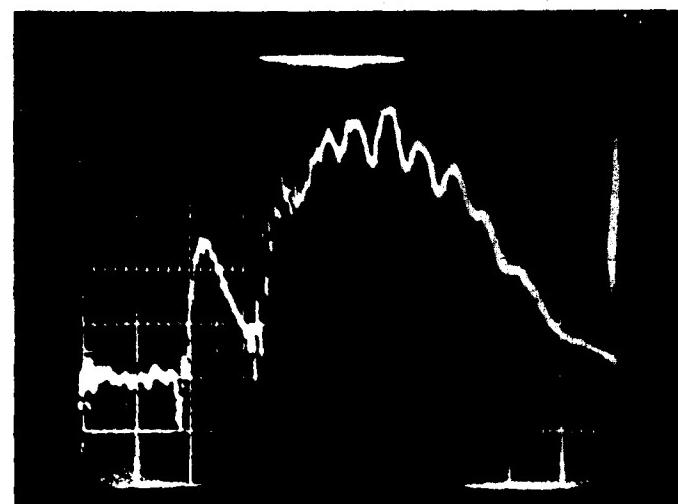
Xe

$6p(3/2)_2 \cdot 6s(3/2)_1$

895.2 nm

Figure 16. Fluorescence on typical 6p-6s transitions in xenon. 150:1 ratio of Ar:Xe at 1 atmosphere and 500 nsec division.

46

Two other lines at 357.7 nm and 380.3 nm are assigned to the $4d\,^4F_{7/2} \rightarrow 4p\,^4D_{5/2}^{\circ}$ and $4d'\,^2D_{5/2} \rightarrow 4p'\,^2D_{5/2}^{\circ}$ transitions in Ar^+. The upper levels for the 358.8 nm and 357.7 nm and the 380.3 nm transitions lie 23 and 25 eV respectively above the Ar^+ ground state. It is not anticipated that a sizeable population of these upper states could be created from the ground state ion at even the largest E/N observed during the discharge pulse. Highly excited ion states can only be created via e-beam excitation. Thus it is difficult to understand how the 357.7 nm radiation can be modulated by the discharge, unless the e-beam creates a metastable ion population in the ^4P and ^4D states at about 16.5 eV above the ground state. Additionally the rate constant for destruction of these states via charge exchange with xenon would have to be less than $\sim$ 10^{-12} cm^3sec^{-1} for the population to last 800 nsec.

The fluorescence on many of the levels between 7p and 8d is weak and it is difficult to discern any structure in the emission. The 688.2 nm radiation from the $7d(7/2)_3 \rightarrow 6p(5/2)_2$ transition, shown in Figure 15, indicates a small 7d population originating from the e-beam followed by a rapid rise in population at the initiation of the discharge. The population decays slowly away with a very slight modulation synchronized with the variations in the discharge voltage. The decay of the fluorescence is not exponential, but it falls to e^{-1} of

37

the peak value in ~ 1 µsec. The radiative lifetime of this state was calculated in the Coulomb approximation[10] to be 10^{-7} sec, indicating that the state is being continually populated during the discharge.

Emissions from some 6p-6s transitions, some of which are shown in Figure 16, exhibit strong modulation due to oscillations in the discharge current for about 100 nsec after the initiation of the discharge. This modulation is superimposed upon a broad emission which peaks after the discharge starts. Additionally there is fluorescence observed from direct e-beam pumping. The shape of the post e-beam fluorescence of the $6p(3/2)_2 \rightarrow 6s(3/2)_1$ transition suggests a gradual build up of the population after the discharge is initiated, as would be anticipated if the 6p levels were populated by cascade from some higher excited states. Many other 6p levels show an immediate increase in fluorescence, as shown in Figure 16, which suggests rapid direct excitation.

For the 500 nsec between the firing of the e-beam and the triggering of the sustainer the fluorescence decays exponentially with a time constant of approximately 300 nsec as determined from the fluorescence of the 980.0 nm, $6p(1/2)_1 \rightarrow 6s(3/2)_2$, and 895.2 nm, $6p(3/2)_2 \rightarrow 6s(3/2)_1$, curves. The same time constant is observed for the tail of the 10838 nm, $6p(1/2)_1 \rightarrow 6s(3/2)_1$, transition. The radiative lifetime of

38

the 6p manifold is $\sim$ 30 nsec so that unless the 6p transitions are radiatively trapped the observed decay constant must reflect the rate at which energy flows into the 6p manifold from higher excited states. The net lifetime of the states above 5d is calculated to be $\sim$ 250 nsec, approximately that observed for the fluorescence. For an $ArXe^+$ or Xe_2^+ dissociative recombination rate of 1×10^{-6} cm^3sec^{-1} and an electron density of $\sim 10^{13}$ cm^{-3} the ion loss rate would be $\sim$ 100 nsec, so it is possible that the 6p manifold is populated by either dissociative recombination or radiative cascade following recombination.

In general the fluorescence curves suggest that the variations in E/N during the discharge modulate the population densities of the states at least up through 8d in xenon. It appears however that the dominant contribution to the populations arises from a slow decay of some highly excited state, possibly Xe_2^+ or $ArXe^+$, which either feeds the 6p levels directly or which populates the higher states such as $7d(7/2)_3$ which subsequently decays into the lower levels.

In order to determine the time dependence of the densities of those levels which do not emit radiation at wavelengths which our photomultipliers can detect, or for which the radiation is trapped, we have attempted to observe absorption of the radiation from a high pressure xenon discharge lamp. These

39

attempts have been unsuccessful due to competing emission at or near the wavelengths at which we were attempting to observe the absorption.

SECTION III

MODELING OF THE ARGON/XENON DISCHARGE

3.1 Argon/Xenon System

The difficulty in understanding the kinetics of the argon/xenon system arises not only from the paucity of knowledge about the individual atoms and homonuclear molecules, but also from the number of heternuclear molecules which are possible and about which no information is available. In order to fully understand the mechanisms which give rise to a dominant laser transition at 1.73 μm it will not be sufficient to be aware of the gross energy transfer mechanisms. It will also be necessary to understand the details of energy transfer among the states of the xenon 5d and 6p manifolds. Since intramanifold energy transfer data is only now becoming available, and since the rate constants for some possibly important mechanisms are unknown, any attempt at modeling the laser discharge realistically can be made only with the intention of identifying a few key mechanisms by which energy is channeled through the laser levels.

The energy level diagram of the lower excited states of the Ar/Xe system is shown in Figure 17. Among the states which could be important to the modeling but have not been included in the figure are the higher excited argon states, heteronuclear ions such as $XeAr^+$ and $ArXe_2^+$, the homonuclear

41

Figure 17.   Some energy levels of the argon-xenon system.

42

triatomics (Xe_3^+), and the shallowly bound $ArXe^*$. For most of these molecules the kinetics are poorly understood.

The processes treated in the discharge model must necessarily be limited to those for which data is available or may be estimated. Some such processes which could lead to a population in the upper laser level are:

1) Direct electron impact excitation either from the xenon ground state or Xe6s into the 5d level, or into Xe^{**} followed by quenching or radiative cascade to the 5d level.

2) Energy transfer from Ar_2^*.

3) Energy transfer from Ar4s into Xe^{**}.

4) Dissociative recombination from Xe_2^+ or $ArXe^+$.

The important energy transfer processes considered in this model are illustrated in Figure 18. In order to reduce the number of coupled differential equations for the population densities the argon and xenon atoms were considered to consist of one metastable level, one ion level and a bulk level which in argon extended from 4p to Ar^+ and in Xe from 7s to Xe^+. Additionally in Xe there were the upper and lower laser levels. For each of the homonuclear molecules there is one ion state (Xe_2^+, Ar_2^+) and one excited neutral diatomic (Xe_2^*, Ar_2^*). The triatomic ion states Xe_3^+ and Ar_3^+ were included in initial calculations and Xe_3^+ was later dropped as it never attained a significant population density.

43

Figure 18. Schematic diagram of energy flow considered for Ar/Xe modeling.

triatomics (Xe_3^+), and the shallowly bound ArXe[*]. For most of these molecules the kinetics are poorly understood.

The processes treated in the discharge model must necessarily be limited to those for which data is available or may be estimated. Some such processes which could lead to a population in the upper laser level are:

1) Direct electron impact excitation either from the xenon ground state or Xe6s into the 5d level, or into Xe^{**} followed by quenching or radiative cascade to the 5d level.

2) Energy transfer from Ar_2^*.

3) Energy transfer from Ar4s into Xe^{**}.

4) Dissociative recombination from Xe_2^+ or $ArXe^+$.

The important energy transfer processes considered in this model are illustrated in Figure 18. In order to reduce the number of coupled differential equations for the population densities the argon and xenon atoms were considered to consist of one metastable level, one ion level and a bulk level which in argon extended from 4p to Ar^+ and in Xe from 7s to Xe^+. Additionally in Xe there were the upper and lower laser levels. For each of the homonuclear molecules there is one ion state (Xe_2^+, Ar_2^+) and one excited neutral diatomic (Xe_2^*, Ar_2^*). The triatomic ion states Xe_3^+ and Ar_3^+ were included in initial calculations and Xe_3^+ was later dropped as it never attained a significant population density.

43

Once the key energy transfer processes were identified, it was necessary to determine the electron excitation rates for the excited states, the rate constants for the energy transfer processes, the radiative lifetimes and branching ratios in order to treat radiative cascade, and the e-beam energy deposition kinetics in order to determine the initial conditions for the discharge. Each of these topics will now be discussed in detail.

3.1.1 Boltzmann Code and Cross Sections

The Boltzmann code used to determine the electron energy distribution function and to calculate the excitation rates and transport parameters was written by Phelps and co-workers and is described in the literature.[11,12] Since this code does not correct the calculated distribution function for electron-electron or super-elastic collisions, the effective electron temperature predicted by the code may be too small. The reduced electron temperature will mostly affect the excitation rates predicted for the higher energy loss processes.

The proper method for solving the time dependent coupled differential equations for the population densities is to put the initial population densities and E/N into the Boltzmann code and use the resulting excitation rates to calculate the new population densities at time t + Δt. These densities would then be put into the code to determine new rates which

would be used to calculate the densities at the new time increment. However, since it takes about 12,000 time increments to model 1200 nsec of the discharge it is too costly and time consuming to calculate the excitation rates vs. E/N for a fixed population distribution for the duration of the discharge. The distribution chosen was for the Xe6s population to be .1% of the total xenon population. Since this approximation somewhat underestimates the total excited population, the rates calculated will be for a somewhat elevated electron temperature and may compensate for the neglected superelastic and electron-electron collisions. As a check on the effect of the fractional xenon population used in the Boltzmann code on the final results of the discharge model, the model was recalculated using excitation rates derived by assuming a fractional Xe6s density of 1% of the xenon population. Although the resulting densities were of course changed, they generally agreed within an order of magnitude with those from the previous calculation, and the general conclusions regarding the importance of the various energy transfer processes were unchanged.

The cross sections used in the Boltzmann code for argon and xenon momentum transfer[13] argon and xenon ionization[14], argon metastable ionization[15] and xenon metastable ionization[16] are to be found in the literature. The total argon and

46

xenon excitation cross sections of Schaper and Scheibner[17]
were used to calculate the Ar4s and Xe6s excitation rates.
These cross sections of course will produce excitation rates
which are larger than the true rate since they include con-
tributions from the cross sections for excitation of the
higher excited states. This choice of cross sections should
not lead to serious difficulties in the modeling since the
discharge E/N is large enough to produce significant excitation
of the metastable states only for the first $\sim$ 100 nsec, and be-
cause during the lower E/N regimes of the discharge the energy
is rapidly redistributed among the excited states which assume
density distributions which are relatively independent of the
population densities at times less than $\sim$ 75 nsec.

Cross sections both direct and exchange, for excitation
among the excited states were calculated using the Gryzinski
classical formulation.[18,19] The ionization cross sections can be
expressed as a function of the ionization potential for the
level, and the excitation cross sections in terms of the ioni-
zation potential of the initial state and the maximum energy
which can be transferred in the excitation. The manifold
averaged Gryzinski cross sections used in the model are given
in Table 3. Figures 19 and 20 show the excitation rates cal-
culated for a fractional Xe6s population of .1% of the xenon
density and a 150:1 ratio of argon to xenon.

TABLE 3

GRYZINSKI CROSS SECTIONS FOR THE MODEL

Xe 6p - 5d

ENERGY (eV)	CROSS SECTION (10^{-16} cm^2)	ENERGY (eV)	CROSS SECTION (10^{-16} cm^2)
.33	0.00	22.00	678.60
1.00	844.27	27.00	588.91
2.00	1410.24	32.00	521.37
3.00	1512.23	37.00	468.63
4.00	1487.70	42.00	426.23
5.00	1424.57	47.00	391.36
6.00	1351.51	52.00	362.14
7.00	1278.86	57.00	337.29
8.00	1210.37	62.00	315.87
9.00	1147.20	67.00	297.20
10.00	1089.46	72.00	280.77
12.00	988.90	77.00	266.20
14.00	905.14	82.00	253.18
16.00	834.71	87.00	241.47
18.00	774.82	92.00	230.88
20.00	723.32	97.00	221.24
		100.00	215.87

Xe 5d - BULK

ENERGY (eV)	CROSS SECTION (10^{-16} cm^2)	ENERGY (eV)	CROSS SECTION (10^{-16} cm^2)
.50	0.00	22.00	235.14
1.00	258.40	27.00	202.36
2.00	553.02	32.00	178.04
3.00	593.22	37.00	159.25
4.00	574.31	42.00	144.28
5.00	541.36	47.00	132.04
6.00	506.70	52.00	121.85
7.00	474.05	57.00	113.21
8.00	444.38	62.00	105.80
9.00	417.76	67.00	99.36
10.00	393.96	72.00	93.71
12.00	353.53	77.00	88.71
14.00	320.71	82.00	84.26
16.00	293.64	87.00	80.26
18.00	270.96	92.00	76.65
20.00	251.70	97.00	73.37
		100.00	71.54

Table 3. (continued)

Xe 6s - 6p

ENERGY (eV)	CROSS SECTION $(10^{-16}$ cm$^2)$	ENERGY (eV)	CROSS SECTION $(10^{-16}$ cm$^2)$
1.26	0.00	9.00	41.10
2.00	19.00	10.00	39.90
3.00	33.10	13.00	36.50
4.00	39.10	15.00	34.20
5.00	42.10	21.00	28.80
6.00	42.90	33.00	21.80
7.00	42.70	53.00	15.60
8.00	42.00	100.00	9.60

Xe 7p ION

ENERGY (eV)	CROSS SECTION $(10^{-16}$ cm$^2)$	ENERGY (eV)	CROSS SECTION $(10^{-16}$ cm$^2)$
1.23	0.00	23.00	56.93
2.00	161.94	28.00	49.75
3.00	171.43	33.00	44.21
4.00	158.16	38.00	39.82
5.00	143.11	43.00	36.25
6.00	129.63	48.00	33.29
7.00	118.11	53.00	30.80
8.00	108.35	58.00	28.67
9.00	100.03	63.00	26.83
10.00	92.88	68.00	25.22
11.00	86.70	73.00	23.80
13.00	78.56	78.00	22.54
15.00	73.70	83.00	21.42
17.00	68.79	88.00	20.40
19.00	64.37	93.00	19.48
21.00	60.43	98.00	18.65
		100.00	18.33

Table 3. (continued)

Xe 6p - BULK

ENERGY (eV)	CROSS SECTION (10^{-16} cm^2)	ENERGY (eV)	CROSS SECTION (10^{-16} cm^2)
1.58	0.00	23.00	21.70
2.00	8.44	28.00	19.00
3.00	29.70	33.00	17.00
4.00	36.30	38.00	15.30
5.00	38.20	43.00	14.00
6.00	38.30	48.00	12.90
7.00	37.60	53.00	11.90
8.00	36.50	58.00	11.10
9.00	35.20	63.00	10.40
10.00	33.90	68.00	9.81
11.00	32.60	73.00	9.27
13.00	30.20	78.00	8.79
15.00	28.10	83.00	8.37
17.00	26.20	88.00	7.98
19.00	24.50	93.00	7.63
21.00	23.00	98.00	7.31
		100.00	7.19

Xe 6s - 5d

ENERGY (eV)	CROSS SECTION (10^{-16} cm^2)	ENERGY (eV)	CROSS SECTION (10^{-16} cm^2)
1.57	0.00	9.00	36.80
2.00	7.27	10.00	36.00
3.00	24.00	14.00	32.30
4.00	31.90	16.00	30.50
5.00	35.60	20.00	27.30
6.00	37.20	32.00	20.70
7.00	37.60	52.00	14.80
8.00	37.40	100.00	9.00

Table 3. (continued)

Xe 5d - ION

ENERGY (eV)	CROSS SECTION (10^{-16} cm^2)	ENERGY (eV)	CROSS SECTION (10^{-16} cm^2)
2.22	0.00	24.00	31.41
3.00	41.68	29.00	28.30
4.00	51.93	34.00	25.69
5.00	53.09	39.00	23.51
6.00	51.53	44.00	21.66
7.00	49.12	49.00	20.08
8.00	46.52	54.00	18.73
9.00	43.99	59.00	17.54
10.00	41.61	64.00	16.51
11.00	39.43	69.00	15.59
12.00	37.43	74.00	14.77
14.00	37.85	79.00	14.04
16.00	37.02	84.00	13.38
18.00	35.68	89.00	12.78
20.00	34.23	94.00	12.23
22.00	32.79	99.00	11.74
		100.00	11.64

Xe 6p - ION

ENERGY (eV)	CROSS SECTION (10^{-16} cm^2)	ENERGY (eV)	CROSS SECTION (10^{-16} cm^2)
2.25	0.00	24.00	31.03
3.00	39.75	29.00	27.98
4.00	50.34	34.00	25.41
5.00	51.72	39.00	23.26
6.00	50.33	44.00	21.44
7.00	48.05	49.00	19.88
8.00	45.55	54.00	18.54
9.00	43.11	59.00	17.37
10.00	40.81	64.00	16.35
11.00	38.69	69.00	15.44
12.00	36.74	74.00	14.63
14.00	37.24	79.00	13.91
16.00	36.47	84.00	13.25
18.00	35.20	89.00	12.66
20.00	33.79	94.00	12.12
22.00	32.38	99.00	11.63
		100.00	11.53

Table 3. (continued)

Xe 6s - BULK

ENERGY (eV)	CROSS SECTION (10^{-16} cm^2)	ENERGY (eV)	CROSS SECTION (10^{-16} cm^2)
2.24	0.00	9.00	10.98
3.00	5.01	10.00	10.84
4.00	8.19	14.00	9.85
5.00	9.81	16.00	9.33
6.00	10.60	20.00	8.40
7.00	10.90	32.00	6.39
8.00	11.00	52.00	4.59
		100.00	2.79
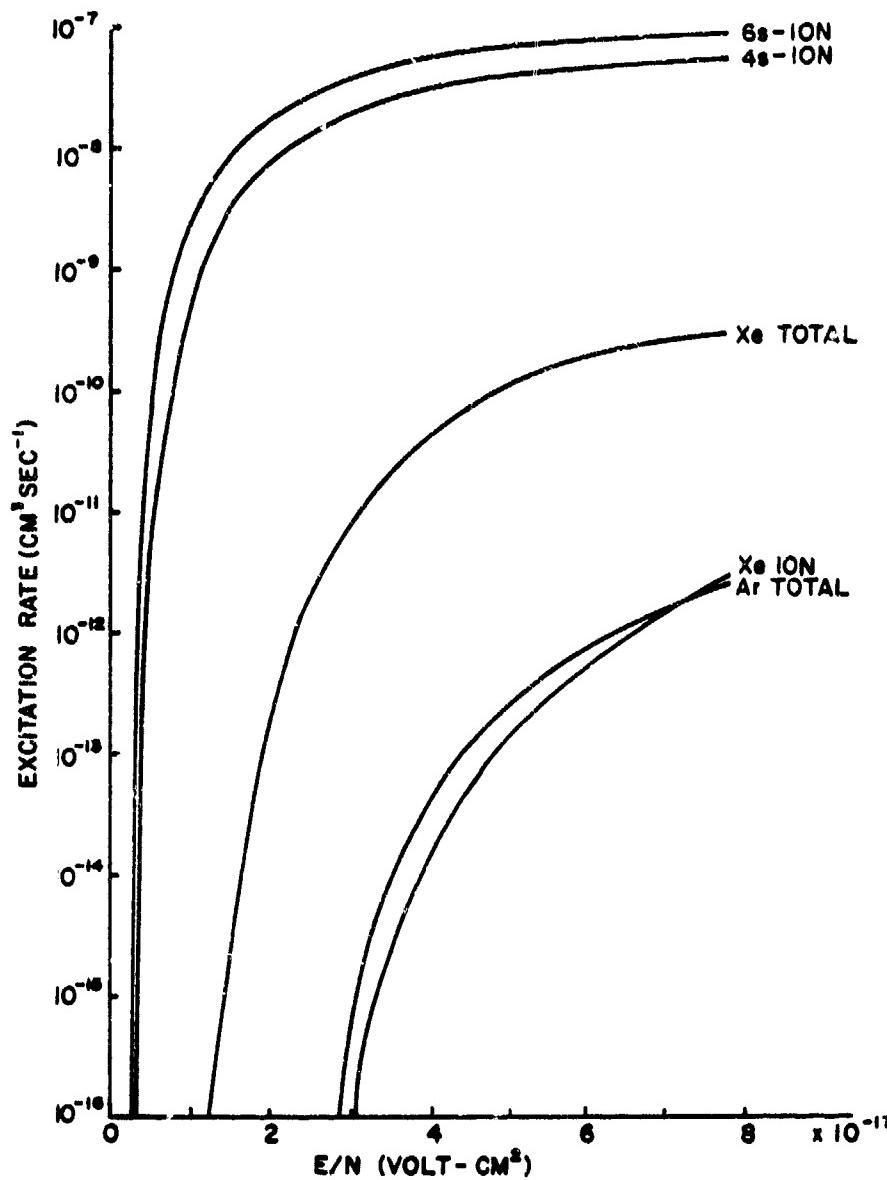
Figure 19. Rates for inelastic electron scattering on ground
and metastable states of argon and xenon. The rates
were calculated for a 150:1 ratio of argon to xenon
and a xenon metastable population of 10^{-3} times the
total xenon density.

53
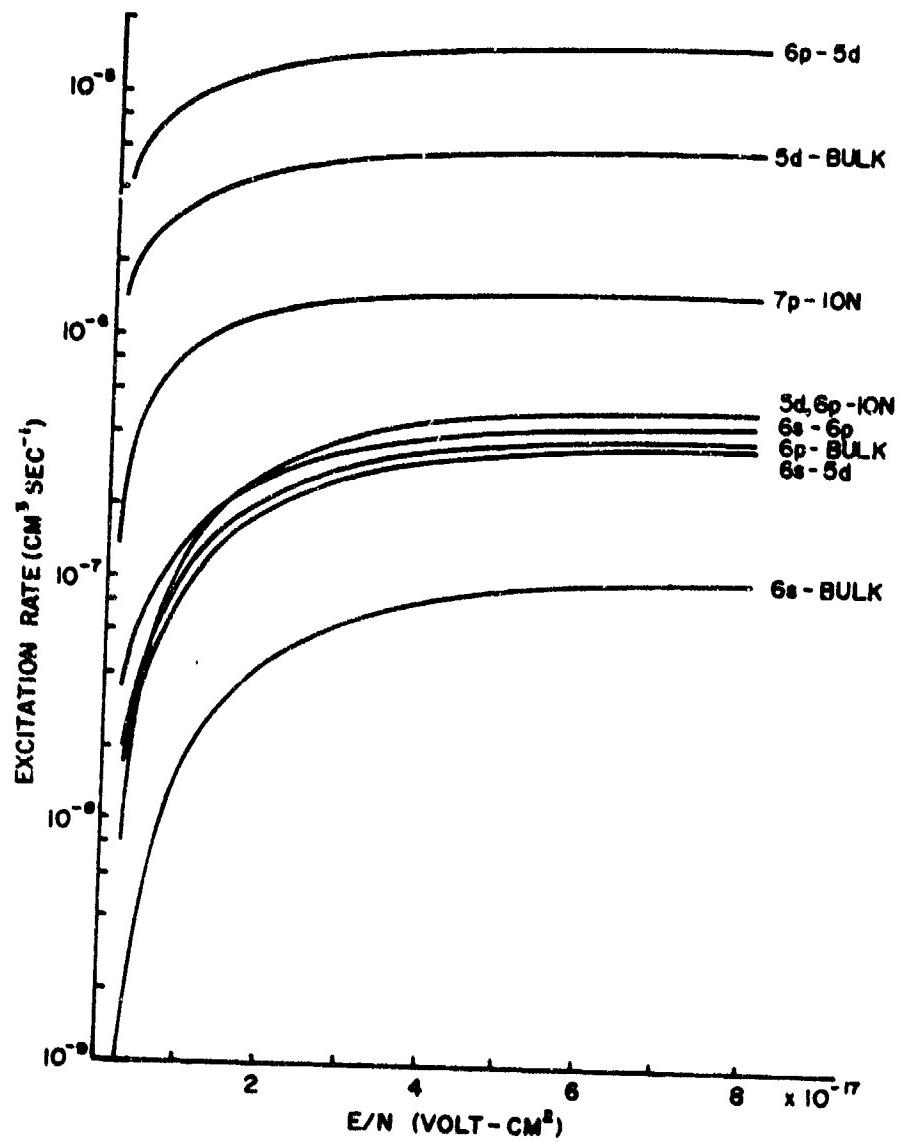
Figure 20. Excitation rates for higher excited states of argon and xenon calculated under the conditions of Fig. 1. The extremely large rates for 6p → 5d and 5d → bulk were reduced by an order of magnitude for much of the modeling.

54

Various transport coefficients were calculated for 3×10^{-18} $\leq$ E/N $\leq$ 8×10^{-17} volt-cm^2 for Xe6s: xenon ratios to 10^{-2}. Figure 21 shows the variation of drift velocity w_e with E/N for various Xe 6s, denoted Xe^m, fractional populations. In these calculations only 6s-6p, 6s-5d, 6s-bulk, 6s-ion were included as significant excited state reactions. The drift velocity calculations were used in estimating the peak electron density from the V-I discharge curves as described earlier.

Figures 22 to 24 illustrate the dominant fractional power transfer curves as a function of E/N for Xe6s/Xe = 0, 10^{-3} and 10^{-2} respectively. Some basic processes may be inferred from these curves:

1) at 100 nsec after the beginning of the discharge the E/N has risen to $\sim 10^{-16}$ volt-cm^2. The excited state densities at this time are still small. Therefore most of the initial discharge energy will go into Ar4s excitation, some into Xe$^+$ and Xe6s production, and the remainder into heating the gas.

2) as the discharge voltage drops the xenon metastable density will increase due to energy transfer from Ar* to Xe. At 1 atm. the initial excited argon density will be depleted in $\sim$ 60 nsec. At an E/N $\lesssim 1.6 \times 10^{-17}$ volt-cm^2, approximately the value at the smaller voltage peaks, and a fractional metastable concentration of 10^{-3}, the discharge power is essentially divided equally between elastic scattering and 6s-6p excitation.

55
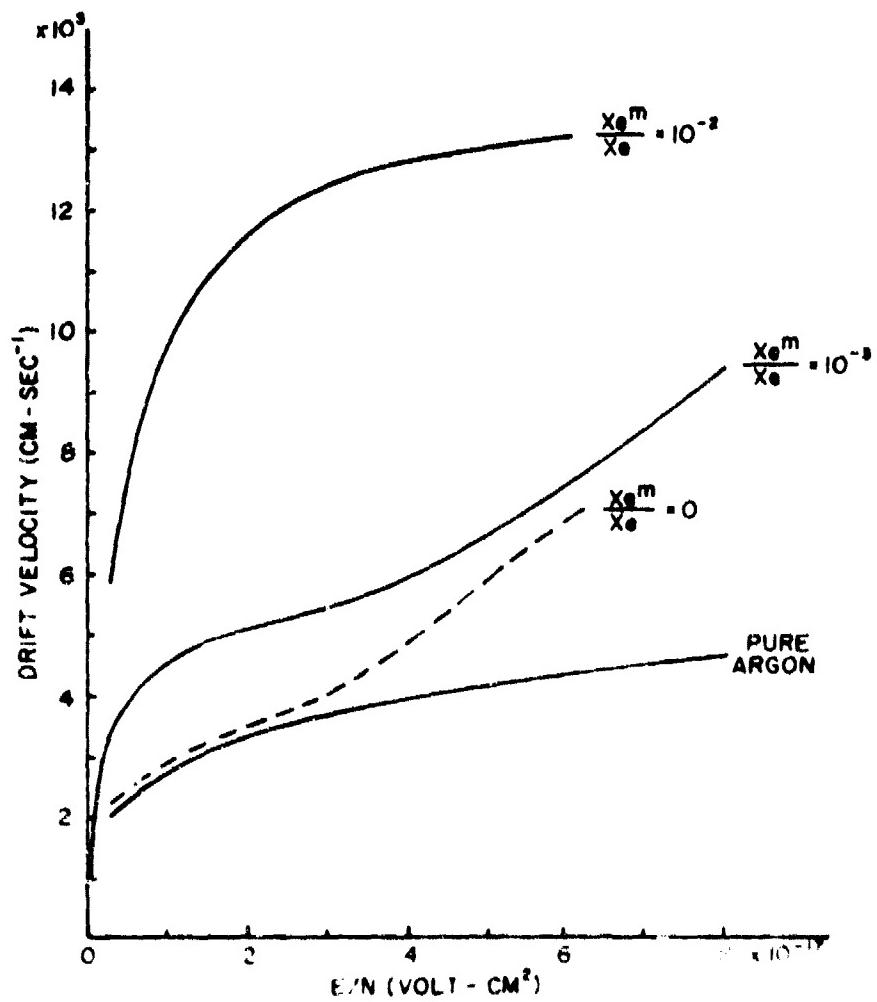
Figure 21. Drift velocity of electrons in argon/xenon mixtures. The pure argon value is from [71] $w_e = 3.7 \times 10^5 (E/P)^{.25}$. The remainder are calculated for a 150:1 argon/xenon ratio.

56
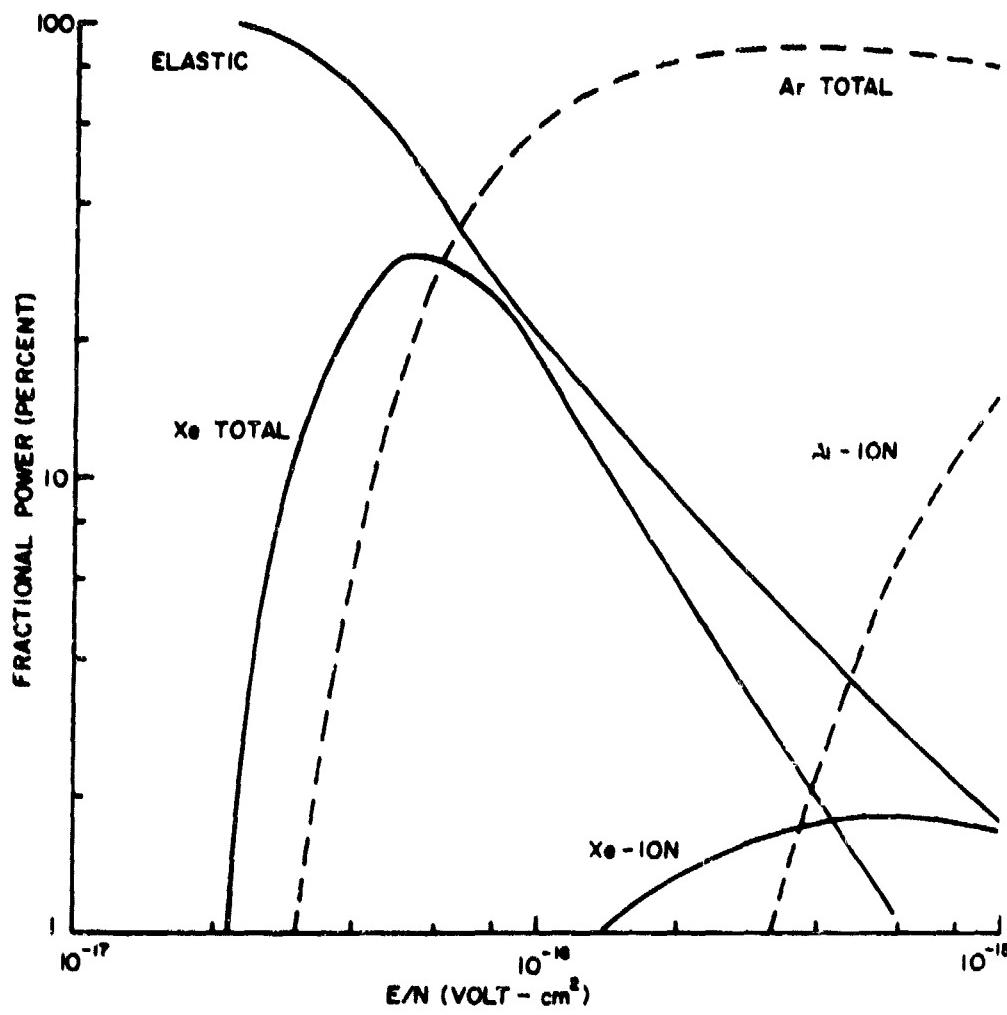
Figure 22. Fractional power lost to designated scattering processes in a 150:1 argon/xenon mixture for $Xe6s/Xe = 0$.

57
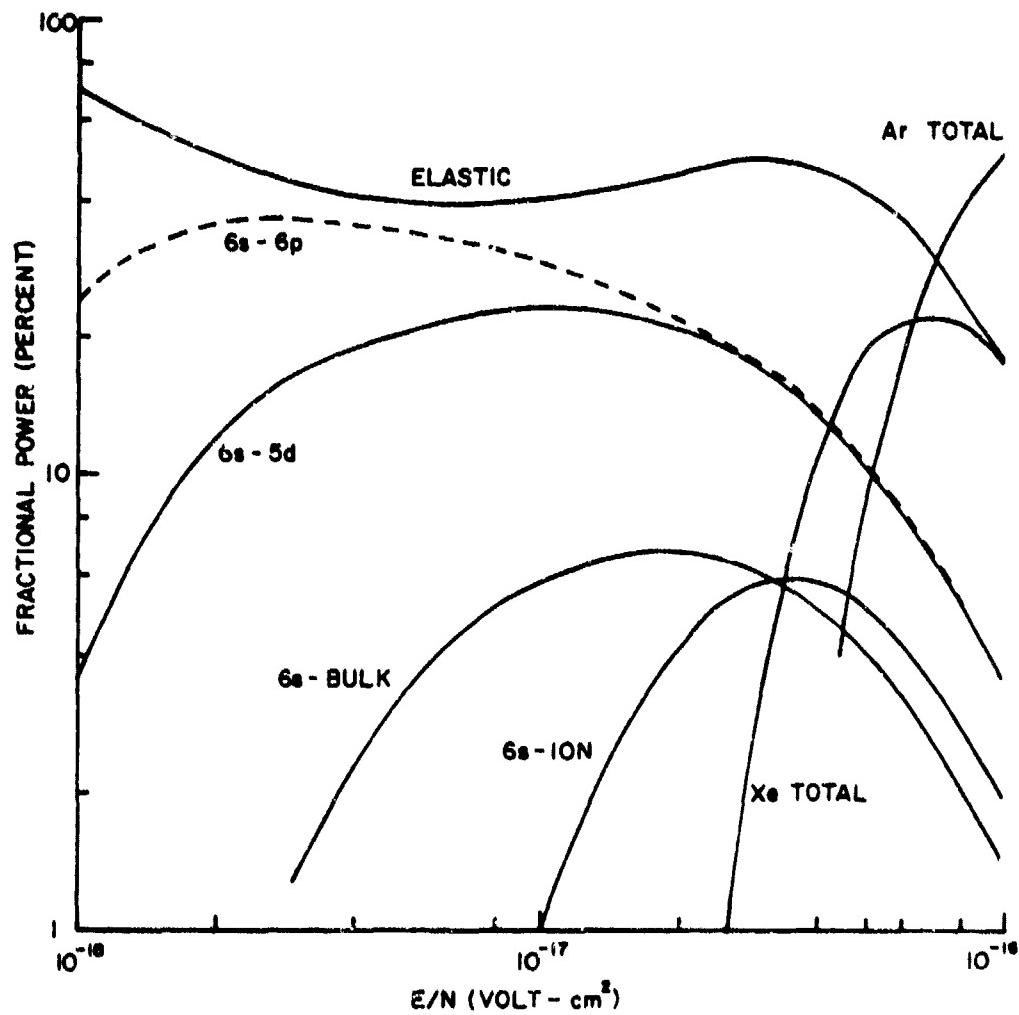
Figure 23. Fractional power lost to designated scattering
processes in a 150:1 argon/xenon mixture for
Xe6s/Xe = 10^{-3}.

58
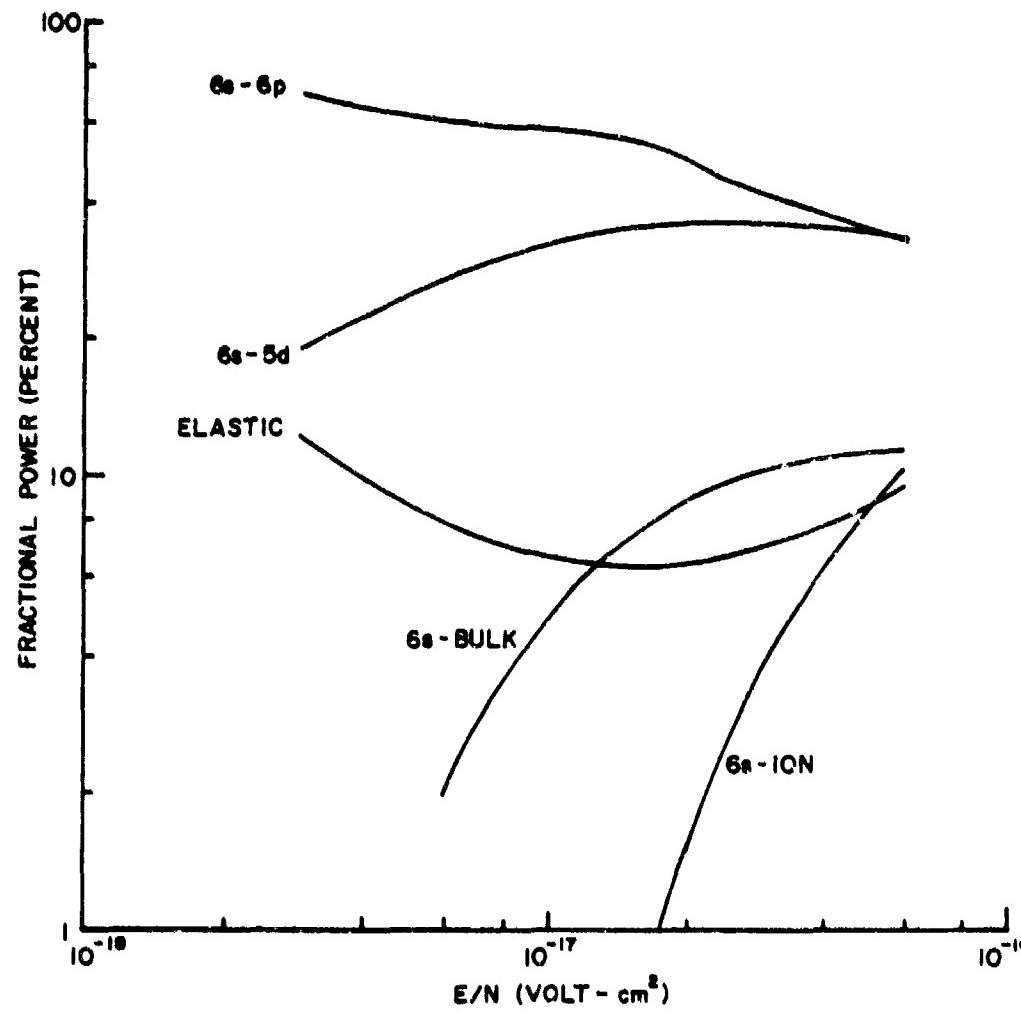
Figure 24. Fractional power lost to designated scattering
processes in a 150:1 argon/xenon mixture for
$Xe6s/Xe = 10^{-2}$.
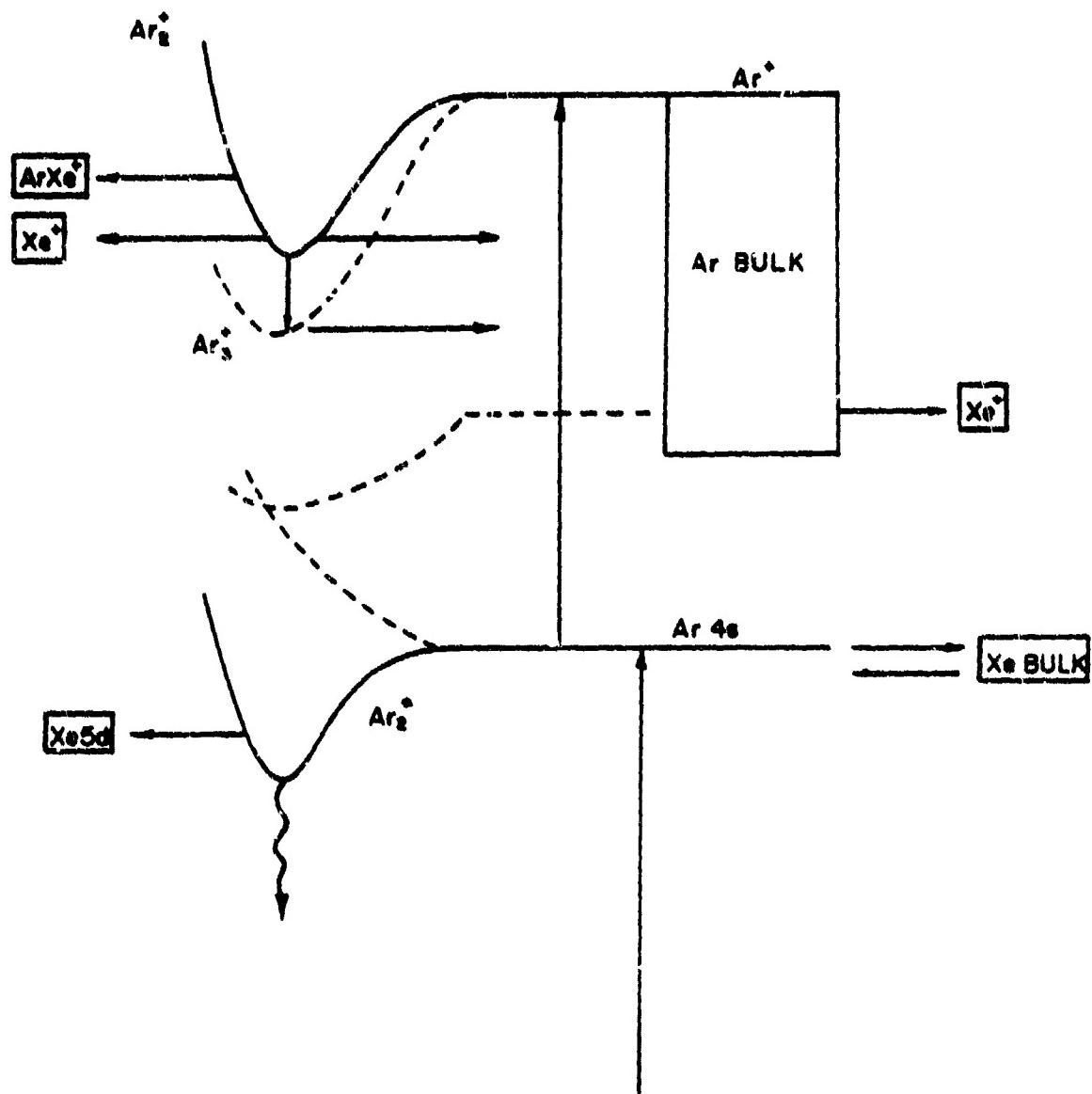
Figure 25.   Schematic diagram of the argon kinetics.

60
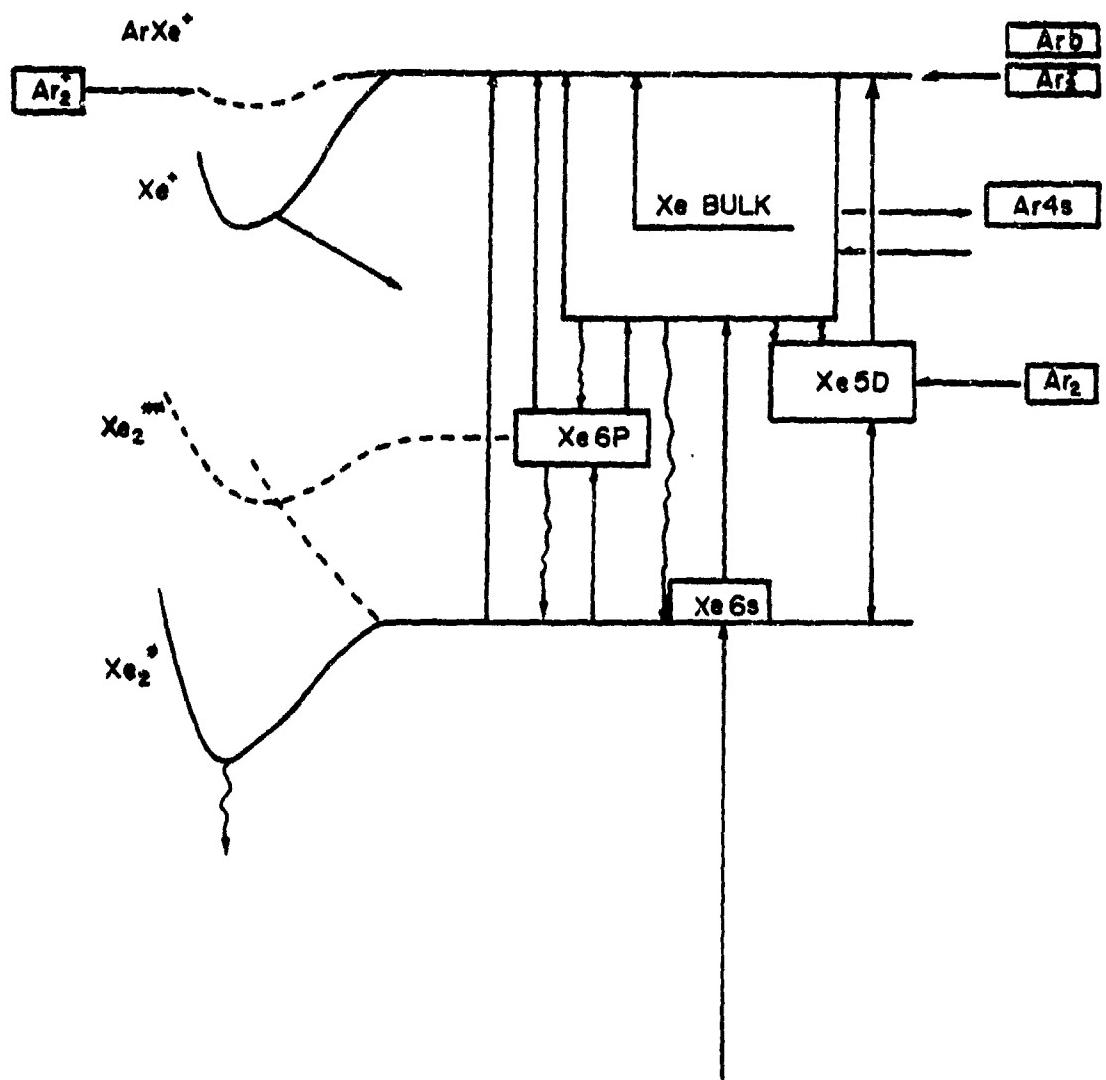
Figure 26. Schematic diagram of the xenon kinetics.

61

If the excitation processes among the higher excited states were included in the calculation, significant power losses into these processes should also be predicted. Thus it would be possible to have stepwise excitation from Xe6s up to Xe5d, or for stepwise ionization of Xe6s with dissociative recombination of Xe_2^+ into Xe5d. Either mechanism will allow for a recirculation of energy from Xe6s through the 5d laser manifold.

3.1.2 Energy Transfer and Quenching Rates

Many of the energy transfer, excitation, and radiative processes considered in the modeling are shown in Figures 25 and 26. In Table 4 we have indicated the various reactions which can occur in the discharge for which rates are available or can be readily estimated. Only those reactions indicated by an asterisk were actually used in the modeling.

The Boltzmann code calculations indicate that during the initial high E/N portion of the discharge most of the power loss is to Ar^* formation. The rate constant for two-body quenching of Ar^* to form Ar_2^* has been measured by LeCalve, et al.[20] They determine the rate constants to be 1.6×10^{-32} cm^6 sec^{-1}, for $Ar(^3P_2)$ and 1.7×10^{-32} cm^6 sec^{-1} for $Ar(^3P_1)$. These values are in general agreement with previous measurements quoted in their paper and by Leichner et al.[21]

King et al.[22] measured the rate constants for energy transfer from $Ar(^3P_0)$ and $Ar(^3P_2)$ into the xenon states between

TABLE 4

Ar-Xe REACTIONS AND RATE CONSTANTS

REACTION	RATE[†]	REFERENCE
(a) ION KINETICS		
$Ar^+ + Xe \rightarrow Xe^+ + Ar$	$\leq 1\,(-14)$	23
* $Ar^+ + 2Ar \rightarrow Ar_2^+ + Ar$	$2.5\,(-31)$	24
$Ar^+ + Xe + Ar \rightarrow Ar^+Xe + Ar$	$2\,(-31)$	25
* $Ar_2^+ + Xe \rightarrow Xe^+ + 2Ar$	$5\,(-10)$	26
* $Ar_2^+ + Xe \rightarrow ArXe^+ + Ar$	$2\,(-10)$	27
* $Ar_2^+ + 2Ar \rightarrow Ar_3^+ + Ar$	$4\,(-33)$	28,29
* $ArXe^+ + Xe \rightarrow Ar + Xe_2^+$	$7\,(-10)$	30
* $ArXe^+ + Ar \rightarrow Xe^+ + 2Ar$	$5\,(-11)$	31
* $Xe^+ + 2Ar \rightarrow ArXe^+ + Ar$	$2\,(-31)$	30
$Xe^+ + 2Xe \rightarrow Xe_2^+ + Xe$	$2.5\,(-31)$	7,25
$Xe_2^+ + 2Xe \rightarrow Xe_3^+ + Xe$	$7\,(-32)$	29,32
$Xe_2^+ + Xe + Ar \rightarrow Xe_3^+ + Ar$	$4.5\,(-32)$	33
(b) RECOMBINATION		
* $Ar_2^+ + e \rightarrow Ar^* + Ar$	$3T_e^{-.61}\,(-5)$	34,35
* $Ar_3^+ + e \rightarrow Ar^* + 2Ar$	$3.6\,(-5)$	29
* $ArXe^+ + e \rightarrow Ar + Xe^*$	$\geq 1\,(-6)$	36
* $Xe_2^+ + e \rightarrow Xe^* + Xe$	$2.2T_e^{-.72}\,(-4)$	37
$Xe_3^+ + e \rightarrow Xe^* + 2Xe$	$9\,(-5)$	29

63

Table 4. (continued)

REACTION	RATE	REFERENCE

(b) RECOMBINATION

$Xe^+ + e + Ar \rightarrow Xe^{**} + Ar$ $\left(\dfrac{300°K}{T_e}\right)^{5/2} (-26)$ 38

$Xe^+ + e \rightarrow Xe^{**} + h\nu$ $\left(\dfrac{300°K}{T_e}\right)^{.7} (-12)$ 39

(c) PENNING IONIZATION

$Ar^* + Ar^* \rightarrow Ar^+ + Ar + e$ $5(-10)$ 40,41

$Ar^{**} + Ar \rightarrow Ar_2^+ + e$ $2(-9)$ 42

* $Ar^{**} + Xe \rightarrow Xe^+ + Ar + e$ $2(-10)$ 43

$Ar_2^* + Ar \rightarrow Ar_2^+ + Ar + e$ $5(-10)$ 44

$Ar_2^* + Ar_2^* \rightarrow Ar_2^+ + 2Ar + e$ $5(-10)$ 41

$Xe^{**} + Xe^* \rightarrow Xe_2^+ + e$ $\dfrac{3\times10^{-17}}{\tau(Xe^*)}$ 45

$Xe_2^* + Xe_2^* \rightarrow Xe_2^+ + 2Xe + e$ $3.5(-10)$ 46

(d) NEUTRAL KINETICS

* $Ar^* + Xe \rightarrow Xe^* + Ar$ $2.2(-10)$ 21,22

* $Ar^* + 2Ar \rightarrow Ar_2^* + Ar$ $1(-32)$ 20,21,41

$Ar^* + Xe + Ar \rightarrow ArXe^* + Ar$ $3(-31)$ 47

* $Ar_2^*(^3\Sigma_u^+) + Xe \rightarrow Xe^* + 2Ar$ $4.3(-10)$ 55

$Ar^{**} + Ar \rightarrow Ar^{**} + Ar$ $1(-11)$ 49

$Xe^*(6s') + Xe \rightarrow Xe^*(6p) + Xe$ $1(-11)$ 6

* $Xe^{**} + Ar \rightarrow Ar^* + Xe$ $4(-14)$ 50

* $Xe^* + 2Ar \rightarrow ArXe^* + Ar$ $6.7(-34)$ 21

* $Xe^* + Xe + Ar \rightarrow Xe_2^* + Ar$ $2.8(-32)$ 21,51,52

$Xe^* + 2Xe \rightarrow Xe_2^* + Xe$ $1.8(-32)$ 7

$Xe_2^* + Xe \rightarrow Xe + 2Xe$ $1(-11)$ 53

64

Table 4.(continued)

REACTION	RATE	REFERENCE
(e) PHOTON REACTIONS		
* $Ar_2^*(^3\Sigma_u^+) \rightarrow h\nu + 2Ar$	3.12(5)	48
* $Ar_2^*(^1\Sigma_u^+) \rightarrow h\nu + 2Ar$	2.4(8)	48
$h\nu + Ar_2^* \rightarrow Ar_2^+ + e$	1(-18)	53,54
$Xe_2^*(^3\Sigma_u^+) \rightarrow h\nu + 2Xe$	1(7)	48
$Xe_2^*(^1\Sigma_u^+) \rightarrow h\nu + 2Xe$	1.8(8)	48
$h\nu + Xe_2^* \rightarrow Xe_2^+ + e$	1.9(-18)	53

*Asterick indicates processes included in the model.

†Rate constant in cm^3 sec^{-1} or cm^6 sec^{-1}, or transition probability in sec^{-1}.

65

7d and 10s, which comprise the Xe bulk in our model. They obtain total quenching rate constants of 1.8×10^{-30} and 3.0×10^{-10} cm^3 sec^{-1} for $Ar(^3P_2)$ and $Ar(^3P_0)$ respectively on the assumption that all the quenching results in xenon excitation. If a statistical distribution of $^3P_0$ and $^3P_2$ states is assumed for Ar4s, the net rate for Ar4s quenching will be 2.2×10^{-10} cm^3 sec^{-1}.

Gleason et al.[55] have measured the rate constant for quenching of $Ar_2^*(1u)$ by xenon to be 4.39×10^{-10} cm^3 sec^{-1} which is a factor of six less than that measured by Chesknovsky et al.[56] Since this energy transfer mechanism is hypothesized to be an important process for populating the laser levels, the model was run with both measured values of the quenching rate.

Another important mechanism for loss of Ar^* is electron impact ionization. The resulting ions will be rapidly converted to Ar_2^+ in three-body collisions. Shiu and Biondi[34] have measured the dissociative recombination rate of Ar_2^+. Although this rate is electron temperature dependent we have used a fixed rate of 3.6×10^{-8} cm^3 sec^{-1} corresponding to a temperature of ~ 5 eV which is approximately the mean energy during the discharge. It is unlikely that the temperature will fall below 1 eV due to superelastic heating, at which point the rate only will have increased to 9.7×10^{-8} cm^3 sec^{-1}.

Production of Ar_3^+ from Ar_2^+ can compete with dissociative recombination and quenching by xenon. The rate constants for production and dissociative recombination of Ar_3^+, 3×10^{-32} cm^6 sec^{-1} and 4.2×10^{-7} cm^3 sec^{-1} respectively, are estimated from the corresponding krypton and xenon rates cited by Werner et al.[7] and from the rate constants for argon calculated by Werner et al.[29] at lower electron temperatures.

The energy deposited into Ar bulk by recombination can be channeled into Ar4s by either collisional quenching or radiative cascade. The collisional process considered is three-body formation of Ar_2^{**} which predissociates into Ar4s. This same mechanism was invoked by Werner et al.[7] to explain the decrease in visible emission from the higher states in noble gases at high pressures. The three-body process is taken to be the rate limiting step with a rate constant equal to that for Ar_2^* production from Ar4s. This gives Ar bulk lifetimes of ~ 20 nsec at 1 atmosphere compared to radiative lifetimes of 50-100 nsec.[57] Since this three-body quench will dominate at high pressures we have not attempted to calculate a net radiative lifetime for the Ar bulk to Ar4s transition.

There are a number of mechanisms by which argon ions can transfer energy into xenon, but the rate constants for these processes have not been measured. The rate constant for

$$Ar_2^+ + Xe \rightarrow Xe^+ + Ar + Ar$$

67
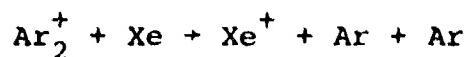
is estimated to be 5×10^{-10} cm^3 sec^{-1} from the result of Bohme
et al.[26] for the corresponding process in argon/krypton. The
rate constant for

$$Ar_2^+ + Xe \rightarrow Ar^+Xe + Ar$$
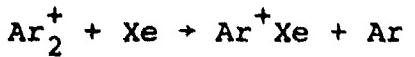
is estimated to be 2×10^{-10} cm^3 sec^{-1} from the Kr_2^+ + Xe rate
of Kebarle, et al.[27] Finally the rate constant for Penning
ionization of xenon by Ar bulk is estimated to be 3×10^{-10} cm^3
sec^{-1} since all of the other argon/xenon quenching rates are
essentially gas kinetic.

The treatment of the xenon kinetics is similar to that in
argon, but is complicated by the addition of the upper and
lower laser states. The $6s(3/2)_2$ and $6s(3/2)_1$ states are
grouped as Xe6s. The $6s'(1/2)_0$ and $6s'(1/2)_1$ states are not
considered separately in the model although Sadeghi and
Sabbagh[6] have shown that these levels are quenched via the
process

$$Xe^*(6s') + Xe \rightarrow Xe^*(6p) + Xe$$

with rate constants of 8.45×10^{-12} and 6.65×10^{-11} cm^3 sec^{-1}
respectively. Thus 6s' production will lead to an enhanced
population in the lower 6p levels.

The sublevels of the 6p and 5d manifold cannot be con-
sidered individually since there is no information on quench-
ing or excitation rates for particular sublevels. As a

result the modeling will not be able to indicate why any particular transition will lase.

Only a single atomic ion state in considered for each atom. For electron temperatures in the range of 1 to 5 eV and for gas pressures of an atmosphere, collisional-radiative recombination processes are unimportant and the dominant mechanism for Xe^+ destruction will be the formation of $ArXe^+$. Unfortunately the rates for $ArXe^+$ loss due to dissociative recombination and Xe_2^+ formation are unknown, although the recombination rate is probably at least as fast as for Xe_2^+ due to higher density of final states.[36] We have assumed a gas kinetic rate for conversion of $ArXe^+$ to Xe_2^+.

The branching ratio for the exit channels for dissociative recombination are not known. Shiu and co-workers[37] have observed the relative intensities of the transitions arising from decay of the exit states and find that for Te $\sim$ 300°K final states up to 7p are populated and for mean electron energies approaching 1 eV excited states up to 6f (11.7 eV) can be populated. All energetically allowed final states which could be monitored were observed to be populated. The 6p-6s transitions were observed to be most intense; however, the spectral response of the detector did allow observation of the 5d-6p transitions so the relative population of the 5d state cannot be deduced. Shiu is presumably also not able

69

to deduce what fraction of the 6p population arises from direct recombination rather than via radiative cascade. For the purposes of the model dissociative recombination is assumed to populate Xe bulk, Xe5d, and Xe6p. The relative branching ratios were varied in order to determine their effect on the predicted population densities.

The rate constants for electron-ion recombination and for the two- and three-body processes are temperature dependent. The temperature of the gas is taken to be room temperature, although it is expected that the temperature will be elevated slightly due to collision with electron and from dissociative recombination of ions into lower excited atomic states. The electron temperature used to obtain the rate constant for dissociative recombination in Xe_2^+ was calculated from the characteristic energy predicted by the Boltzmann code at each value of E/N. This method will be least accurate at very low E/N values where superelastic collisions will prevent the electron temperature from falling as rapidly as the code will predict the electron temperature used in calculating the dissociative recombination rate for the other ions was fixed at 5 eV.

Werner, et al.[29] have observed a decrease in electron density in e-beam pumped rare gas plasmas at high pressure which they attributed to a fast dissociative recombination of X_3^+ molecules. Xe_3^+ is most likely to be formed via

70

$$Xe_2^+ + Xe + Ar \rightarrow Xe_3^+ + Ar \quad .$$
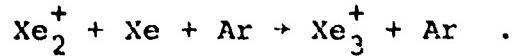
If the rate for this process is taken to be 6×10^{-32} cm^3 sec^{-1}, at 1 atm. total pressure the rate of Xe_3^+ formation will be 2×10^5 sec^{-1} compared with a loss rate of Xe_2^+ by dissociative recombination ($kT_e = 5eV$) of 8×10^6 sec^{-1}. Thus Xe_2^+ dissociative recombination will be the dominant electron loss mechanism and the dominant decay mechanism of Xe_2^+.

A possible alternative mechanism is

$$Xe_2^+ + Ar + Ar \rightarrow ArXe_2^+ + Ar \quad .$$

At one atmosphere total pressure the Xe_2^+ loss rate for this reaction is 3×10^7 sec^{-1}, assuming the rate constant for Xe_3^+ production, and a fast dissociative recombination rate, $\alpha_c = 9 \times 10^{-5}$ cm^3 sec^{-1} for Xe_3^+, will deplete the electron population. As yet this process has not been added to the model since there is considerable disagreement on the proper rates for clustered ion formation.[29]

The xenon bulk level is populated by dissociative recombination from the ions and by energy transfer from argon 4s levels and argon bulk. The rate of collisional quenching of Xe bulk by argon is estimated to be 1/500th of the transfer rate from argon 4s to xenon.

The upper and lower laser levels are populated by radiative transitions from xenon bulk, dissociative recombination of the

ions, and via energy transfer from Ar_2^* which is assumed to transfer into the 5d level alone. This assumption will cause the model to predict a higher laser power than is actually observed if this transfer mechanism is significant in inverting the Xe 5d/6p populations.

The assumption that the energy transfer from Ar_2^* occurs primarily into the upper laser level, $5d(3/2)_1$, is based upon the following reasoning. The energy available to be transferred can be deduced from the Ar_2^* emission spectrum which indicates that the 6p and 5d levels are most likely to be populated. As we noted earlier, if we assume that the energy transfer occurs via a dipole-dipole interaction potential then the most likely states to be populated are the $5d(3/2)_1$ and $5d(1/2)_1$ levels which are the only 5d and 6p levels with large dipole moments connecting them to the ground state. Since we do not know the branching ratio between these two 5d levels, we have assumed all of the transfer to occur into the $(3/2)_1$ level, although the $5d(1/2)_1$ level lies closer to the peak in the fluorescence energy distribution.

Energy transfer from Ar_2^* to xenon can also occur optically. In argon/xenon mixtures, Powell and Szöke[58] have observed structures on the Ar_2^* 126 nm band corresponding to absorption on the allowed $^1S_0 \cdot 5d(1/2)_1$ and $^1S_0 \cdot 6s'(1/2)_1$ transitions in xenon. They also observed collisionally induced absorption on several forbidden transitions to the 5d

72

and 6p manifolds. Since the absorption cross sections have not been measured we have not included optical energy transfer in the model.

The dominant loss mechanisms from the 6p and 5d levels are the laser output, radiative decay of Xe6p to Xe6s and Xe5d and Xe6p quenching to Xe6s in a three-body process involving Xe_2^{**} formation and predissociation into Xe6s similar to the mechanism invoked in argon.

Setser has reported some fast quench rates of the 4p levels of argon, $1-10 \times 10^{-11}$ cm^3 sec^{-1}, and the 5p levels in krypton.[59] These results are consistent with recent measurements of argon 4p level quenching by Nguyen and Sadeghi.[49] Apparently 20-50% of the excited atoms are quenched directly to the metastable. The remainder of the energy is distributed among various exit channels. This quenching process has been investigated in the model by adding a fast two-body quench of Xe6p to 6s in some of the calculations. A two-body mixing of 5d and 6p levels would be too difficult to model since it is not clear how the branching should be divided among final states.

The formation of ArXe* dimers has been included as a Xe6s quenching process. Leichner et al.[21] find a relatively small rate, 6.7×10^{-34} cm^6 sec^{-1} for the process

$$Xe(^3P_1) + 2Ar \rightarrow (ArXe)^* + Ar \quad .$$

73

Chestnovsky et al.[56] find no evidence for ArXe* dimer for-
mation although they note the presence of a possible KrXe*
dimer in high pressure Kr/Xe system. However, Powell and
Szöke[58] have observed collisionally induced radiation from
Xe*.

The formation of Xe_2^* from Xe6s is assumed to lead only to
U.V. emission and will limit the laser efficiency if there is
no energy recirculation from Xe6s up through the excited states.

Mulliken[8] predicts the presence of a large number of
bound and dissociative states of Xe_2^{**} within a few electron-
volts of the Xe_2^* ground state. The cross sections for excita-
tion of Xe_2^* are unknown, but could be approximated from the
atomic excitation cross sections. Excitation rates of $\sim 10^{-7}$
cm^3 sec^{-1} would allow Xe_2^* excitation to compete with radiative
decay and thereby retard the depletion of excited xenon atoms.
This excitation mechanism has not been added to the model.

3.1.3 Radiative Lifetimes and Branching Ratios

In order to include the effects of cascade pumping of
the Xe5d level from higher lying levels the transition pro-
babilities among all levels up to 10s were calculated in
xenon. The transition probability is given by

$$A = \frac{2.02 \times 10^{18}}{(2J_m+1)\lambda^3} S_{mn} \quad (sec^{-1})$$

where the absolute line strength S_{mn} is expressed as the product of a relative line strength term, which describes the relative probability for transitions between levels of the same orbital angular momenta, and a reduced matrix element of the dipole operator which gives the probability for transitions between states of different orbital angular momenta. The relative line strengths are tabulated by Statz, et al.,[60] but must be corrected by a factor of 3.[61] The reduced matrix elements may be expressed in terms of the integral of the product of the initial and final radial wave functions multiplied by $\hat{r}$. This integral has been calculated in the Coulomb approximation, i.e., with hydrogenic wave functions, by Bates and Damgaard and they have tabulated their results.[10] Unfortunately, the limits of the approximation are such that the results are expected to be least valid for transitions involving the 5d state.

Net transition rates in xenon from the bulk to 6s, 6p, and 5d were calculated by averaging the transition probabilities from the bulk to each of the lower levels, and then summing over the lower levels which belong to each state. Two different population distributions were assumed for the bulk: equal population in each level, and a population falling of as $e^{-\varepsilon_u \cdot 5eV}$ where ε_u was measured from the lowest 6s state. The results are given in Table 5. The net radiative lifetime for

TABLE 5

SOURCES FOR RADIATIVE TRANSITION PROBABILITIES, (SEC^{-1})

XENON BULK

TRANSITION	$\gamma(EQUAL)$ [1]	$\gamma(EXP)$ [2]	γ [3]
Bulk → 6s	3.6×10^6	2.2×10^5	7×10^6
→ 6p	5.4×10^6	3.2×10^6	4.4×10^6
→ 6s'	1.3×10^5	6.2×10^4	
→ 5d	3.8×10^6	$4. \times 10^6$	3.9×10^6

Ar_2^* [4]

$\gamma(^3\Sigma) = 3.1 \times 10^5$

$\gamma(^1\Sigma) = 2.4 \times 10^8$

$\gamma(NET) = 6.2 \times 10^7$

Xe_2^* [4]

$\gamma(^3\Sigma) = 1.0 \times 10^7$

$\gamma(^1\Sigma) = 1.8 \times 10^8$

$\gamma(NET) = 5.3 \times 10^7$

---

[1] Equal excited state populations.

[2] Population vary as $e^{-\epsilon/.5eV}$, where ϵ is the energy of the state measured from the lowest 6s level.

[3] Used in model.

[4] J.W. Keto, R.E. Gleason, Jr., and G.K. Walters, "Production Mechanisms and Radiative Lifetimes of Argon and Xenon Molecules Emitting in the Ultraviolet," Phys. Rev. Lett. 33, 1365-1368 (1974).

an individual bulk level was ∿ 100 nsec. The net radiative

lifetimes of Xe_2^* and Ar_2^*, given in Table 6, were calculated

on the assumption that the $^3\Sigma_u^+(1u)$ and $^1\Sigma_u^+(0_u^+)$ states were

populated proportionally to their statistical weights.

The rate for the xenon 6p-6s transition, 2.9×10^{-7} sec^{-1},

was calculated on the assumption that the 6p levels were

equally populated.

3.2 Bath Model

As a prelude to the detailed kinetics model, a simplified

quasi-equilibrium or Bath model will be outlined. This model

has the virtue that the detailed state dependence of the ex-

citation and relaxation is not incorporated explicitly and

this simplifies the kinetics while retaining the gross features.

First, we assume that the xenon excited state density is

approximately ten times the electron density or ∿ 2.5×10^{15}/cm^3.

This is consistent with the energy partitioning of the e-beam

and the first high E/N portion of the sustainer. Next we

assume that the excited xenon states are in a Boltzmann dis-

tribution such that excitation and relaxation may be thought of

as temperature changes. Shown in Figure 27 is a sketch of the

distributed xenon states along with other states thought rele-

vant and the gross kinetic processes. One must assume that

the upper laser level is perturbed from equilibrium in order

to create gain; the main problem is to find the equivalent

pumping rate to this level.

All xenon states whose energy is above the $5d[3/2]_1$ level are grouped as an upper bath; the remaining states are grouped as a lower bath. In Figure 28 is shown the stored energy density in these two baths versus the equivalent electronic temperature. At a temperature as high as .6 eV, 1/3 of the excited xenon population is still in the metastable level.

The pumping action due to electron excitation has associated with it a characteristic time $\tau_{exc} \simeq (\tilde{R} n_e)^{-1}$ where $\tilde{R}$ is some excitation rate. Using Seaton's[62,63] impact approximation for inelastic excitation in conjunction with our computer code which calculates A coefficients, state to state cross sections and rates were generated for a large number of levels in xenon. The Seaton rates agree to within factors of two with the Gryzinski rates for the low lying states, but have the advantage of predicting state to state cross sections according to optical selection rules and matrix elements. In the region of low E/N of interest, the calculated rates were all large ($> 10^{-7}$ cm^3/sec) resulting in values of $\tau_{exc} < 40$ nsec which is short compared with the characteristic circuit time scale of 325 nsec. Because of the rapid excitation and implied population rearrangement, we may treat the system in a quasi-static condition.

In order to achieve a steady state, the power lost by quenching must be balanced by electron excitation. For the

78

assumed excited state density, almost all the power deposited
in the gas in the low E/N region leads to excitation within
the baths and ionization. Thus steady state requires simply

$$\vec{J} \cdot \vec{E} = (U_u + U_\ell) \bar{\Gamma}$$

where Γ is some average damping. Taking as an example, a total
stored energy density of 140 $\mu j/cm^3$ and a deposited energy
density from the midpoint in Figure 28 of 7 kW/cm^3 results in
$\Gamma \sim 5 \times 10^7/sec$ which is only slightly faster than the average
radiative decay rate.

We can now address the kinetics in Figure 27 merely by
looking at various contributions to Γ which could lead to ex-
citation of the upper laser level. This is accomplished by
solving simple rate equations for the kinetics shown in Fig-
ure 27. The results will be expressed as an equivalent laser
saturated power density U_{SPD}, that is the maximum extractable
power density independent of threshold effects assuming that
the lower level decays infinitely fast. The resulting contri-
butions are:

A) Radiative cascade from the upper bath

$$U_{SPD} \simeq \beta_{RD} Q_{RD} U_u \Gamma_{rad}$$

B) Sequence $U_u \rightarrow Ar^* \rightarrow Ar_2^* \rightarrow 5d[3/2]_1$

$$U_{SPD} \simeq \beta_{MA} Q_{MA} \gamma_m \left(\frac{\gamma_T}{\gamma_T + A}\right) \left(\frac{\gamma^*}{\gamma + \gamma_m}\right) U_u$$

79
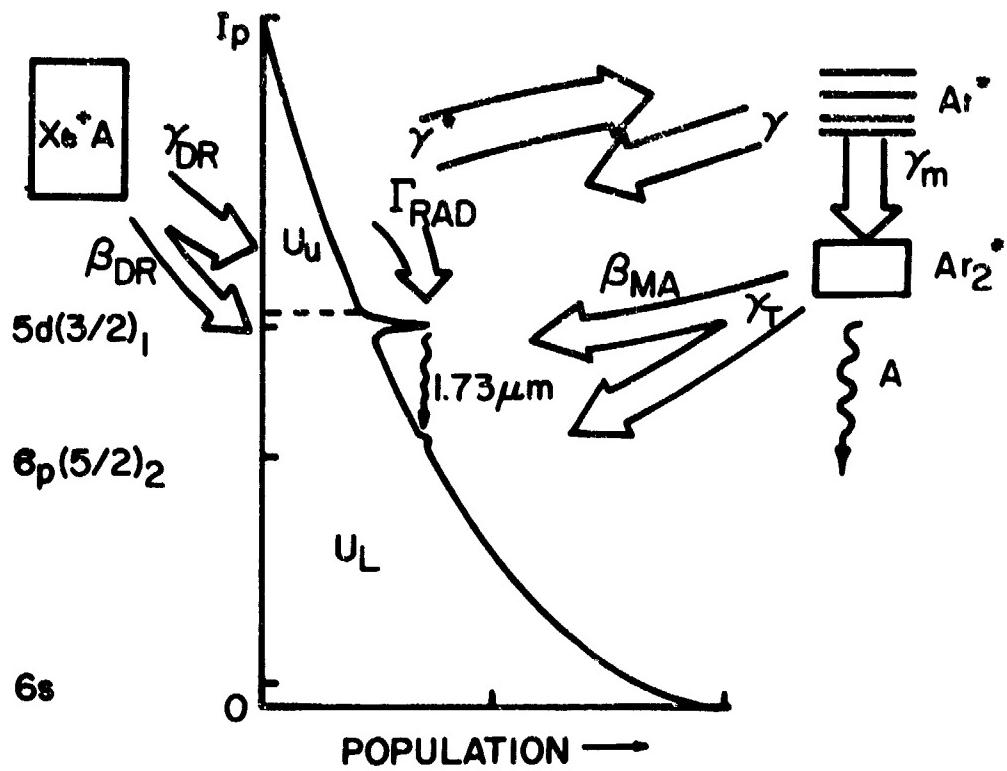
Figure 27. Boltzmann distribution of excited states in Xe showing gross collisional processes. Energy is measured with respect to the metastables. Species Xe$^+$A is some molecular ion or ions. See Table 5 for rates used in the modeling. All processes were evaluated for 150:1 ratio at 1 atmosphere.
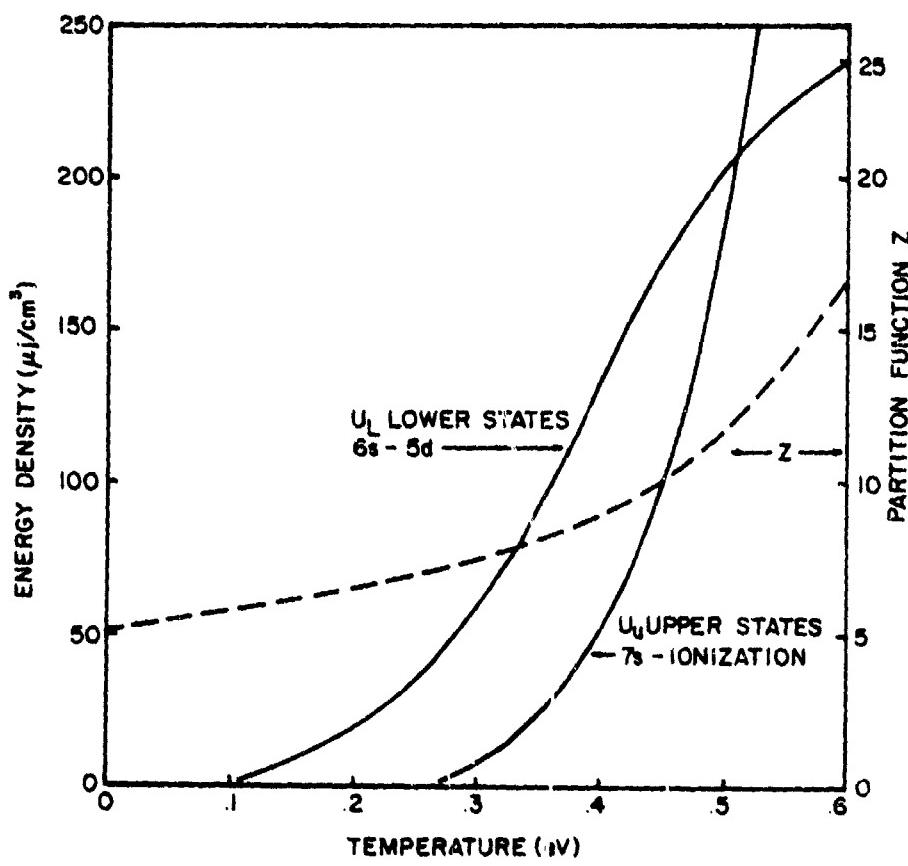
Figure 28. Electronic energy density and partition function Z in Xe. Total excited Xe density taken to be $2.5 \times 10^{15}/cm^3$. The energy is referenced to the metastable Xe level and level degeneracy is explicitly included.

C) Dissociative recombination

$$U_{SPD} \simeq \beta_{DR} \, Q_{DR} \, n_e^2 \, \gamma_{DR} \, I_p$$

where β_i is the equivalent branching ratio, Q_i the equivalent quantum efficiency ($h\nu_{laser}$/average energy in bath $\approx$ .2), the decay terms are in Figure 27, and I_p is the ionization potential of the Xe metastable.

As a specific example, values appropriate to the experiment will be discussed. Assume that $U_u \sim 100\mu j/cm^3$ as being representative of an extrema, then for $\Gamma_{rad} \sim 10^7/sec$, $\beta_{RD} = \beta_{DE} = .05$ from calculations: the above equations evaluate to

a) $U_{SPD} \sim 10 \ W/cm^3$ (Radiative)

b) $U_{SPD} \sim .1 \ \beta_{MA} \ W/cm^3$ (Ar_2^* Transfer)

c) $U_{SPD} \sim 35 \ W/cm^3$ (Recombination)

which should be compared with the average extracted power density of $\sim 200 \ W/cm^3$ (150:1 Ar:Xe @ 1 atm.). The branching ratio β_{MA} is not known, however even for an optimistic value of 1 the contribution to the total laser output by Ar_2^* transfer is small. This leaves as dominant contributions radiative cascade and dissociative recombination. If one invokes two-body quenching of states in U_u obeying optical selection rules with a rate ten times the radiative rate then ten times more power is potentially available ($100 \ W/cm^3$) by quenching.

82

Similarly, if the quenching is selective causing a channeling
or funneling of the states in U_u into the 5d(3/2)$_1$ level ef-
fectively raising β_{RD} again increasing the available power.
Both are certainly possible but unknowns.

Finally, if one permits collisional mixing of levels,
then it is also possible to have a "direct" excitation into
the 5d(3/2)$_1$ level from the 6p manifold due to electron impact.
The mixing would produce a population reduction or increase
creating "gain" on some transitions. The pumping to the upper
laser level would be attributed to electron excitation from
the 6p manifold. The electron impact excitation rates ob-
tained by using the Seaton cross sections and our solution of
the Boltzmann transport equation are given in Table 6 for
E/p $\sim$ .5 along with a simplified excitation picture. This
scheme would have associated with it a saturated power den-
sity

$$U_{SPD} = n_e \overline{R}(\overline{n}(6p) - n(5d(3/2)_2))h\omega_{laser}$$

where $\overline{R}$ is some manifold averaged rate and detailed balancing
is assumed. If the saturated power density is set to 100 W/cm^3
then

$$\overline{R}(\overline{n}(6p) - n(5d(3/2)_2)) \simeq 3\times10^6 \text{ sec}^{-1}$$

and the differential population should be 3×10^{13} or 3×10^{12} cm^{-3}

83

TABLE 6

CALCULATED RATES FOR ELECTRON EXCITATION

OF $6p \rightarrow 5d(3/2)_2$ TRANSITIONS
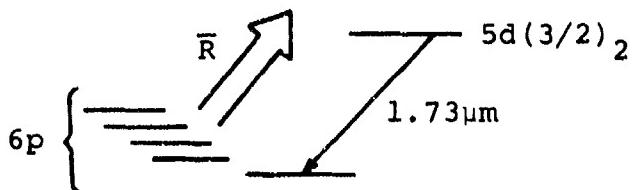
6p STATE	RATE $(cm^3 sec^{-1})$	$5d(3/2)_2 \rightarrow 6p$ LASER TRANSITION
$6p(1/2)_0$	1.2×10^{-6}	$2.65 \mu m$
$6p(3/2)_2$	1.4×10^{-7}	
$6p(3/2)_1$	1×10^{-6}	2.03
$6p(5/2)_3$		
$6p(5/2)_2$	5.7×10^{-8}	1.73
$6p(1/2)_1$	2×10^{-7}	

84

for $\bar{R}$ equal to 10^{-7} or 10^{-6} cm^3 sec^{-1}, respectively. At an electronic temperature of .5 eV and for the assumed excited state density, the p states all have a population greater than 10^{13} cm^{-3}, therefore this excitation mode may exist provided the lower laser level is perturbed by collisional quenching and/or radiative decay.

The results of this simple bath model thus indicate that argon does not contribute directly to the laser output via energy transfer through Ar_2^* but rather can only contribute to two-body quenching and to the electron mobility. It is only during the early discharge stage where Ar^* transfer becomes important. Similarly, radiative cascade and dissociative recombination may contribute to the observed laser action, the exact magnitude being dependent on the details of the recombination and nonradiative quenching processes. Finally, direct excitation of the laser level may proceed from the 6p levels provided the population of the lower level is quenched by some means, either collisionally or by radiative decay. Population perturbations of the 6p levels are evident in the laser spectra, laser time domain pictures in Figure 4, and the fluorescent intensities in Figure 16. All of the processes certainly may exist in any xenon discharge, however it is the special property of the high pressure case, large excited state density, which is thought responsible for the dramatic

85

laser performance simply because of the fractional power transfer data in Figures 22-24 and the implied energy recirculation discussed above.

3.3 Discharge Modeling

The differential equations describing the time variations of the population densities are coupled by the excitation and quenching rates discussed in the previous sections. In order to obtain a solution for the coupled differential equations we employ a routine written by Gear[64] which is intended to handle "stiff" equations, that is, equations for which the dependent variables change with widely differing rates. A calculation involving 13 coupled equations and a discharge duration of 1200 nsec typically requires 25 seconds of execution time on a CDC Cyber 175 computer.

In order to predict the laser power output we assume that the laser transition is saturated, so that the 5d and 6p populations are locked together. If K_+^N and K_-^N are the excitation and quenching mechanisms, other than the laser transition, for the Nth state then

$$\frac{d[Xe5d]}{dt} = K_+^{5d} - K_-^{5d} - S$$

and

$$\frac{d[Xe6p]}{dt} = K_+^{6p} - K_-^{6p} + S$$

86

where $S\left(\frac{hc}{\lambda}\right)$ is the saturated laser power density. If S is
large, the 5d and 6p populations will be nearly equal. Taking
the sum and difference of these equations yields the dif-
ferential equation for Xe5d + 6p and the equation for the in-
stantaneous power density:

$$\frac{d}{dt} [Xe5d + 6p] = \frac{1}{2} \left[(K_+^{5d} + K_+^{6p}) - (K_-^{5d} + K_-^{6p}) \right]$$

$$S = \frac{hc}{2\lambda}\left[(K_+^{5d} - K_+^{6p}) - (K_-^{5d} - K_-^{6p}) \right] .$$

Since there is no threshold inversion population necessary for
lasing in this approximation, the model is expected to over-
estimate the laser intensity.

The external circuit is modeled as a simple series LRC
circuit with C = .064 µf, L = 120 nH and R = 300 mΩ. No
secondary capacitors are included in the circuit. Since the
best current and voltage profiles are available for 1 atmos-
phere total pressure, a 150:1 ratio of Ar:Xe and a 23 kV
initial sustainer voltage, these parameters are used for most
of the modeling.

The instantaneous E/N in the discharge is calculated from
the voltage across the electrodes without regard to any volt-
age drop across a cathode the region. For glow discharges
in argon[65] the cathode fall at aluminum or copper electrodes
is about 100 volts which is as much as 30% of the predicted

discharge voltages for some modeling conditions. At our high discharge pressures the length of cathode-fall region will be negligible compared to the discharge length.

3.3.1   E-Beam Energy Deposition

The Ar/Xe mixture is preionized with a 150 kV, 250 ampere electron beam. The rate of excitation of the gas is given by

$$\frac{dN_i}{dt} = \frac{J}{e} \, NL(\epsilon) \frac{\eta_i}{E_i}$$

where N is the target gas density, $L(\epsilon)$ is the energy lost by electrons of energy ϵ per unit distance per unit target density, η_i is the excitation efficiency for the ith state and E_i is the energy lost in the excitation. The energy loss functions $L(\epsilon)$ used in the modeling were taken from the Berger-Seltzer[66] tables. Peterson[67] has tabulated the efficiencies η_i for excitation of many levels of argon as a function of the incident electron energy and has shown these efficiencies to be constant for incident energies above 100 eV. Thus if the electrons do not lose all of their energy in passing through the gas, as is the case for our system, the efficiencies remain constant over the deposition length. Because of the atomic similarity between argon and xenon, and because of the similarity of the energies necessary to produce an ion pair,

88

the efficiencies η_i for xenon are assumed to be the same as Peterson calculated for the corresponding states in argon.

The energy loss functions indicate that 20 keV of energy will be lost per 150 keV electron in passing through the .5 mil titanium foil window and that 11 keV and 27 keV will be deposited in the gas at 1 and 2 1/2 atmospheres. For a 200 nsec, 250 ampere electron pulse, this corresponds to a deposited energy of .5 Joule/atm.

The initial excited state population densities for the discharge were determined by applying the kinetics model to the period of e-beam preionization. The electron beam profile was taken to be a sine wave with a 400 nsec period and a 250 ampere peak current. The excited state populations were followed from t=0 to t=200 nsec at which time the e-beam pump was shut off and the populations were allowed to relax for 300 nsec. The densities predicted at 400 nsec, that is, 200 nsec after the end of the e-beam, were taken as the initial conditions for the discharge model. Since the gas was maintained neutral the initial electron density is the sum of the ion densities.

The modeling described above for the e-beam energy deposition suffers from the problems attendant to the use of a 'simple stopping power' approximation from which Berger and Seltzer obtained the $L(\varepsilon)$ values. The calculation thus

89

neglects multiple scattering of the initial e-beam electrons
which leads to larger stopping power as the beam energy de-
creases, scattering of electrons out of the beam by both the
target gas and Ti foil, reflection of the beam back into the
gas at the far electrode, and variations in energy deposition
with position in the target gas due to the divergence or
"blooming" of the beam. A complete treatment of these factors
in modeling the energy deposition would entail a sophisticated
Monte-Carlo calculation of the energy transport in three di-
mensions which is beyond the scope of the present modeling
program.

The results of a calculation of the energy deposition into
the rare gases obtained from a one-dimensional deposition code
which includes scattering were tabulated in a recent NRL tech-
nical report.[68] While these results cannot be applied di-
rectly to the problem of energy deposition into the Ar/Xe
mixtures, a consideration of the results for pure argon does
indicate why the laser output power decreases at high pressures.

The energy deposited into each centimeter path length of
the e-beam as a function of the argon pressure is shown in
Figure 29. These curves include the slowing down of the 150
keV beam in the .5 mil Ti foil. The figure also illustrates
the foil and electrode configuration. It is clear that as the
target gas density increases progressively more energy is

90
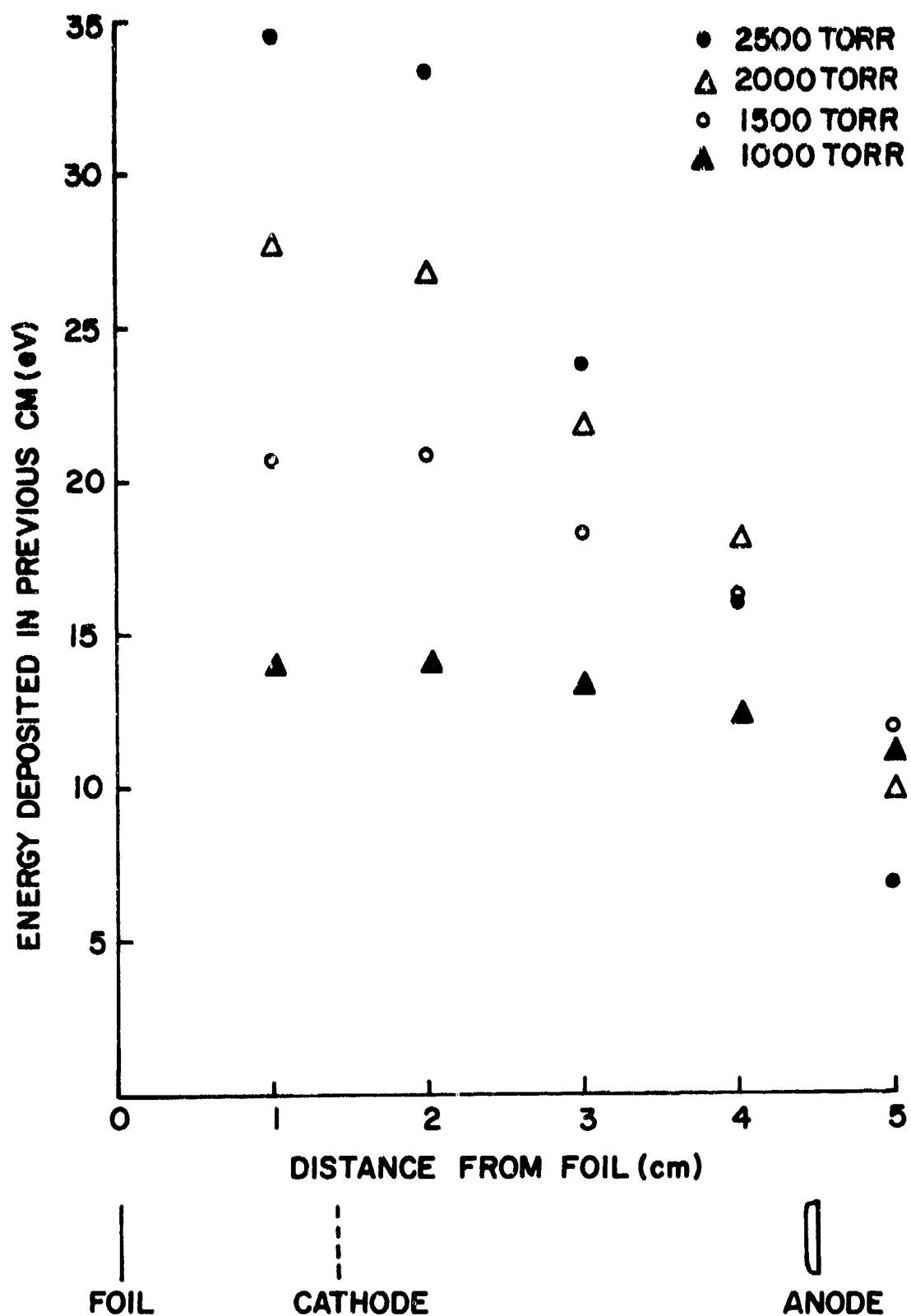
Figure 29. Energy deposited by a 150 keV electron into pure argon.
The illustration at bottom shows the relationship of
the graph to the discharge configuration.

deposited into the "dead" space between the foil and first
electrode and as a result less preionization of the gas be-
tween the electrodes will occur.

Figure 30 indicates the energy per electron deposited be-
tween the electrodes as a function of argon pressure. The
similarity between this curve and that of the laser energy out-
put vs pressure in Figure 3 suggests that the roll-off in
output energy is due to the decrease in preionization in the
discharge region. It is likely that the difference between
the curve peaks in Figures 30 and 3 is due to the presence of
xenon. Because of the large xenon mass, 42% of the incident
electrons in a 200 keV incident beam will be backscattered
out of the gas and they will carry out 62 keV of energy.[68]
Additionally, the stopping power of xenon is greater than that
of argon so that the presence of xenon will cause more of the
beam energy to be deposited into the dead space. Both of
these effects will cause the energy deposition peak of Fig-
ure 30 to be displaced to lower pressures in agreement with
the peak in Figure 3.

The NRL results indicate that the continuous slowing down
approximation of Berger and Seltzer underestimates the energy
deposited into the gas. Whereas the continuous slowing down
calculation predicts an energy deposition of .5 joule/atm,
Figure 30 indicates that for a 200 nsec, 250 ampere beam the
energy deposition is closer to 1 joule/atm.
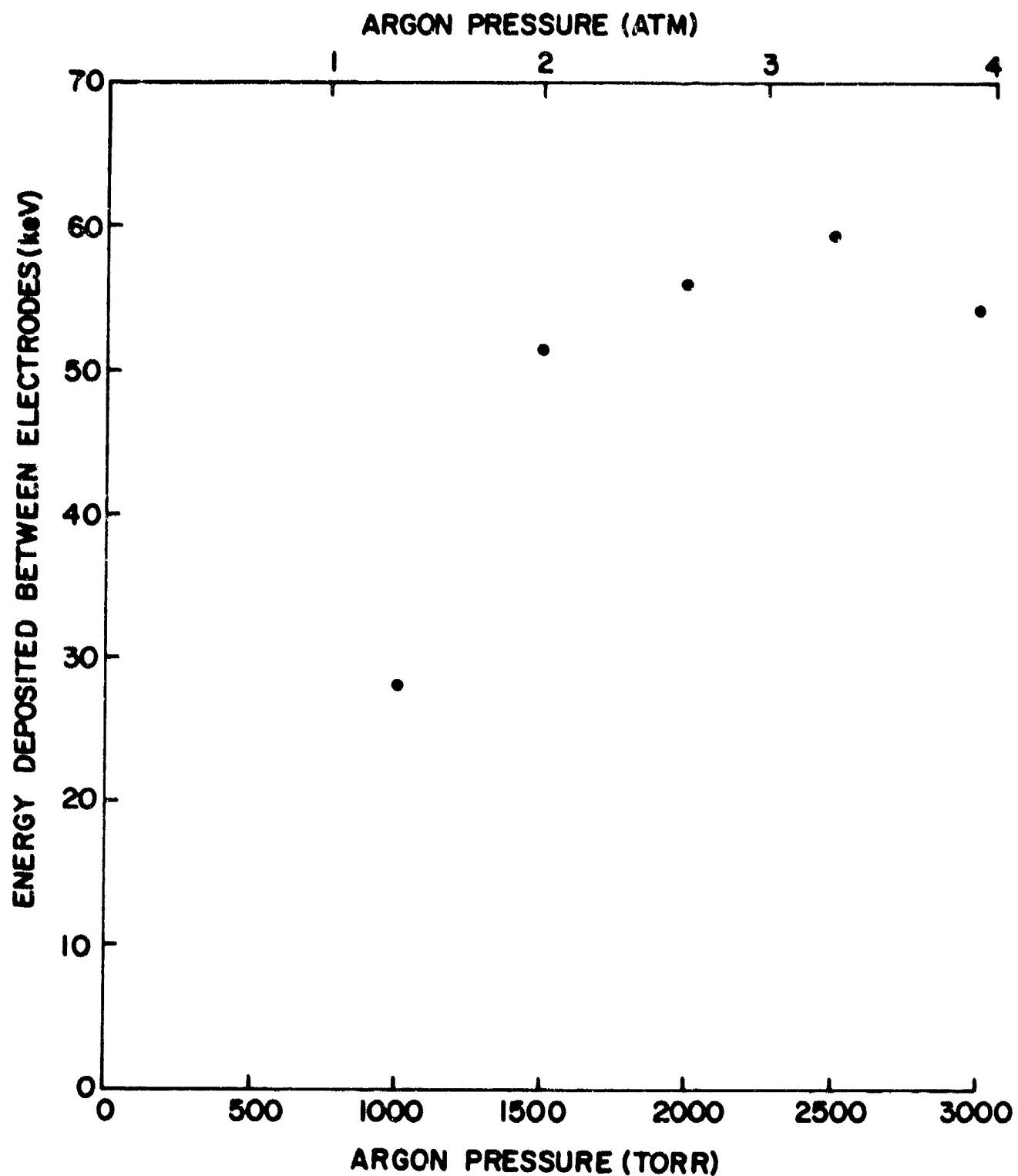
Figure 30. The total energy deposited between the electrodes only by a 150 keV electron into pure argon.

Figures 31 and 32 illustrate the time dependence of the excited state populations for 1 atm total pressure during the 200 nsec pulse and the subsequent 300 nsec relaxation time during which no further electron excitation processes occurred. At 400 nsec there are significant populations of metastable xenon, Xe_2^+ and $Xe(5d)$ and $Xe(6p)$, while the other populations have fallen below 10^{12} cm^{-3}. The metastable xenon population was calculated for two different loss mechanisms: three-body destruction with Ar + Ar and three-body destruction with Ar + Xe. The difference in metastable density at 400 nsec was a factor of five.

3.3.2 Discharge Evolution Model

The complete discharge model was assembled in a number of discrete steps. In the initial approximation only five electron excitation processes were assumed: $Xe(^1S_0)$ → 6s, $Xe(^1S_0)$ ionization, $Xe(6s)$ ionization, $Ar(^1S_0)$ → 4s, and $Ar(4s)$ ionization. All of the energy transfer and recombination processes discussed earlier were included. The initial conditions were taken to be an electron density of 10^{13} cm^{-3}, an equal Xe^+ ion density and all other populations equal to zero. In the second step of the modeling the secondary excitation processes $Xe(6s) - 6p$, $Xe(6s) - 5d$, $Xe(6s) - $ bulk, $Xe(6p) - 5d$, $Xe(6p) - $ bulk, $Xe(6p)$ ionization, $Xe(5d) - $ bulk, $Xe(5d)$ ionization and $Xe(bulk)$ ionization and superelastic scattering were added to
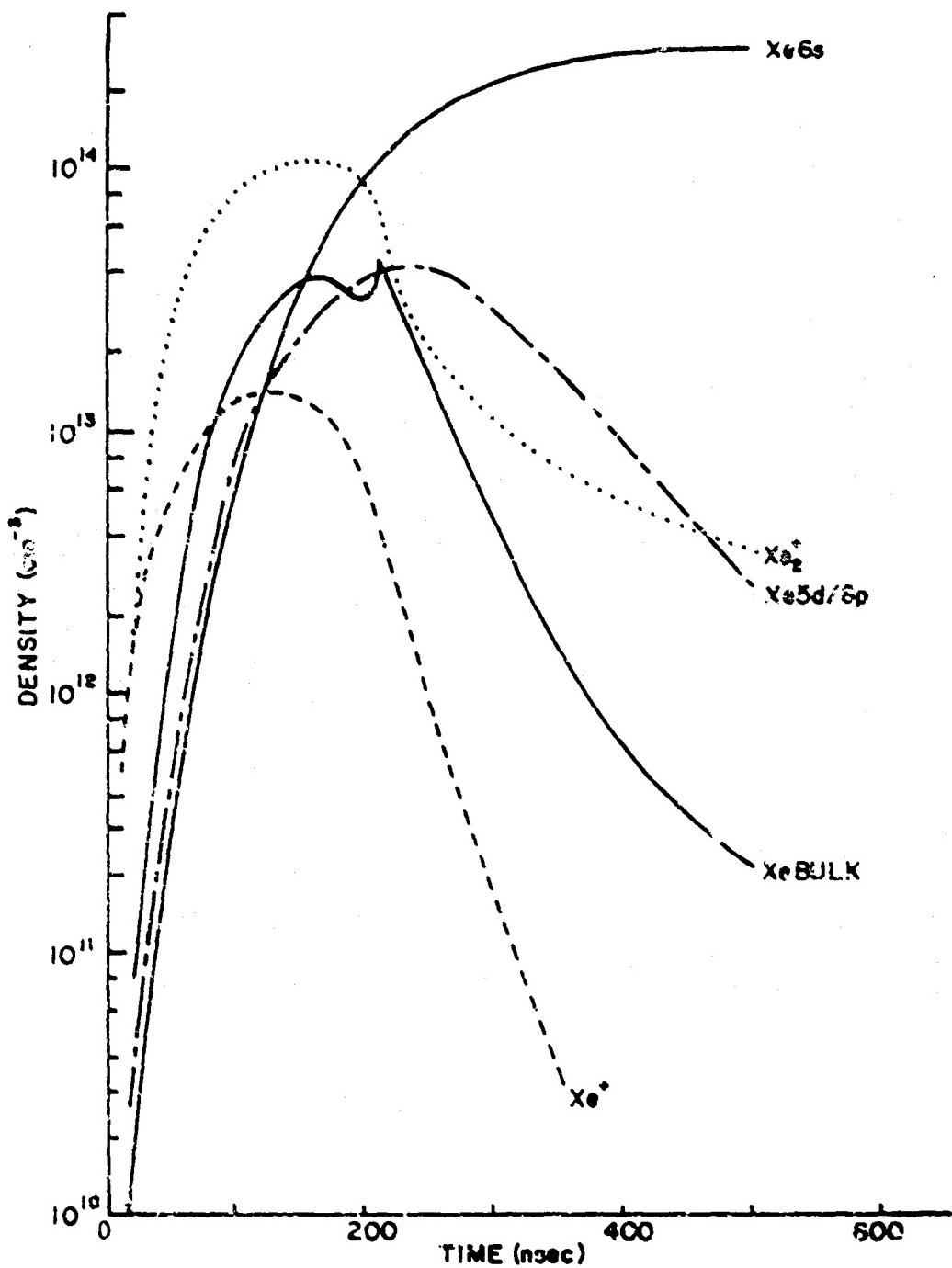
Fig.31. Time dependence of the densities of designated xenon states as a function of time as predicted by the kinetics model. The gas is pumped by the 250 ampere e-beam for 200 nsec as described in the text.

95
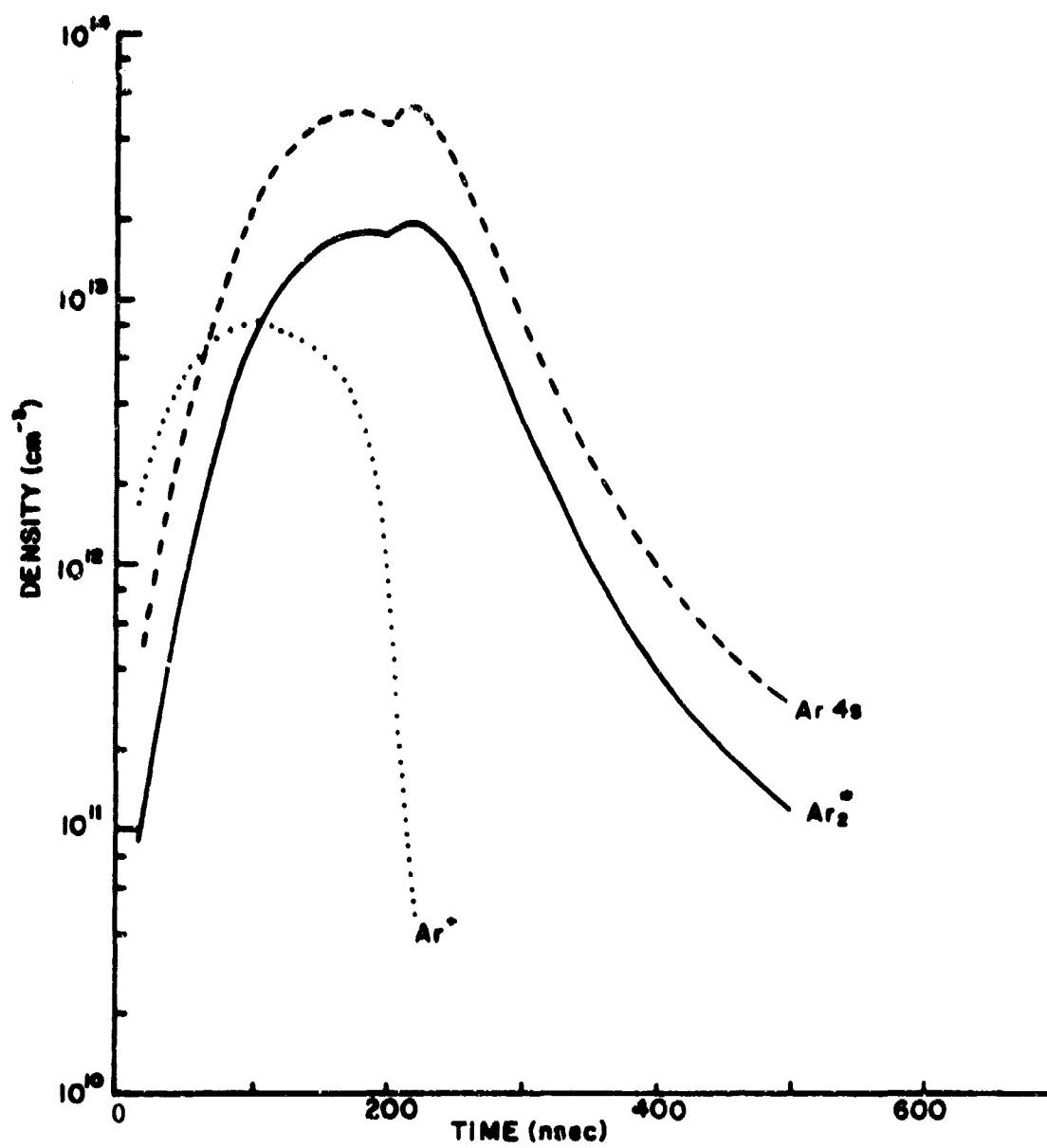
Fig.32. Time dependence of the designated argon densities. The conditions are as described in Fig.31.

the same kinetics and initial conditions. For the most re-
cent calculation the initial conditions were derived from the
electron-beam code described earlier. All of the modeling
was done for a 150:1 ratio of argon to xenon, 1 atmosphere
total pressure and a 23 kV sustainer.

Figure 33 shows the voltage and current profiles for the
first 750 nsec of the discharge as predicted by the initial
discharge approximation. These results should be compared
with the measured profiles in Figure 10.

The predicted voltage profile exhibits a 23 kvolt initial
peak followed by a low-voltage oscillation, in agreement with
the general behavior of the observed voltage profile. The
amplitude of the predicted low-voltage oscillation is about
a factor of two lower than for the observed oscillation and
the predicted curves tend to peak immediately after the zero-
crossing, whereas the observed curves peak essentially mid-
way between crossings.

The shape of the predicted current agrees nicely with
the observed current profile, although the predicted current
damps out too rapidly. The model predicts an initial peak
current of 12 kamp which is essentially the observed value.
The current is predicted to peak ∿ 200 nsec after the sus-
tainer is switched on, which agrees with the observed delay.
Our synchronization of current and voltage in Figure 10
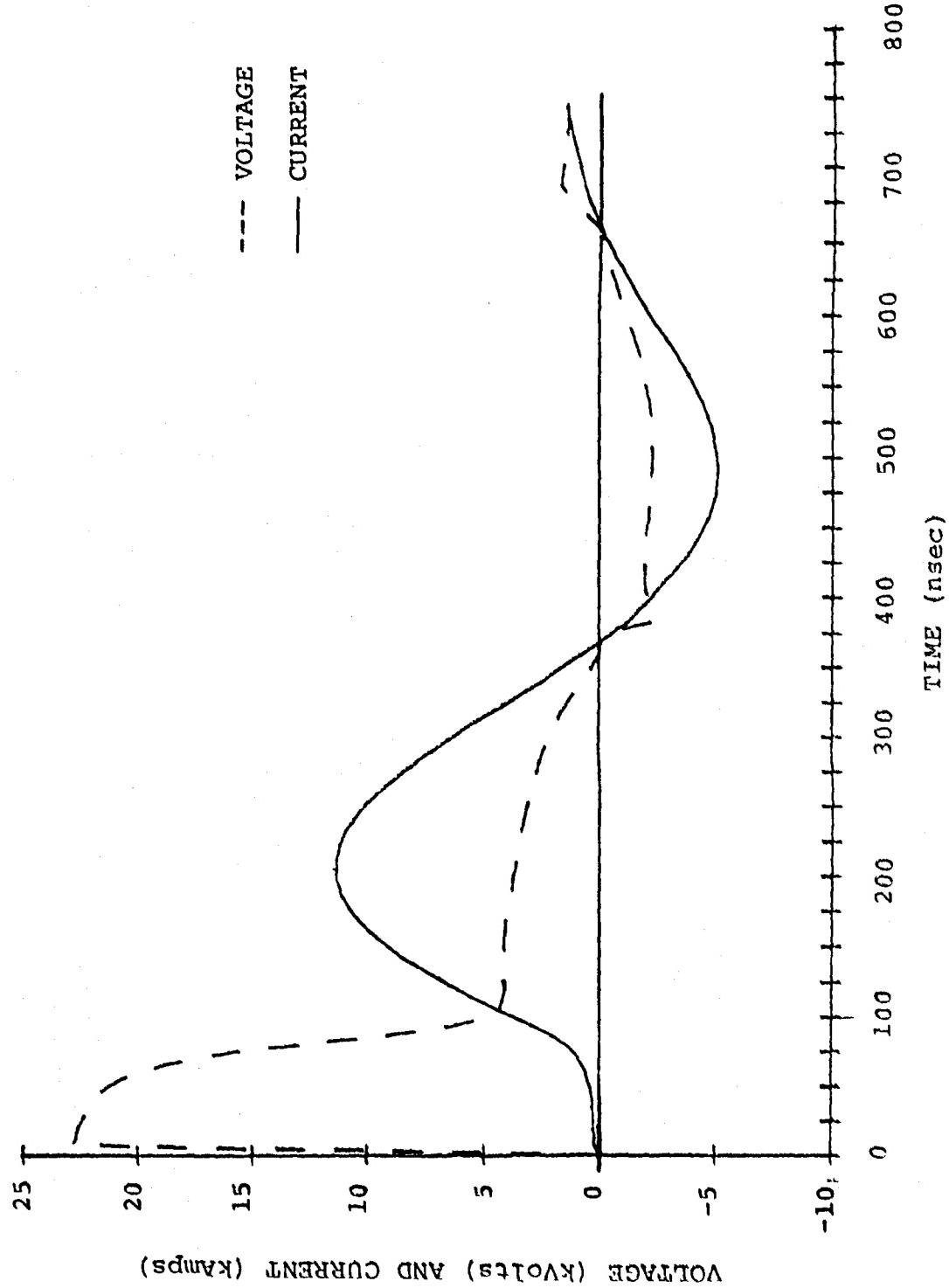
Fig. 33. Current and voltage profiles predicted by initial discharge model with five electron excitation processes.

indicates that the voltage passes through zero $\sim$ 100 nsec before the current does, whereas the model predicts that they pass through zero simultaneously.

Figure 34 shows the predicted saturated laser output versus time. Here again there are only 5 electron excitation processes included. The output is characterized by an initial spike followed by a series of peaks of decreasing amplitude modulated at one-half of the current and voltage oscillation frequencies. The total energy emitted in this pulse is 250 mJ, which is a factor of 3 larger than a typical laser pulse under these conditions. It should be remembered that due to the assumption of a saturated transition the model is expected to overpredict the laser intensity. The laser output peaks $\sim$ 250 nsec after the start of the discharge compared with $\sim$ 200 nsec for the first observed peak. The peaks in output power are delayed by $\sim$ 60 nsec from the current peaks, in agreement with the observed delay of $\sim$ 50 nsec.

In order to determine the contribution of energy transfer from excited argon into xenon towards the laser output the argon/xenon transfer rates were all set equal to zero. The predicted curve resembles Figure 34 except that the amplitude is decreased slightly and the small initial spike has been eliminated. The total energy in the pulse is 185 mJ. Thus this particular model predicts that at 1 atmosphere the transfer from argon to xenon contributes 1/4 of the laser output.

99
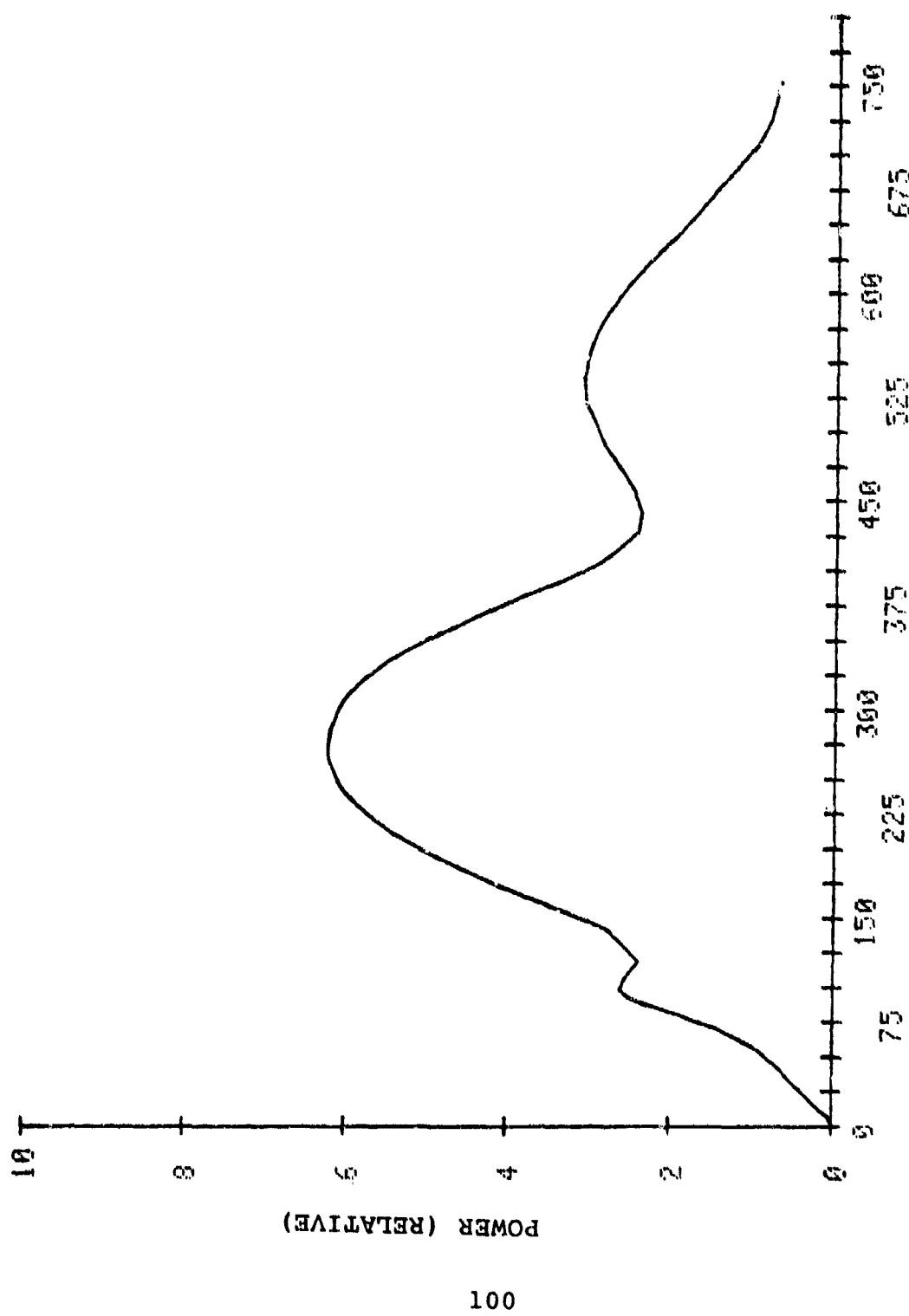
Fig. 34. Predicted saturated laser output versus time with 5 electron excitation processes.

Figures 35 and 36 illustrate the predicted variation in
the densities of various excited states and the electron den-
sity. The electron density rises rapidly from its assumed
initial value of 10^{13} cm^{-3} to $\sim 1 \times 10^{15}$ cm^{-3} and decreases
slowly with some modulation for the duration of the discharge.
The predicted peak density is a factor of 14 larger than the
7×10^{13} cm^{-3} anticipated from the free carrier absorption meas-
urements and a factor of 2 larger than the value inferred from
the current and voltage profiles.

The xenon 6s population density is seen in Figure 35 to
build up to an equilibrium population of 10^{15} cm^{-3}, about 1%
of the total xenon density. This reservoir of metastables
effectively constitutes a minority gas which can lase on the
5d-6p transition with a 34% quantum efficiency, and this is
in fact what the model predicts. The Xe$^+$ (not shown) and Xe$_2^+$
densities follow the electron density closely and are highly
modulated, essentially disappearing at the current and voltage
minima in the case of Xe$^+$. The Xe$^+$ ions are lost rapidly to
molecular ion formation, and the molecular ions recombine
rapidly to populate the laser levels. Since the effective
ground state of the lasing species is only 3.8 eV below the
ionization limit, the ionization-recombination process can pro-
ceed even at relatively small E/N, thus accounting for modulated
output even in the tail of the discharge.
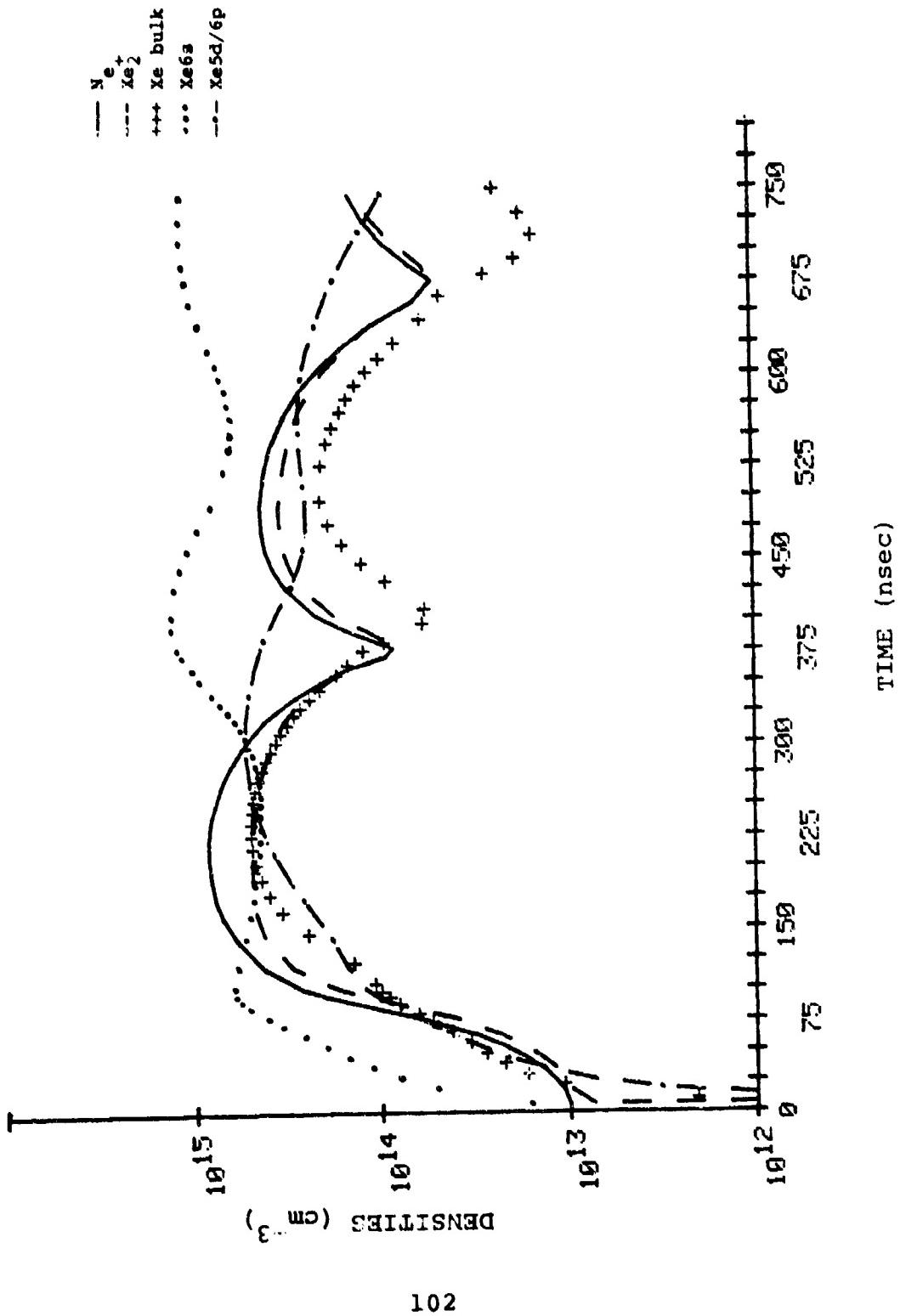
Fig. 35. Predicted time dependence of the densities of designated xenon excited states and of the free electron density.
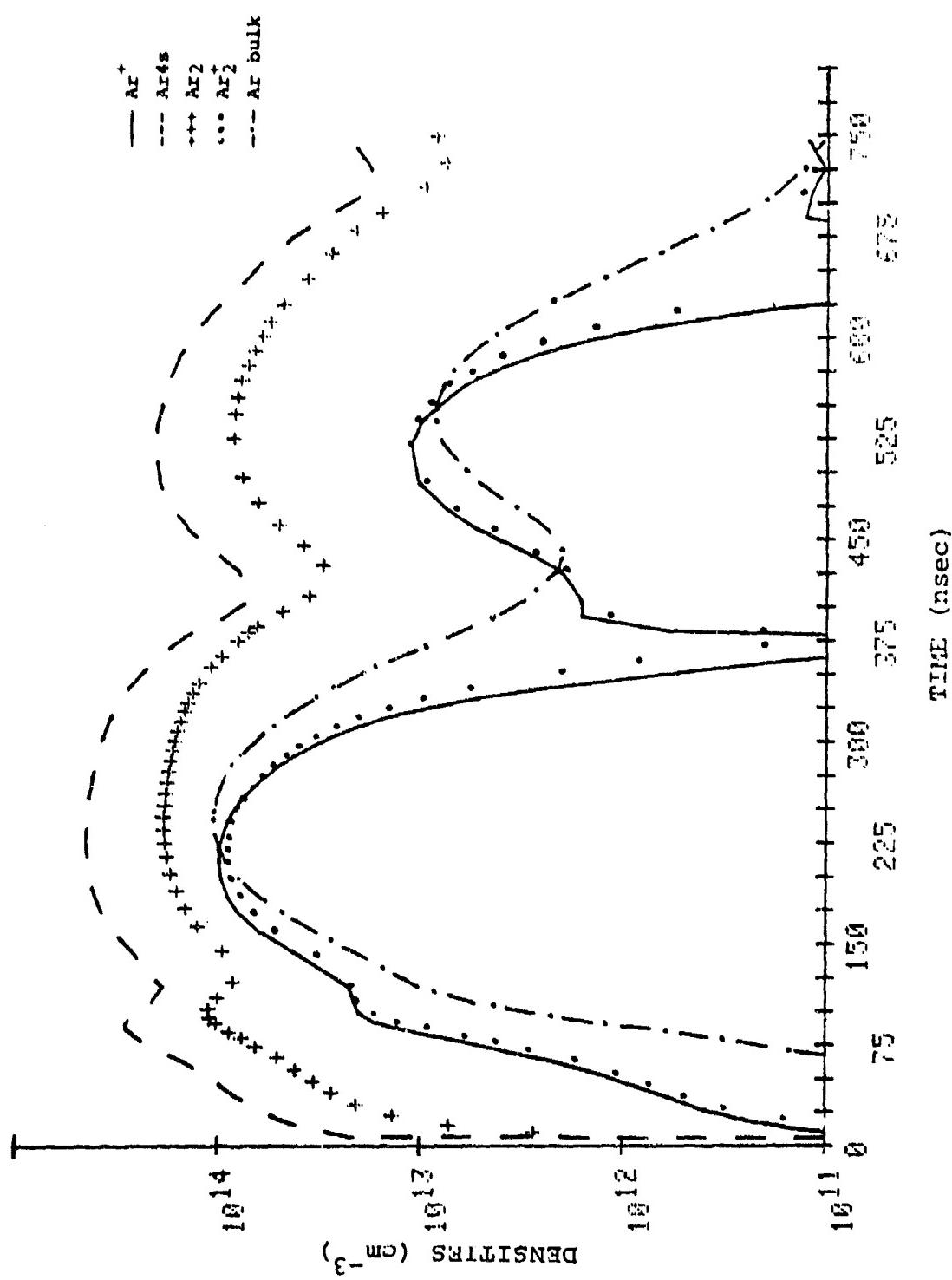
Fig. 36. Predicted time dependence of the densities of designated argon excited states.

The density of the Xe6s minority species does not de-
crease significantly during the 1.2 µsec discharge due to the
small loss rate from Xe_2^* formation:

$$Xe^* + Xe + Ar \rightarrow Xe_2^* + Ar$$

for which $k \sim 2.8\times10^{-32}$ cm^6 sec^{-1} and $\gamma \sim 10^5$ sec^{-1}. The popu-
lation could be depleted via the process

$$Xe^* + 2Ar \rightarrow ArXe^* + Ar$$
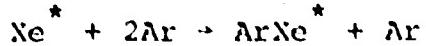
which would decrease the amplitude and possibly the duration of
the laser pulse. We have mentioned, however, that Leichner et
al.[21] find a relatively small rate, 6.7×10^{-34} cm^6 sec^{-1}, for
this process which makes quenching by 2Ar only about as fast
as by Ar + Xe. In the present model, therefore, the pulse
duration is determined by the rate of electron loss by recom-
bination.

The next step in the modeling of the discharge was to add
excitation processes among the excited xenon states, including
superelastic collisions. The addition of the Xe(6s-6p),
Xe(6s-5d), Xe(6s-bulk), Xe(6p-5d), Xe(6p-bulk), Xe(6p-ion),
Xe(5d-bulk), Xe(5d-ion) and Xe(bulk-ion) processes should en-
hance the populations of the ion states at the expense of the
neutrals. The Xe6s state should be strongly affected as the
population is not only depleted more rapidly by excitation,

104

but also because the rate of Xe6s formation will be reduced as the fraction of higher excited atoms which will radiate to Xe6s is reduced by excitation.

Figure 37 illustrates the predicted laser power profile for the conditions of Figure 10. There is clearly a series of three broad peaks in this profile. These peaks correspond in time with the extrema in the voltage and current profiles and thus would correspond most closely with the strong series of peaks in the observed power profiles. Although it is clearly resolved only on the second power peak there is additionally a second, smaller series of peaks immediately preceeding all except the first peak of the large series which corresponds most closely with the zero-crossing times in the voltage and current profiles. We therefore associate this second series of peaks with the smaller series in the observed power output. The first sharp peak at $\sim$ 50 nsec is apparently due to the response of the system to the initial large voltage spike, i.e., initial large E/N value, and is not associated with either series.

It is clear that the only agreement between the predicted and observed laser power profiles is in the prediction of two series of peaks, an initial power spike, and a decay of the peak intensities at longer times. The widths of the peaks, the relative amplitudes and spacings are not in as good agreement. The relative amplitudes of the predicted power peaks

105
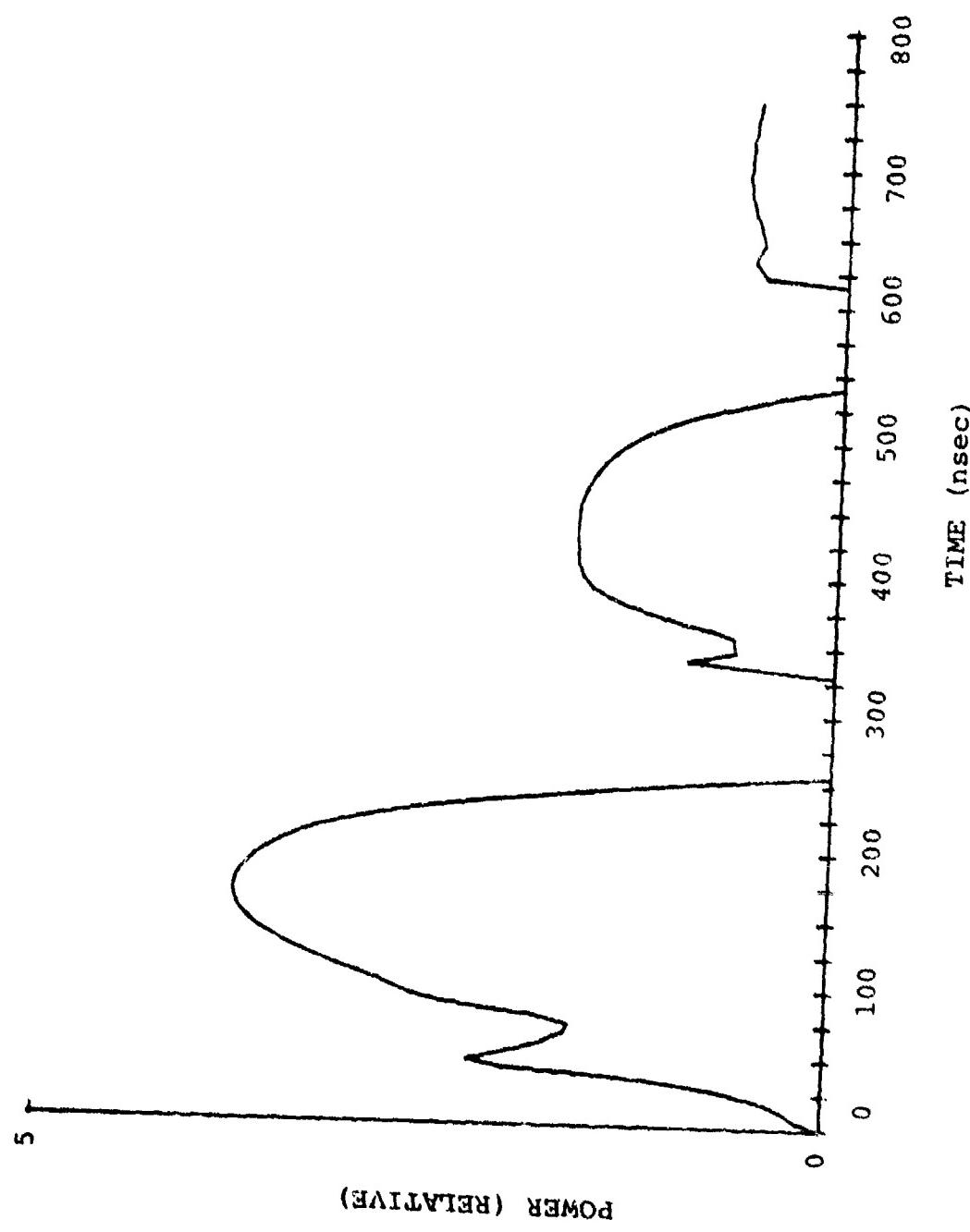
Fig. 37. Laser power profile predicted by the complete model for 150:1 argon/xenon mixture at 1 atmosphere. Branching of Xe^+ and $ArXe^+$ dissociative recombination is .3:.4:.3 for Xe bulk:Xe5d/6p:Xe6s.

are very sensitive to the rates of production and destruction of the 6p and 5d levels. It will become clear, however, that the two series of peaks are present for a wide variety of modeling conditions and that we can make specific statements about the kinetic processes which give rise to these peaks.

Figure 38 illustrates the current and voltage profiles predicted by the model. These should be compared with the true profiles of Figure 10. The voltage is predicted to rise to the 23 kvolt supply voltage and then to fall within 50 nsec. The peak height predicted is therefore higher than observed but the width is essentially correct. After the initial spike the voltage is predicted to rise again before beginning a series of low amplitude oscillations which damp out in time. The dip following the initial peak actually appears in some of the smoother experimental traces. The amplitudes of the second and subsequent peaks are too large, as the observed peaks do not exceed 1 kV, but the amplitudes of these predicted curves depend upon the instantaneous electron density and therefore can be varied by adjusting the rates of recombination or of $ArXe^+$ collisional dissociation, for example.

The predicted current profile agrees nicely with the observed curves, particularly the current at the first peak which is 12.5 amp, as observed. Compared with the correlated current and voltage curves of Figure 10, it appears that the current
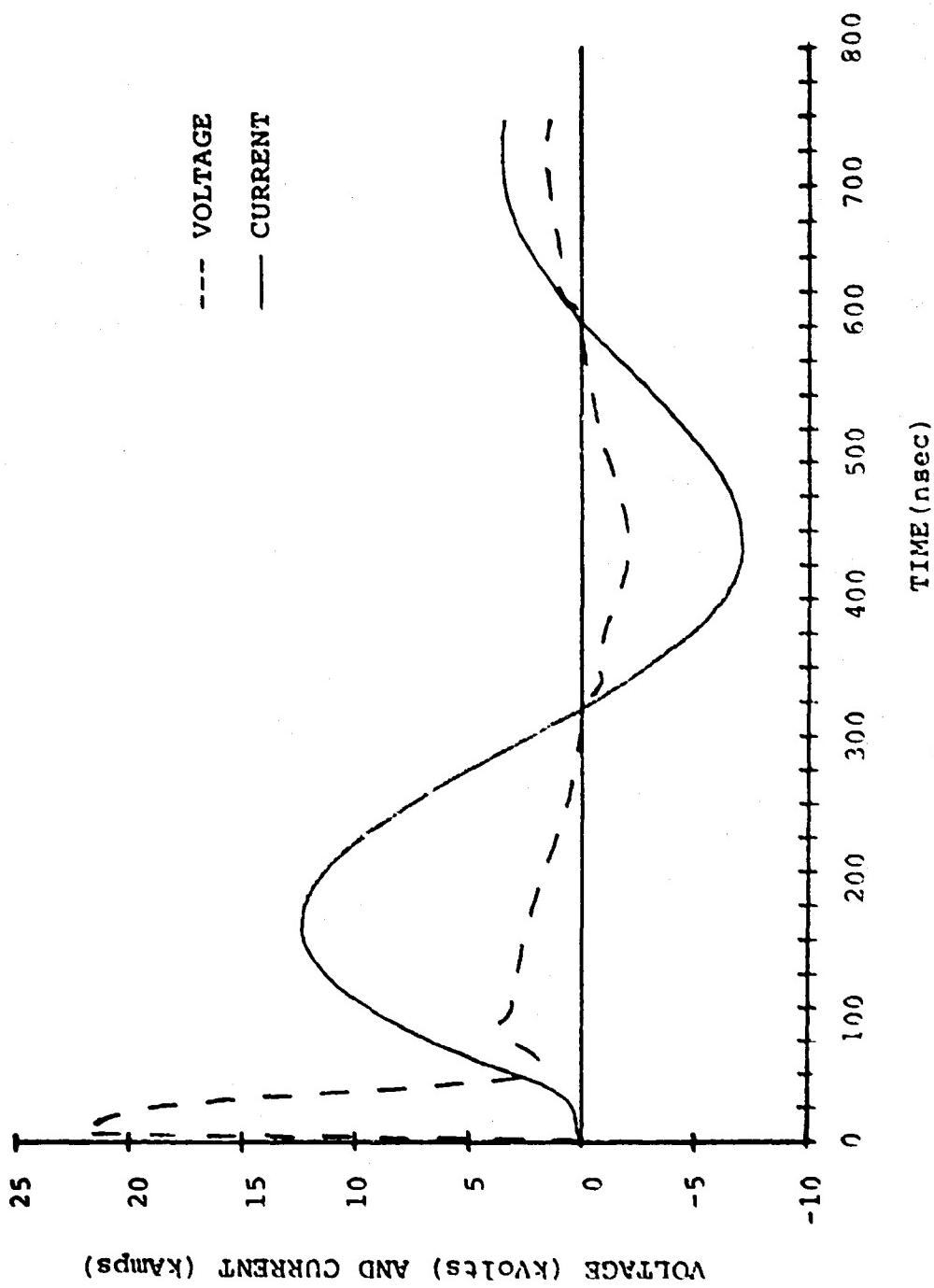
Figure 38. Current and voltage profiles corresponding to Figure 37.

in the model does not rise as soon after the discharge is initiated as the observed current. This is consistent with the large value for the initial voltage spike. If the current were to increase more rapidly, due to a more rapid rise in the electron density, then the discharge impedance would be reduced and the voltage would not attain such a large initial value.

The predicted time variations of various important population densities are shown in Figures 39 and 40. Before discussing particular states in detail, a brief look at the general behavior indicates that the populations cycle between two conditions: a condition of a high degree of ionization with energy stored in the Xe^+ and $ArXe^+$ levels during the high E/P regime and a condition of relatively low ionization where the excited state populations have collapsed into the lower metastable states. We observe lasing for both of these conditions, corresponding to the two series of power peaks. The conclusion to be drawn is that the prolonged laser output and the thereby increased energy per pulse is due to a cyclical ionization and recreation of the xenon metastable levels.

The current density in Figure 39 is predicted to rise to 10^{15} cm^{-3} and to then fall off in successive peaks. This density is significantly larger than the $\sim 1 \times 10^{-14}$ cm^{-3} current density inferred from the voltage-current profiles of Figure 38 and the 7×10^{13} cm^{-3} density anticipated from the free
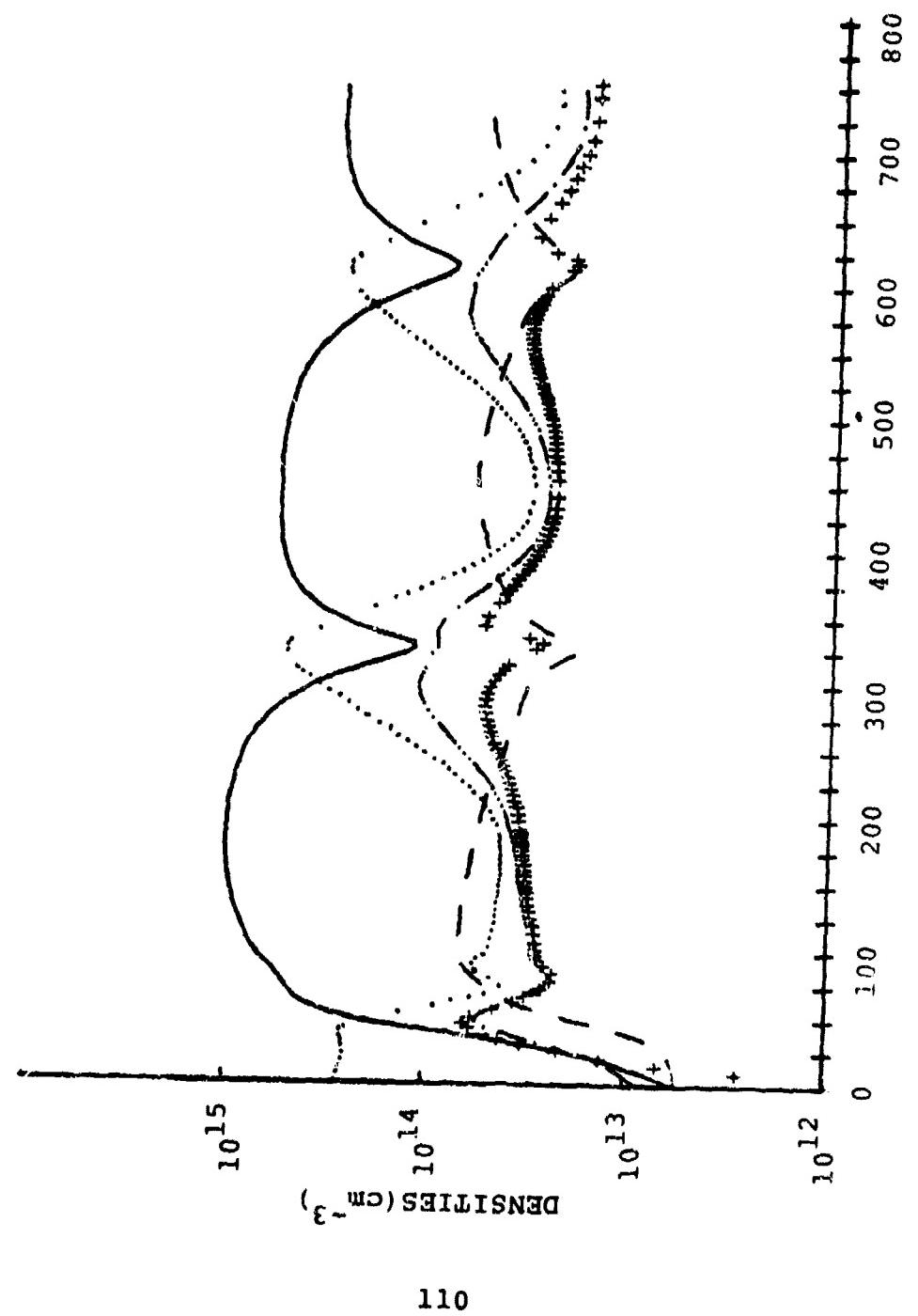
Figure 39. Density profiles corresponding to Figure 37.

110
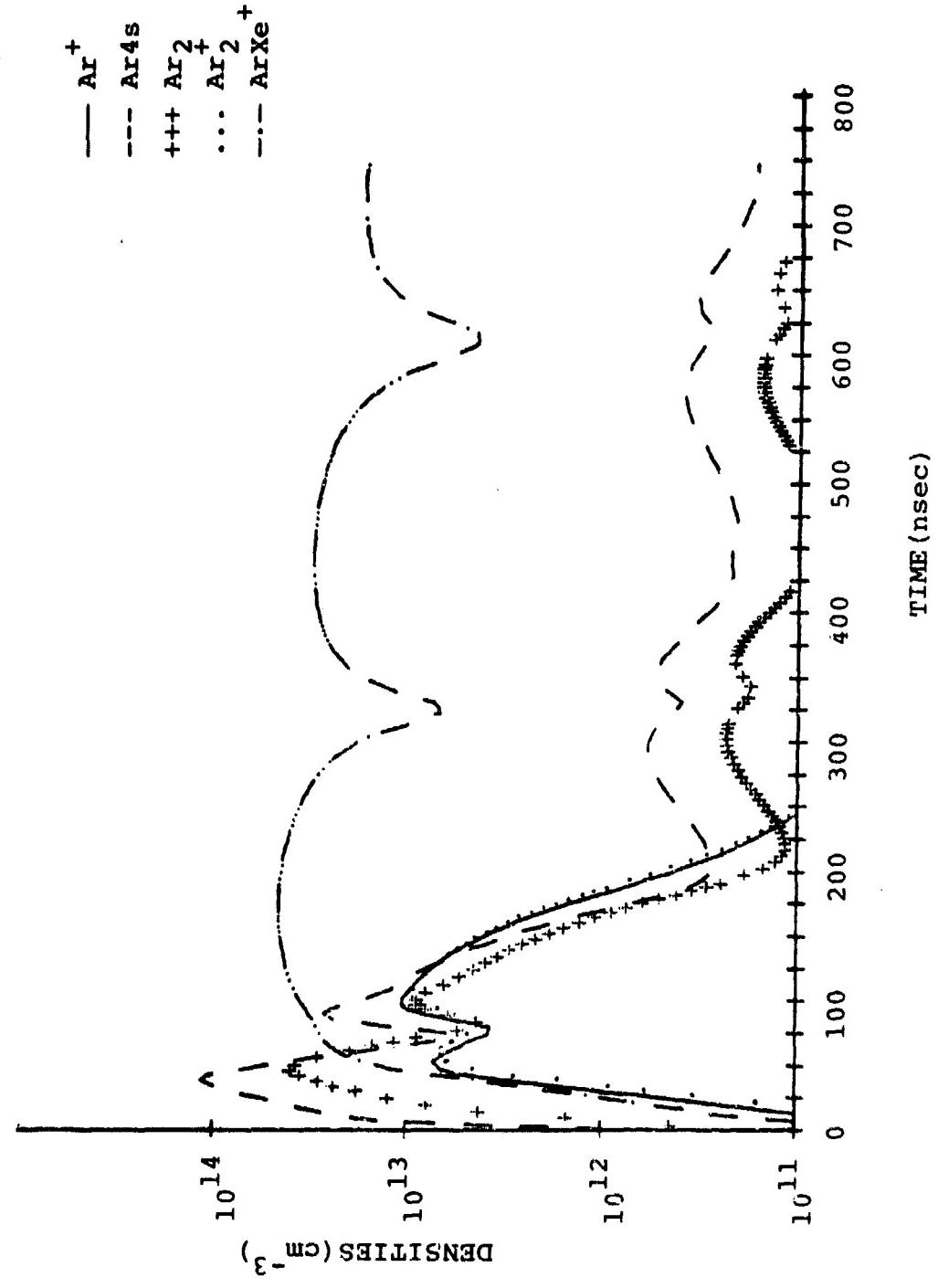
Figure 40. Argon density profiles corresponding to Figure 37.

111

carrier absorption measurements. It appears therefore that the predicted total ion densities may be too large by a factor of 5 or 10.

The difficulty in modeling the ion kinetics lies in the lack of information about $ArXe^+$. If we assume that the rate constant for the reaction

$$Xe^+ + Ar + Ar \rightarrow ArXe^+ + Ar$$
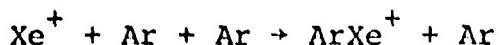
is the same as for Xe_2^+ production in the equivalent reaction in pure xenon, then $ArXe^+$ production becomes the dominant Xe^+ loss mechanism.

A particular problem associated with $ArXe^+$ is the stability of the ion against collisional dissociation. There is not very much information available about the potential energy curves of $ArXe^+$. Tanaka et al.[69] predict that $ArXe^+$ is bound very shallowly by $\lesssim .2$ eV whereas Powell and Szöke[58] indicate a well depth of $\sim .12$ eV. Such a shallowly bound state may be collisionally dissociated at a gas kinetic rate, but the true dissociation rate has not been measured. A rough estimate of the collisional dissociation rate assuming a harmonic oscillator potential yields a rate constant of 5×10^{-10} cm^3 sec^{-1}. For a fast dissociation rate, most of the ion density appears as Xe^+ and the rate of return of energy from the ions into the neutrals is slowed considerably.

The rate for dissociative recombination for ArXe$^+$ is unknown, but it presumably will be at least as fast as Xe$_2^+$ recombination due to the higher density of final states. The faster the rate taken for recombination the lower the ion density. Additionally, since ArXe$^+$ recombination has a significant effect upon the neutral population distributions, the branching of ArXe$^+$ into the various exit channels from Xe6s to Xe bulk will affect the laser power profile. The branching into the final states also effects the ion density since the bulk states which are produced are more readily ionized than the lower excited states.

Since the dominant ion population is Xe$^+$ for fast ArXe$^+$ dissociation there are three mechanisms for direct recombination from Xe$^+$ which would be mentioned: three-body, neutral stabilized recombination; collisional-radiative recombination and radiative recombination. The rate coefficient for the three-body neutral stabilized recombination has been calculated by Massey et al. [38] to be $\sim 10^{-26}$ cm^6 sec^{-1} at 300°K with a $T_e^{-5/2}$ dependence, which for an electron temperature of 3 eV and density of 10^{15} cm^{-3} gives an ion loss rate of 10^3 sec^{-1} at one atmosphere. Radiative recombination coefficients at 300°K are typically $2-4 \times 10^{-12}$ cm^3 sec^{-1} [39] with a temperature dependence of $\sim T_e^{-.7}$, which indicates a recombination rate of 10^2 sec^{-1} at 10^{15} electrons cm^{-3} and $T_e = 3$ eV.

113

Finally, Chen[70] has measured the collisional-radiative recombination rates in the rare gases. In xenon at $T_e = 300°K$ the rate is $\sim 10^{-12}$ cm^3 sec^{-1} for $n_e \sim 10^{15}$ cm^{-3} and $T_e \sim 2$ eV. Thus all of these recombination processes will be much slower than the molecular ion formation rates in the discharge.

The populations of the xenon bulk levels are farily stable, only varying between 2 and 8×10^{13} cm^{-3}. The population varies most rapidly as the system E/N begins to drop. As the electron temperature decreases, at 300 nsec, for example, the bulk population increases slightly since the recombination rate is increasing and the rate of bulk ionization decreases. As the electron temperature drops further and the ion populations become depleted the bulk population is reduced by radiative cascade and superelastic quenching. As the temperature increases the bulk population rises initially due to excitation of primarily the 6s level, which at low E/N contains the largest population, and then drops to its equilibrium value at high E/N as the 6s population becomes depleted and the bulk population is lost to ionization. This process is repeated during each cycle of the E/N.

The populations in the 5d and 6p levels, which are comparable to that of the bulk, undergo similar oscillations. It is clear that for both the bulk and lower levels recombination is most important in determining the populations at higher

114

values of E/N, since without a fast recombination rate these populations would be completely depleted by electron excitation. The branching ratio chosen for recombination into the bulk and lower states thus significantly affects the relative populations and the intensity of the predicted laser power. In Figures 37-39 the recombination for both Xe_2^+ and $ArXe^+$ was taken to be 30% into bulk, 40% into 5d and 30% into 6p. The effect of varying this ratio will be discussed later.

The xenon 6s level has the largest population at the initiation of the discharge. This population is diminished rapidly as the E/N and electron density increases due to stepwise ionization. When the E/N again decreases the excited state populations collapse into the 6s state. Thus the 6s state acts as a virtual ground state for the excited energy levels. As the E/N rises again the 6s population is rapidly excited and ionized, so that the excited state populations oscillate between being predominately held as ions (Xe^+) and as Xe6s.

We have caclulated the relative contributions of various processes toward Xe 5d production at various times during the discharge. During the first peak near 47 nsec the dominant excitation mechanisms are electron excitation of the lower levels, 6s and 6p, which contribute 39% and 25% of the excitation rate respectively. There is additionally a 16% contribution from superelastic quenching of Xe bulk. Since the ion

115

populations are still small there is a negligible contribution due to recombination. Energy transfer from Ar_2^* makes its largest contribution to this peak, 13% of the excitation rate. This first peak therefore can therefore be attributed to electron impact excitation of the lower xenon states at the peak E/N values and to energy transfer from the argon populations created at these early discharge times.

At the position of the largest power peak, 150 nsec into the discharge, the population mechanisms have changed considerably. Energy transfer from Ar_2^* now contributes less than 1% of the excitation. The contribution of 6s excitation has decreased from 39% to 16%, although the 6p contribution is about the same. Recombination of the ions now makes the largest contribution, 39%.

For the remainder of the discharge the relative contributions to 5d production remain almost constant except that the 6s to 5d excitation drops by a factor of two at the lowest E/N values. The output power falls to zero at low E/N due to rapid superelastic quenching of 5d to 6p. This rate was taken to be 3×10^{-7} cm^3 sec^{-1} for all E/N values. The electron impact mixing rates for 5d and 6p in general are difficult to calculate due to the overlap of the manifolds. The excitation and superelastic rates were obtained by averaging the rates based on the Gryzinski cross sections, but it is unlikely that the rates for transitions between these nearly degenerate

116

will be accurate. Figures 41 and 42 illustrate the effect
of reducing the rate of superelastic quenching of 6d to 6p
on the output power. Similar results are obtained if the 6p
to 5d excitation rate is increased. The total output energy
is increased substantially and the power does not decrease
to zero between peaks. It is clear from the modeling, however,
that the general structure of the peaks is not significantly
different from that of Figure 7. The bulk levels have assumed
a larger overall population and radiative decay from the bulk
has replaced superelastic quenching as the mechanism for popu-
lating the lower levels from the bulk.

The argon densities are relatively insensitive to the
modeling variations discussed so far, and a typical density
curve is shown in Figure 40 for the conditions of Figure 39.
In general these densities are lower than those in xenon and
only attain significant values for the first 200 nsec, during
which time they follow the variations in E/N. In the region
of lower E/N the Ar4s and Ar_2^* densities follow the variations
in the bulk density. This is due to the quenching of Xe bulk
by argon which maintains the excited argon population densities
which would otherwise be lost rapidly to quenching by xenon
and Ar_2^* radiative decay.

Energy transfer from Ar_2^* to 5d is not predicted to be an
important process except during the initial stages of the
discharge. Ar_2^* quenching contributes 13% of the 5d excitation

117
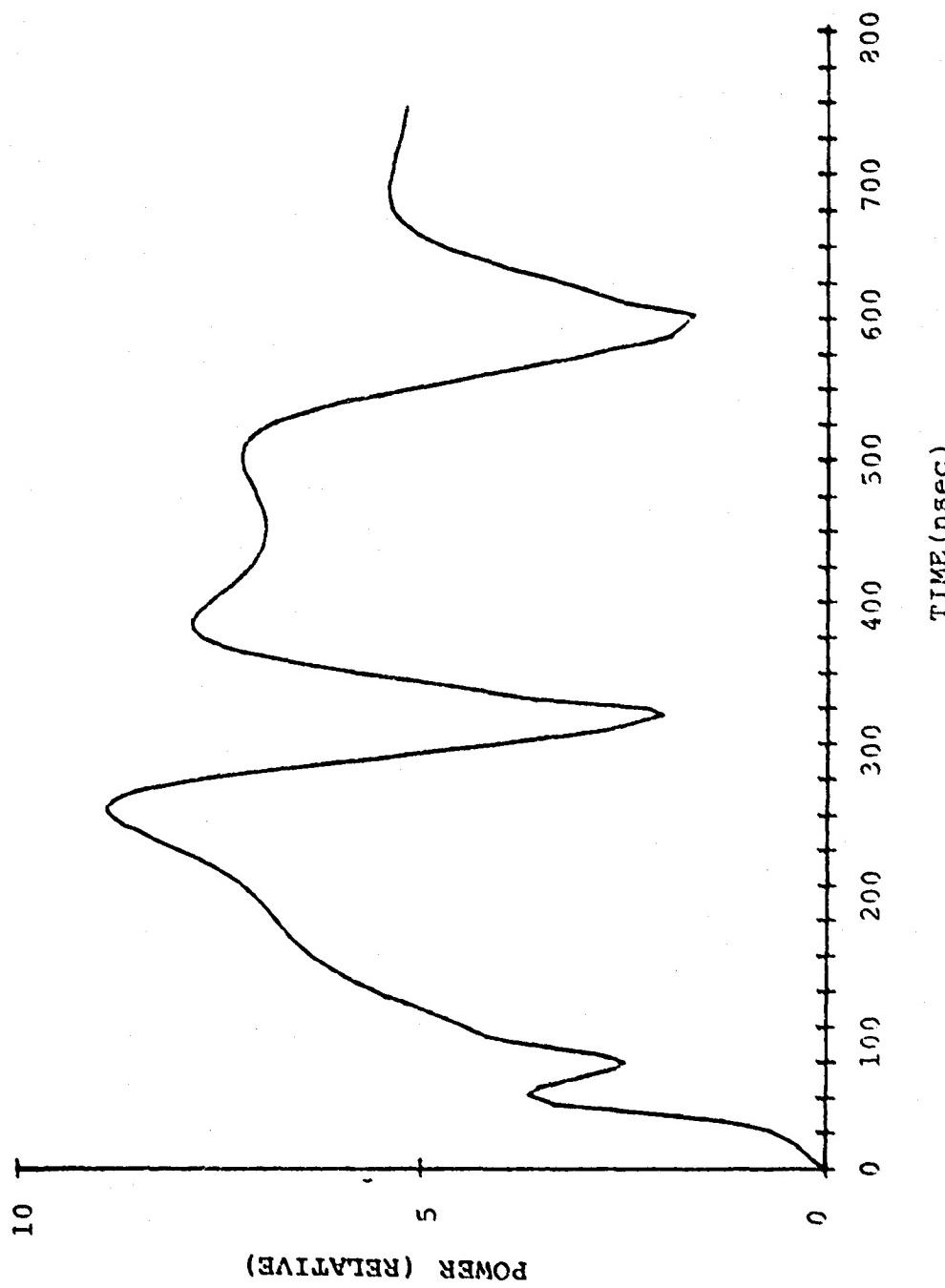
Figure 41. Power profile resulting from reducing the superelastic quenching of 6d to 6p. Compare with Figure 37.
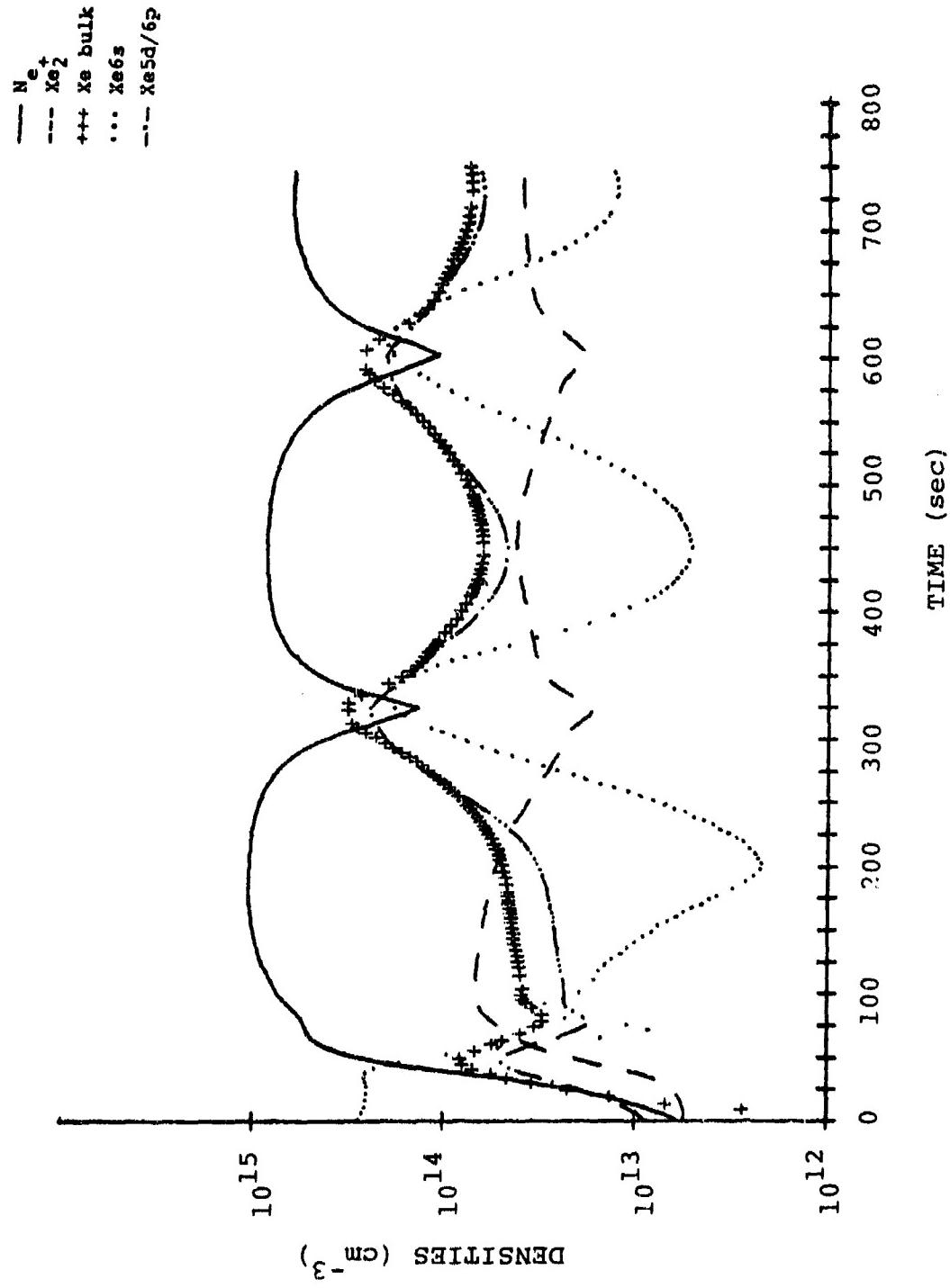
Figure 42. Density profiles resulting from reducing the superelastic quenching of 6d to 6p. Compare with Figure 39.

119

at the first power peak at 47 nsec but for the remainder of the discharge it contributes no more than 1% of the excitation.

The pressure dependent profiles of Figure 4 indicate that with increasing pressure the peak laser power increases but the pulse width decreases. Figures 43 and 44 indicate the results of increasing the total pressure to 2.5 atmospheres in the modeling. The Xe6s populations are now rapidly quenched in three-body collisions and the pulse length contracts to essentially a single peak. The amplitudes of the peak has increased 50%, but the laser energy has increased only marginally, from 104 to 110 mjoules. Thus the model does predict a decreasing pulse width and an increased peak height, but the quenching rates are much too large resulting in too narrow a pulse with too little energy.

It is clear in Figure 39 that the dominant loss of the excited state populations occurs at low E/N when the populations are held as Xe6s. Thus, while the electron density does not diminish during the high E/N regime it does not rise to its previous value following the period of minimum E/N. This implies that the rate of population loss is determined by the Xe6s quenching mechanisms: Xe_2^* and $ArXe^*$ production. In the present modeling Xe_2^* production leads to production of two ground state atoms. This assumption will overestimate the quenching by Xe_2^* formation since processes such as dissociative

120
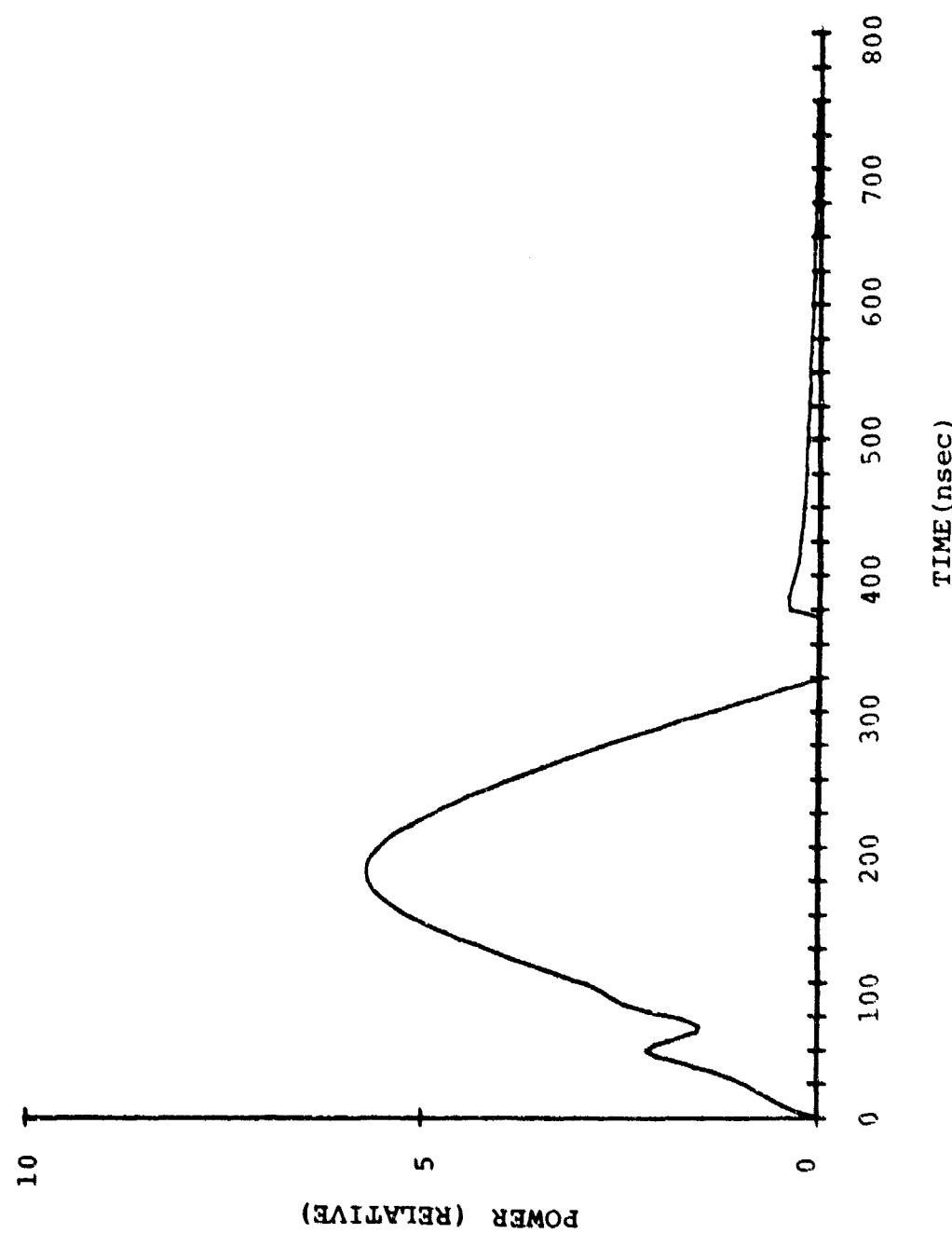
Figure 43. Power profile resulting from increasing the total pressure to 2.5 atmospheres. Compare with Figure 37.

121
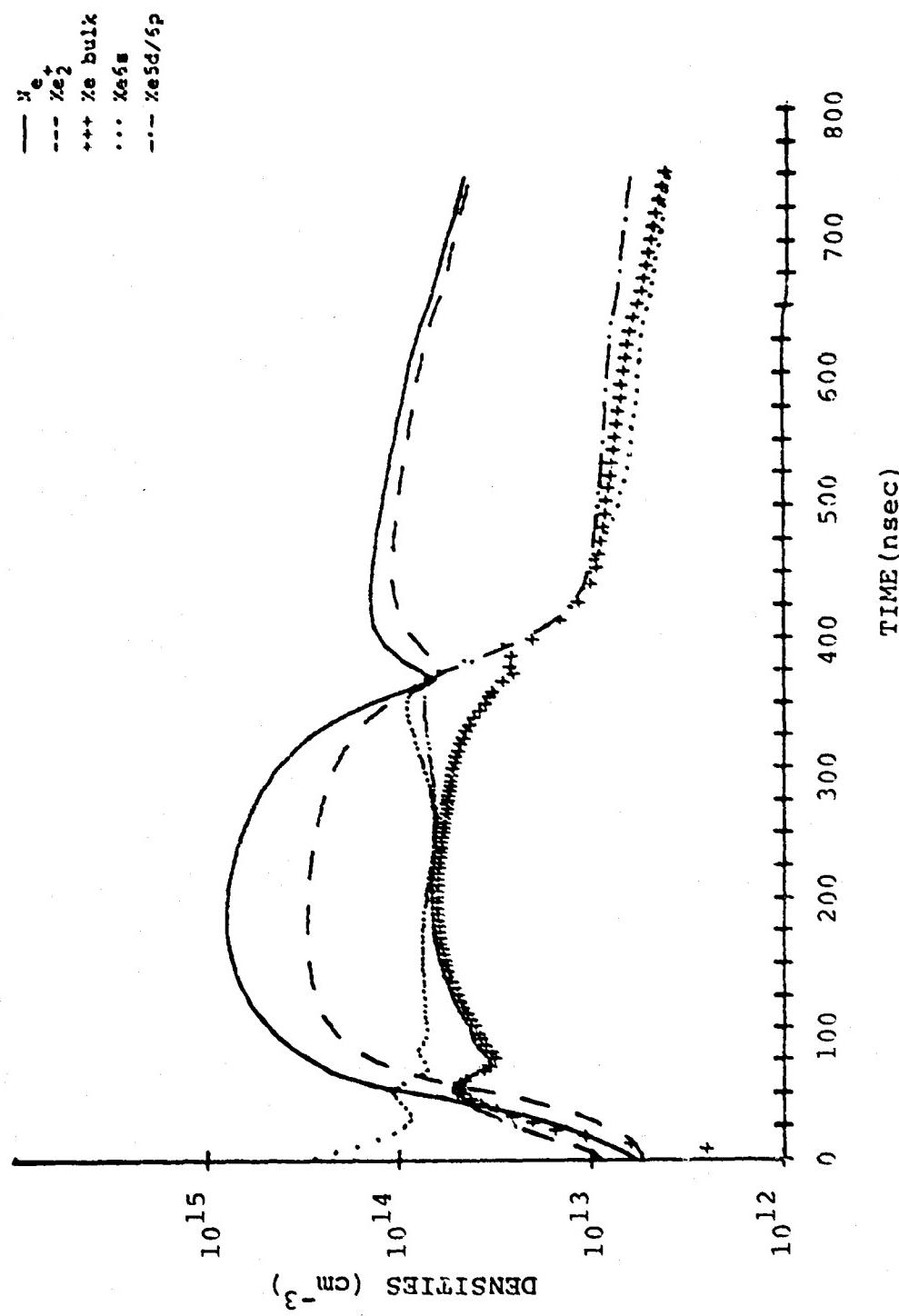
Figure 44. Density profiles resulting from increasing the total pressure to 2.5 atmospheres. Compare with Figure 39.

excitation can increase the Xe^{**} populations. Similarly $ArXe^*$ production is modeled as a total loss mechanism. We have noted the uncertainty in the production rate for $ArXe^*$ by

$$Ar + Ar + Xe^* \rightarrow ArXe^* + Ar .$$
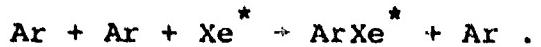
Since $ArXe^*$ will be shallowly bound, collisionally dissociation can repopulate the $Xe6s$ state as can Xe^{**} production by electron excitation. Thus the complete loss rates attributed to $ArXe^*$ and Xe_2^* production should over-estimate the rate of loss of the excited state densities.

The modeling so far as assumed that 40% of the $ArXe^+$ and Xe_2^+ recombination populates the 5d state while the remainder equally populates the 6p and bulk states. It is, of course, unlikely that the $ArXe^+$ and Xe_2^+ recombination branching ratios are equal, and in fact one would anticipate that $ArXe^+$ would recombine predominantly into the bulk due to both the large number of bulk states available as exit channels and to the large energy difference between the $ArXe^+$ energy and that of the 5d and lower states.

Figures 39, 45, and 46 illustrate the results of varying the branching of $ArXe^+$ and Xe_2^+ from complete recombination into Xe bulk to complete recombination into Xe6s. The power output profiles for the three conditions vary essentially only in amplitude, with a predicted 62 mJ output for total

123
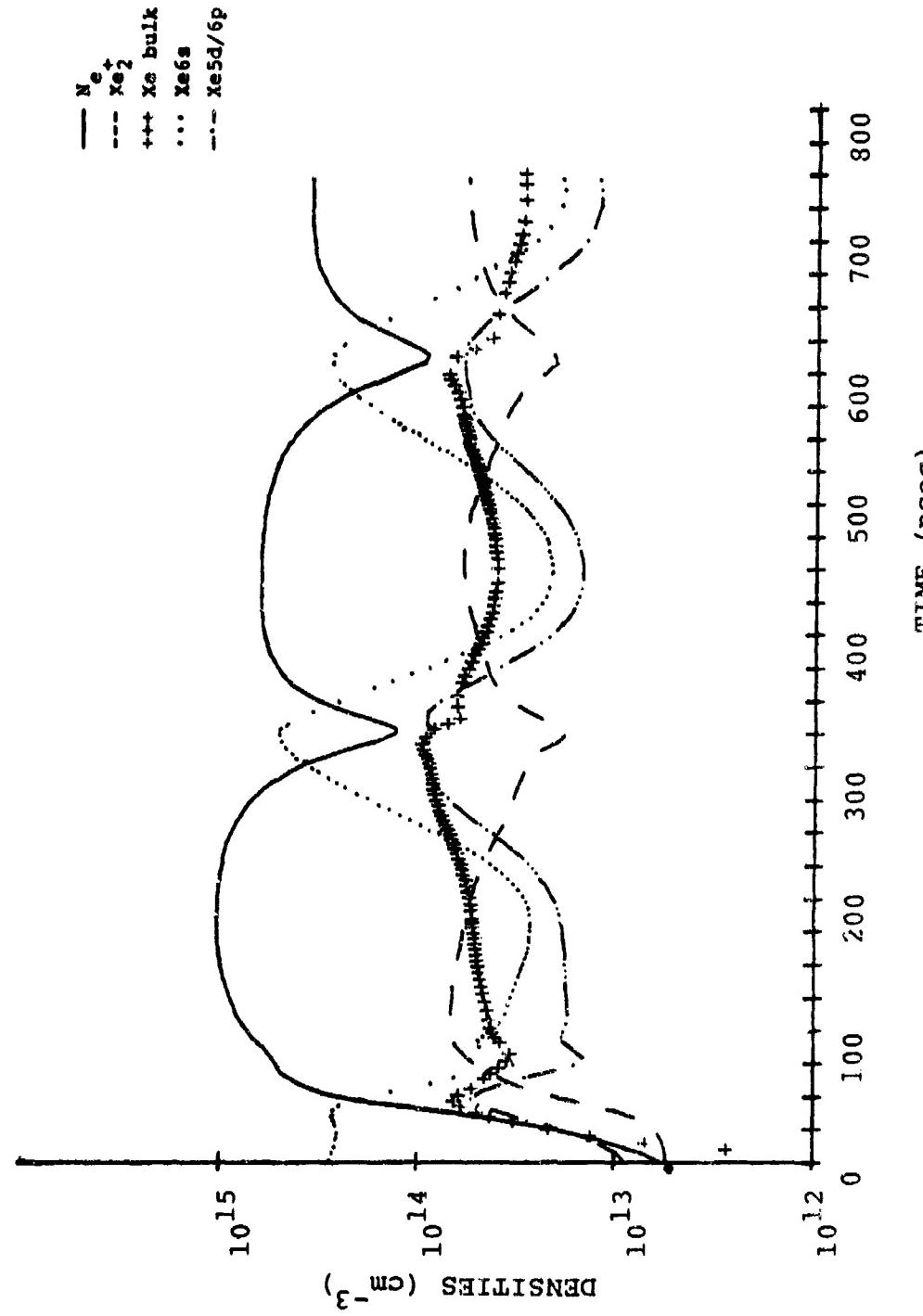
Figure 45. Density profiles resulting from Xe_2^+ and $ArXe^+$ recombination entirely into Xe bulk.

124
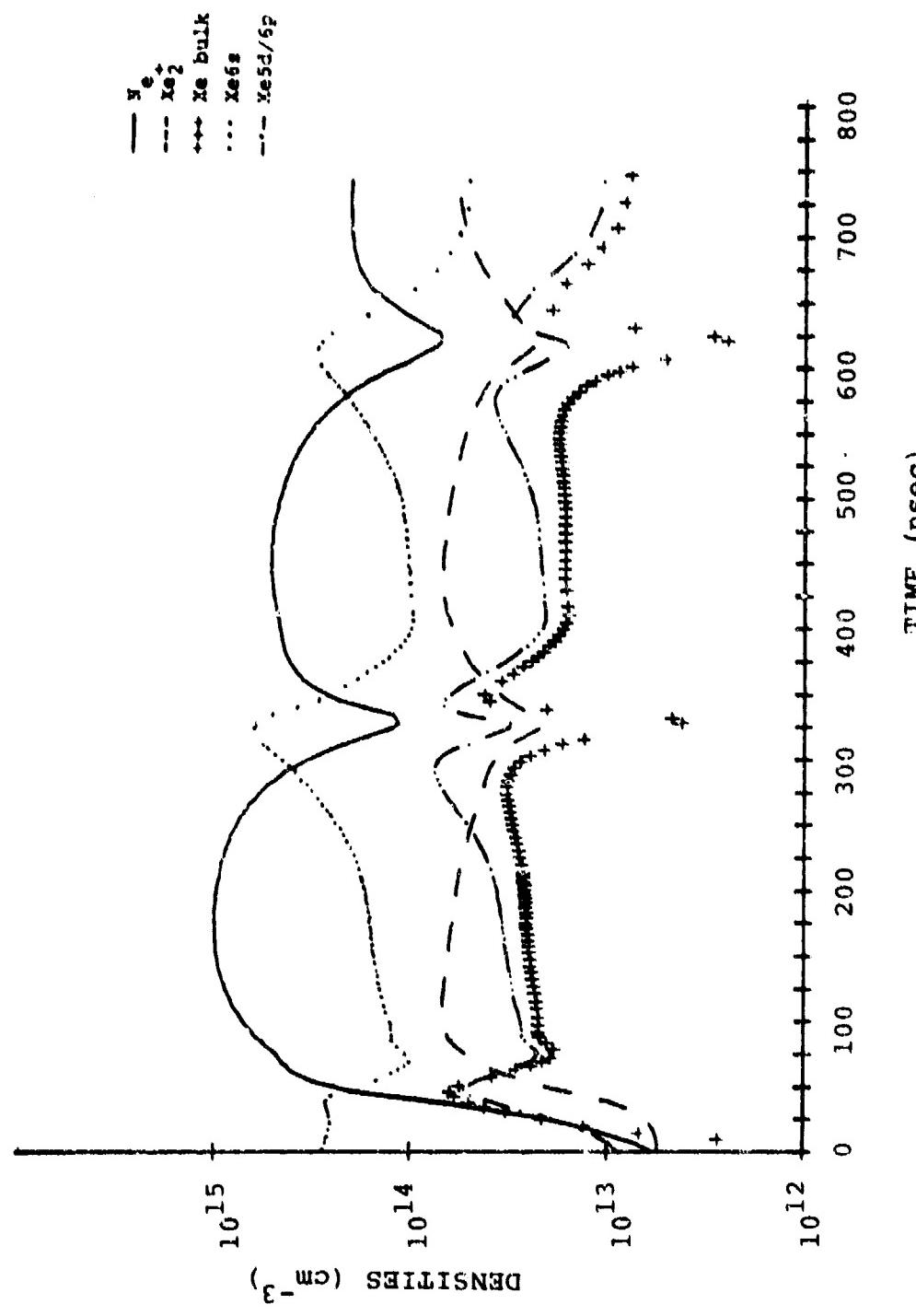
Figure 46. Density profiles resulting from Xe$_2^+$ and ArXe$^+$ recombination entirely into Xe6s.

125

recombination into Xe bulk, 104 mJ output for essentially

equal recombination into Xe bulk, Xe6s and Xe5d, and 98 mJ for

recombination into Xe6s. Although the densities differ in the

three plots it is clear that the basic recirculation pattern

is unaffected.

The best agreement to date between the model predictions

and experimental power profiles is shown in Figure 47, which

we have included in order to indicate the relative insensiti-

vity of the results to significant variations in the modeling.

The agreement is remarkably good considering the crudeness of

the model used in this particular case: The superelastic scat-

tering processes were dropped from the model, $ArXe^+$ as modeled

similarly to Xe_2^+ with no collisional dissociation and a .8:1:.1

branching ratio for recombination into the bulk, Xe5d and

Xe6p respectively. We see the initial sharp peak followed by

two very clear series of peaks - a taller series of broad

peaks with a smaller narrow series between. The amplitudes

of the tall series increases from the first to second peak and

then falls off, not unlike the behavior of the true series.

Figures 48 and 49 show some of the population densities

predicted by the modeling in this particular case. The most

significant differences from the previous modeling are that

the densities are now largest in the diatomic ions rather

than in Xe^+ and that the predominant neutral species is now

126
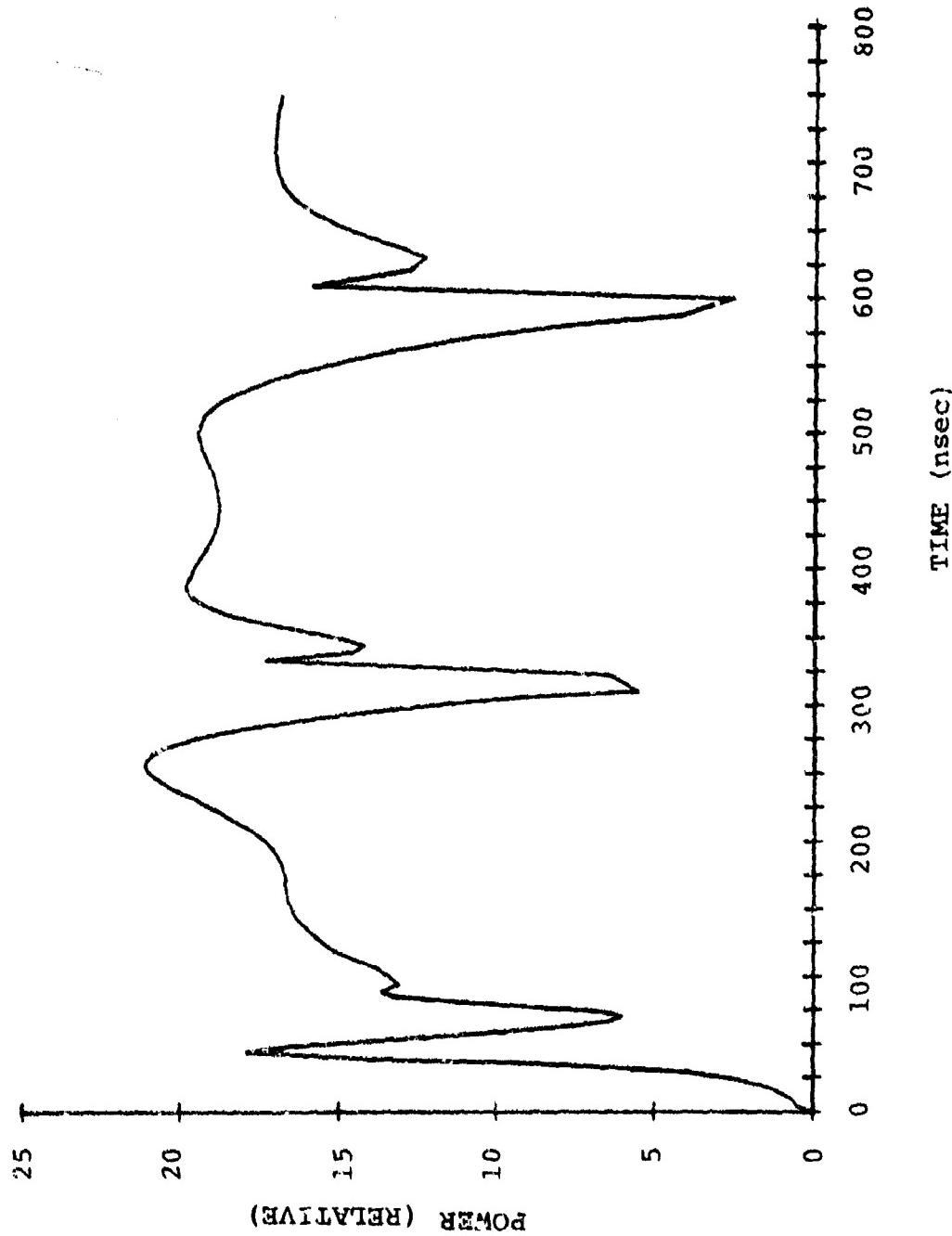
Figure 47. Power profiles obtained without superelastics, without collisional dissociation of ArXe[+] and with predominant Xe[+] and ArXe[+] dissociative recombination into Xe bulk.
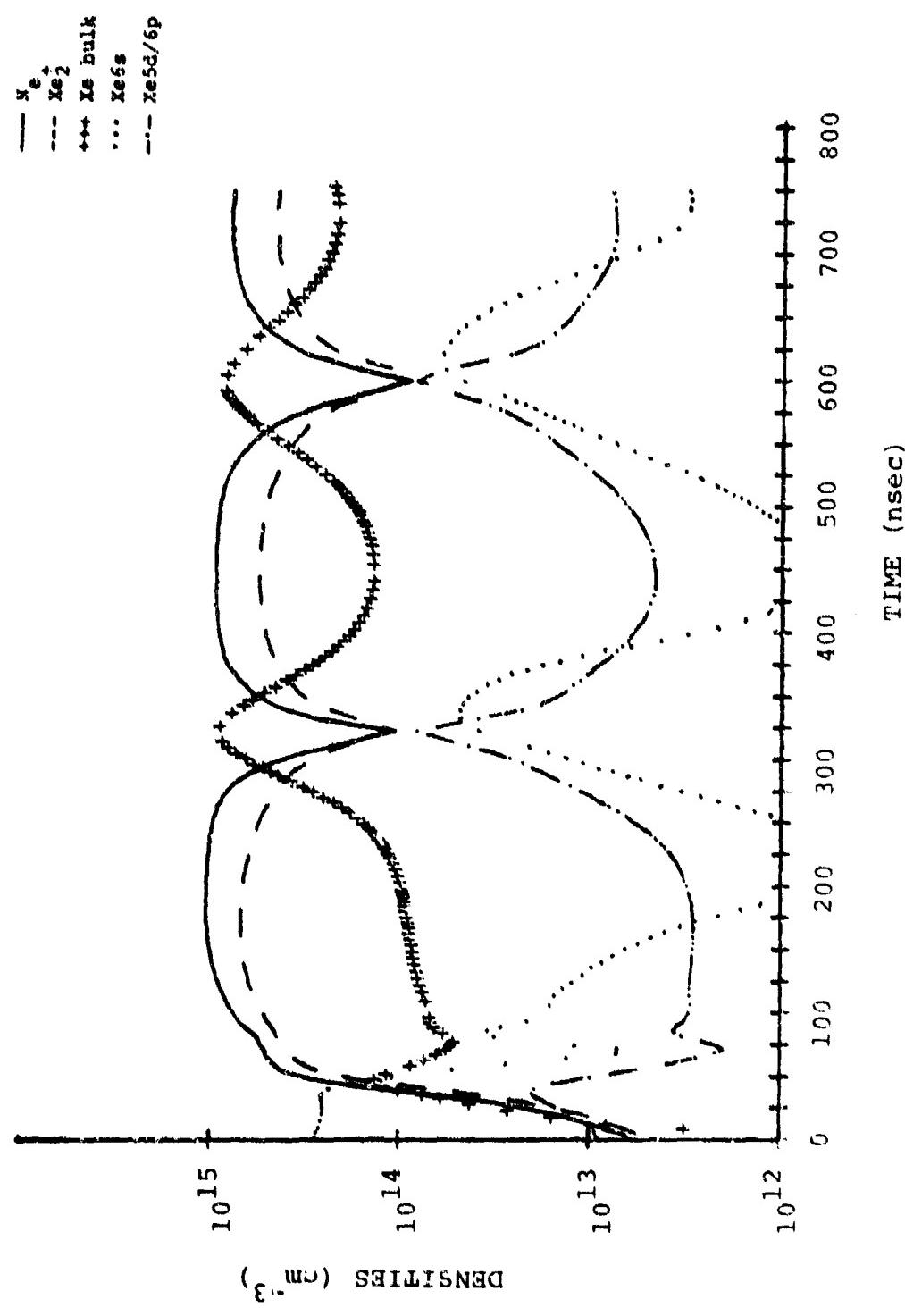
Figure 48. Density profiles corresponding to Figure 47.

128
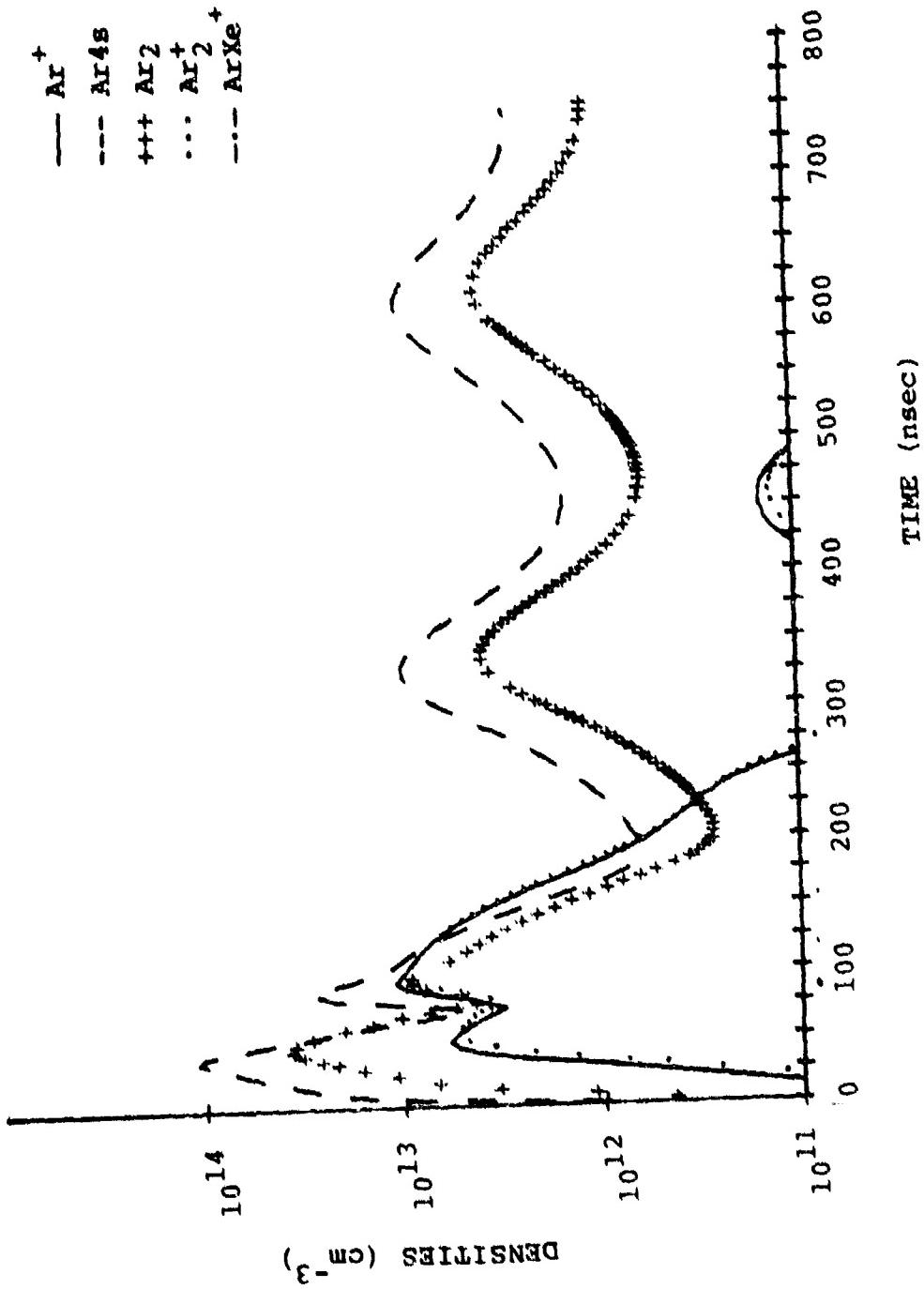
Figure 49. Density profiles corresponding with Figure 47.

Xe bulk rather than Xe6s. The increase in the molecular ion

densities is due to the assumption of no collisional dis-

sociation by Ar. The bulk populations increase because of the

larger molecular ion densities and because the rate of loss of

the bulk is reduced when superelastic collisions are ignored.

It is apparent from Figure 48 that there is still energy

recirculation in the discharge model, except that now the energy

is cycled primarily between the ions and the bulk levels, with

a fraction of the bulk states populating the lower xenon

levels by radiative cascade. Since the Xe6s fractional popu-

lation is now relatively small the loss of excited state energy

by Xe6s quenching is negligible, which is why the electron

density and total excited state population decays very slowly.

In fact in this modeling mode the duration of the power pulse

is determined by the rate of quenching of Xe bulk by Ar leading

to a loss via radiative decay of Ar_2^*.

Since Ar4s production by collisional quenching of Xe bulk

pulls energy out of the cycling xenon populations and does

not return it effeciently, Ar4s production is predicted to be

detrimental to the laser output. The rate constant used for

the reaction

$$Xe^{**} + Ar \rightarrow Ar4s + Xe$$

in this modeling is taken to be 2×10^{-4} times the reverse rate

measured by King et al.[22] As this rate is increased the excited

130

xenon populations are lost more rapidly. This results in a
faster decay of the oscillations in the laser output and a
decrease in the pulse energy. Figures 50 and 51 illustrate
the results of increasing the Xe bulk to argon transfer rates
by one and two order of magnitude respectively. The power
profiles decrease more rapidly with increased transfer to Ar.
Increasing the rate by an order ofmagnitude deceases the total
energy by 20%. A two order of magnitude increase, to .02 times
Setzer's reverse rate, decreases the output by 56%. It appears
that energy transfer into Xe5d from Xe bulk via Ar_2^* is suf-
ficiently less efficient than radiative cascade and superelastic
quenching that quenching of Xe bulk by argon will be detrimen-
tal to the laser. This may explain why larger ratios of argon
to xenon than 150:1 give less efficient lasing.
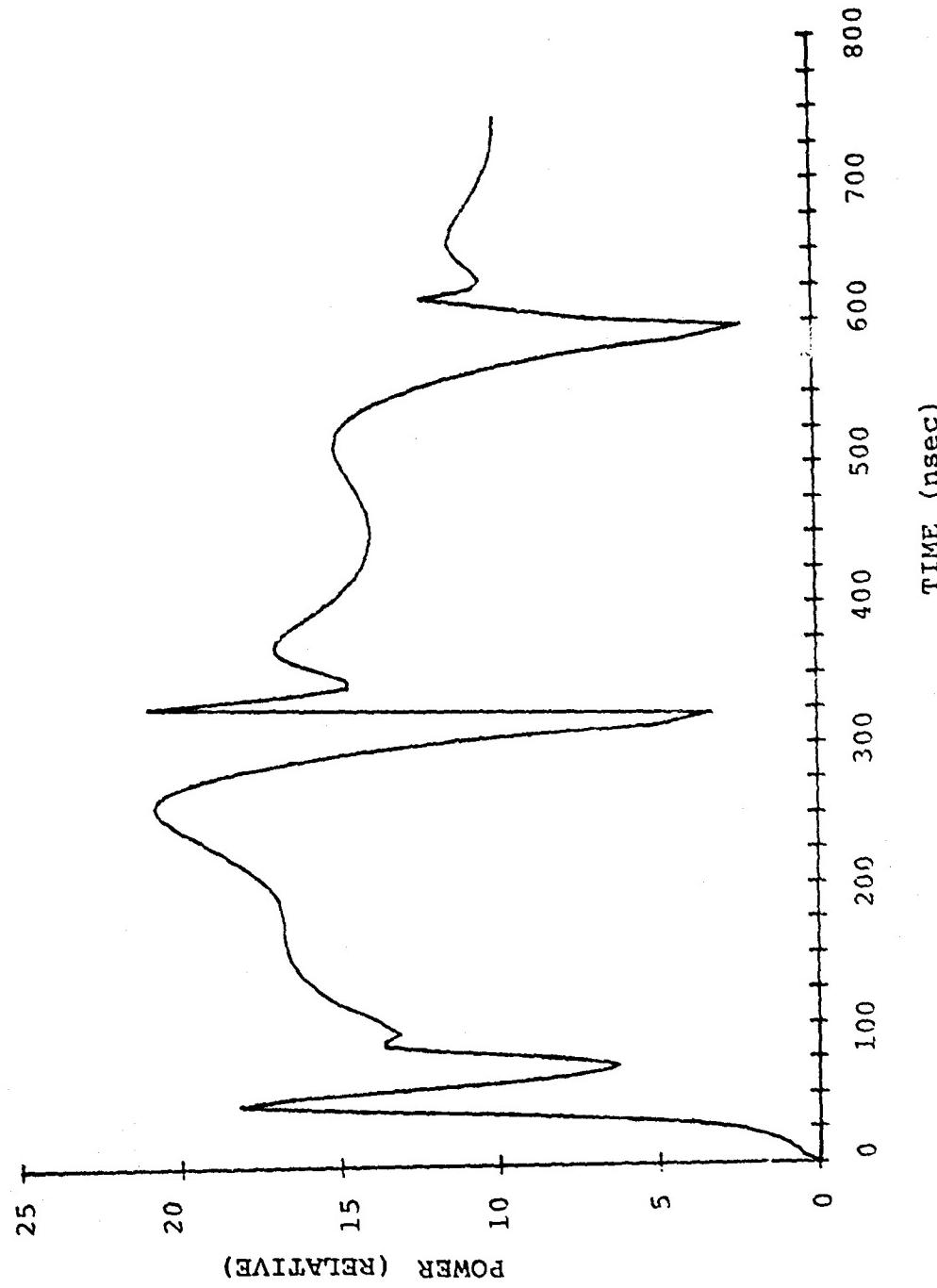
Figure 50. Power profiles obtained by increasing Xe bulk quenching rate by argon to 4×10⁻¹³ cm³ sec⁻¹. Compare with Figure 47.

132
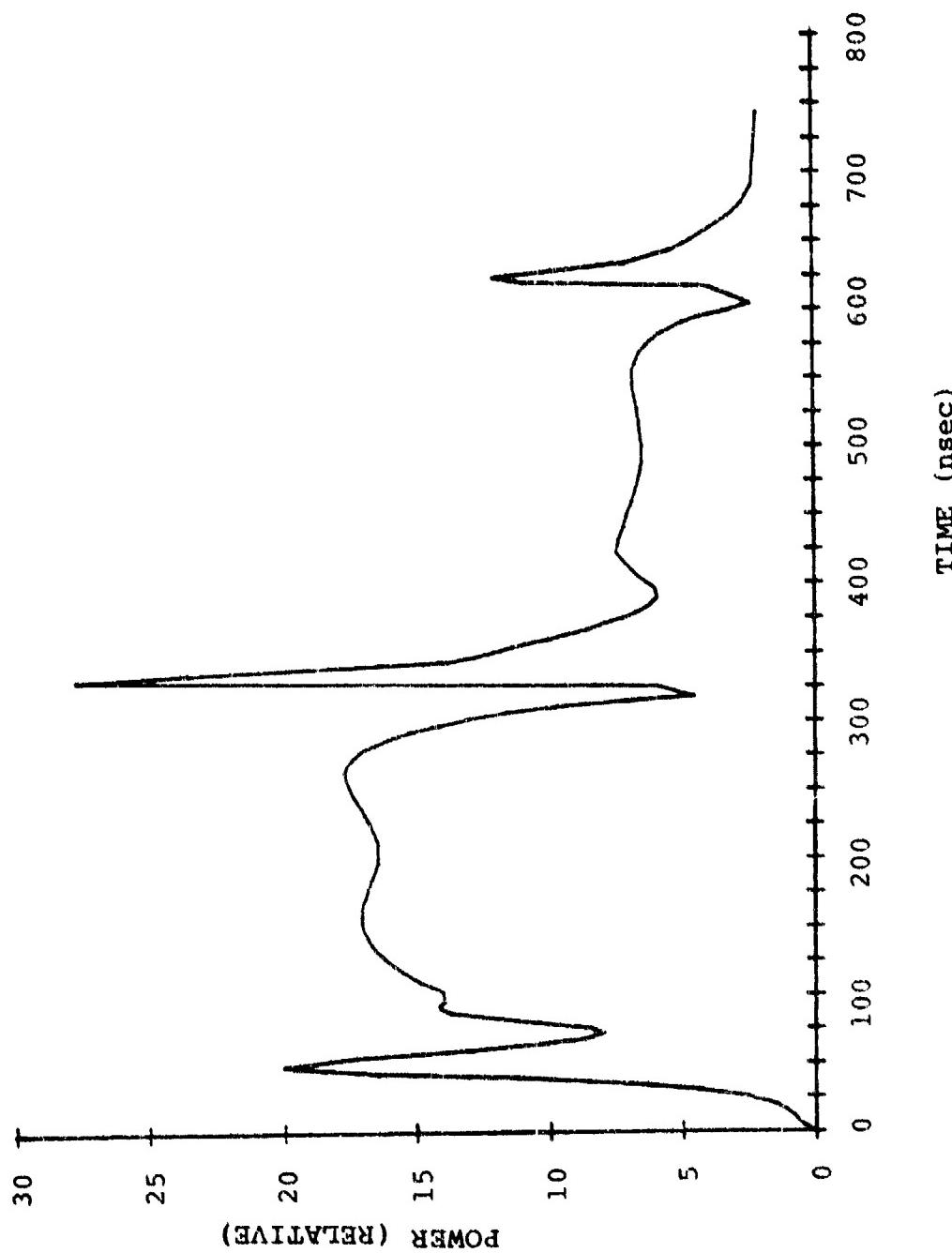
Figure 51. Power profiles obtained by increasing Xe bulk quenching rate by argon to 4×10^{-12} cm^3 sec^{-1}. Compare with Figure 47.

133

SECTION IV

THE HELIUM-XENON LASER

We have previously reported that lasing on the 5d→6p
transitions in helium/xenon mixtures yields much smaller
energies per pulse at pressures below one atmosphere than in
argon/xenon mixtures.[5] We have also noted that the dominant
laser line in helium/xenon mixtures is the 2.03 μm line,
which is the line expected to have the highest gain according
to our calculations of the 5d→6p transition probabilities. We
have now verified that these results are valid for pressures up
to 4 atmospheres. Although we have done no detailed modeling
of helium/xenon mixtures, we have made some experimental meas-
urements and calculations which suggest why this system is so
efficient.

In an e-beam preionized discharge there will be a signi-
ficant difference in the initial population densities in argon/
xenon and helium/xenon mixtures due to the very low stopping
power of helium for high energy electrons. Figure 52, which
was compiled from the NRL e-beam deposition data,[68] illustrates
the difference in energy deposition in our system for 200 keV
electrons in argon and in helium at 2 atmospheres and in xenon
at 2/150 atmosphere. The energy deposited into two atmospheres
of helium is an order of magnitude less than is deposited into
argon, and the resulting metastable and ion densities must

134
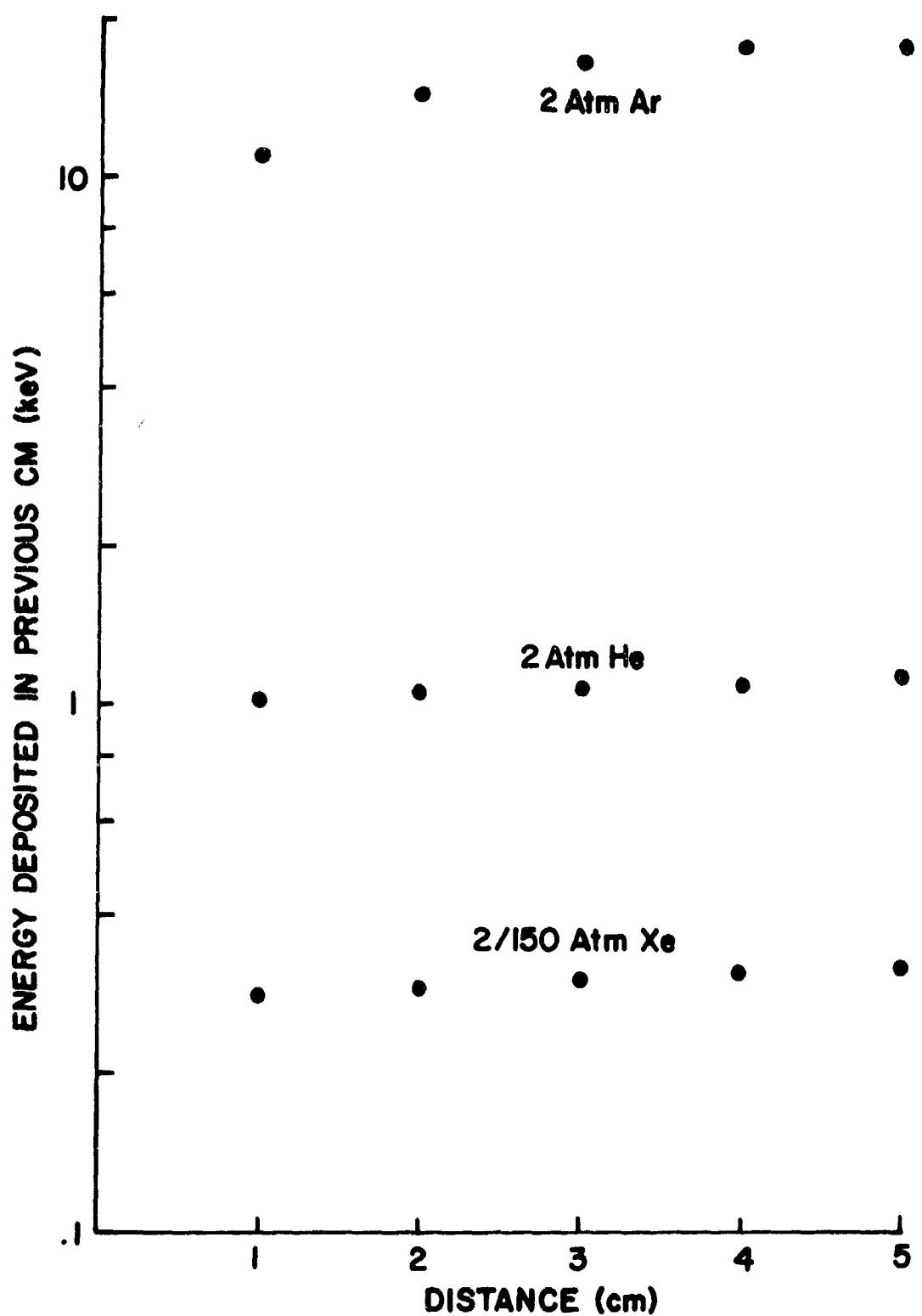
Figure 52. Energy deposited by 200 keV electrons into argon, helium and xenon.

therefore be at least an order of magnitude smaller. Thus
the initial electron density will be significantly smaller
in the helium mixture.

The kinetics of the helium/xenon system must necessarily
differ significantly from argon/xenon since the lowest excited
state of helium will Penning ionize xenon. Shuker, et al.[72]
in their analysis of low-pressure helium/xenon discharge
kinetics conclude that the dominant mechanism for populating
the laser levels is collisional-radiative recombination fol-
lowed by radiative cascade. The question arises as to whether
some kind of energy recirculation could occur here also.

Excitation rates and fractional power transfers were cal-
culated for a 150:1 ratio of He:Xe with ratios Xe^m/Xe = of 10^{-3}
and 10^{-2} and no metastable helium. This calculation was per-
formed for $3 \times 10^{-18} \leq E/N \leq 1.5 \times 10^{-17}$ volt-cm^2. The helium
momentum transfer cross sections were taken from Crompton et
al.[73] and the helium excitation cross sections were from
Schulz and Fox,[74] although since the electron energy distri-
bution function decreased rapidly at higher energies the helium
excitation cross sections did not affect the results of the cal-
culations. The choice of a 150:1 ratio of helium to xenon was
made since the work of Olson and Grosjean[4] indicates the highest
laser power for ratios between 100 and 200:1.

The Boltzmann code calculations shown in Figures 53 and 54 predict that for $E/N < 1.5 \times 10^{-17}$ volt-cm^2 at least 90% of the power is dissipated in elastic scattering. This is significantly different from the results of similar calculations in argon, shown in Figures 22-24. We can attribute this difference to the lack of a Ramsauer minimum in the total scattering cross section in helium which results in a larger scattering cross section than in argon over the energy range from .01 to 5.5 eV. Because of the excessive scattering of lower energy electrons in helium, the electron energy distribution function falls off rapidly at higher energies and as a result the excitation rates calculated for all processes for $Xe^m/Xe = 10^{-3}$ are one to two orders of magnitude lower in helium/xenon than in argon/xenon mixtures. Thus we would not expect efficient reexcitation of any Xe6s atoms produced in the discharge.

For an E/N of 3×10^{-18} volt-cm^2 the calculations indicate that the electron drift velocities in the helium/xenon and argon/xenon mixtures are both about 3×10^5 cm sec^{-1} whereas for an E/N of 1.5×10^{-17} volt-cm^2 the drift velocity in argon/xenon was an order of magnitude greater than that for helium/xenon, 6×10^5 cm^3 sec^{-1}. This result indicates that the current and voltage in a helium-xenon discharge circuit will damp out faster due to an increased gas impedance. This has been verified by observations of the helium/xenon discharge.

137
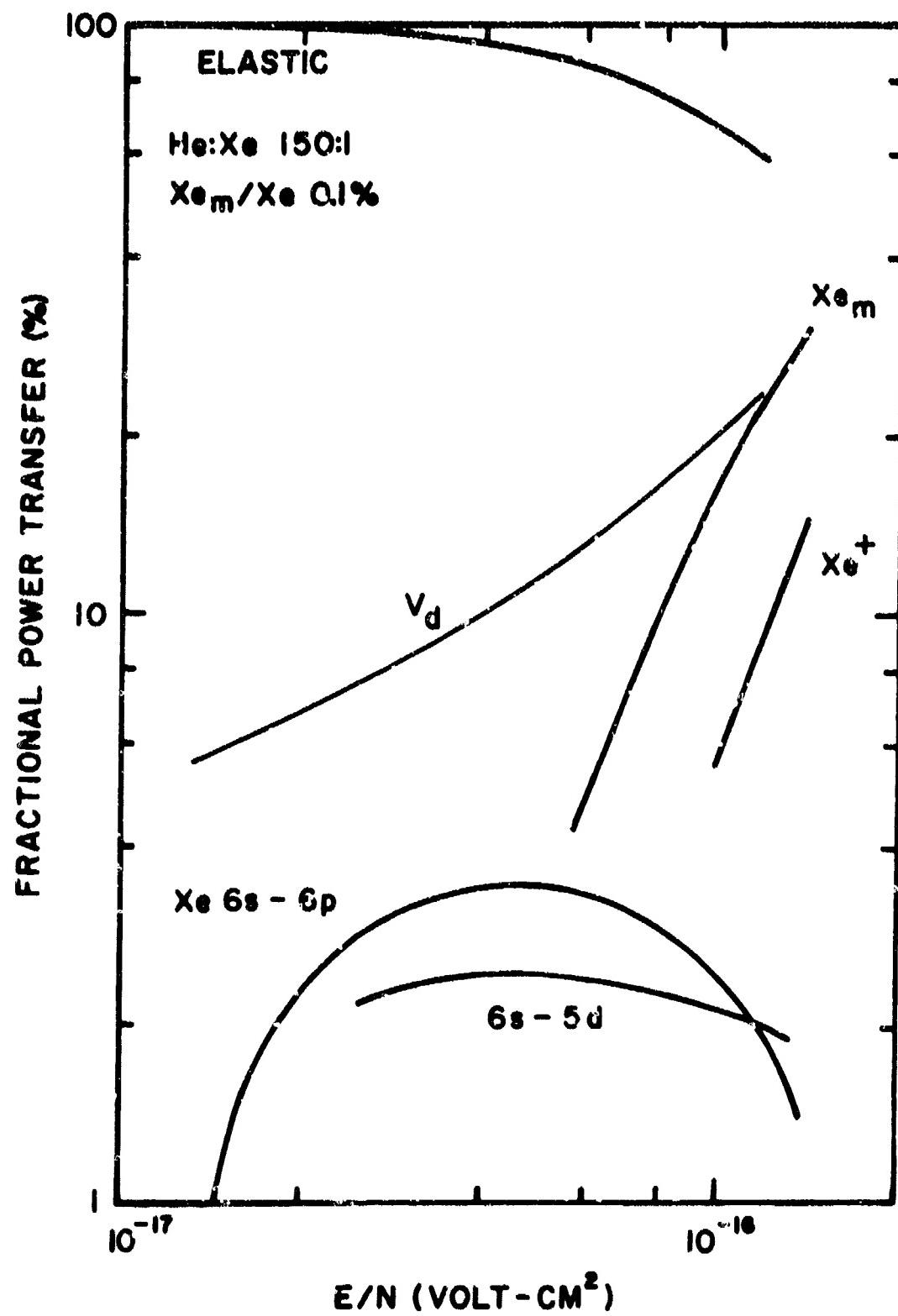
Figure 53. Power transfer and drift velocity curves for a 150:1 He/Xe mixture with Xe6s/Xe = 10^{-3}.
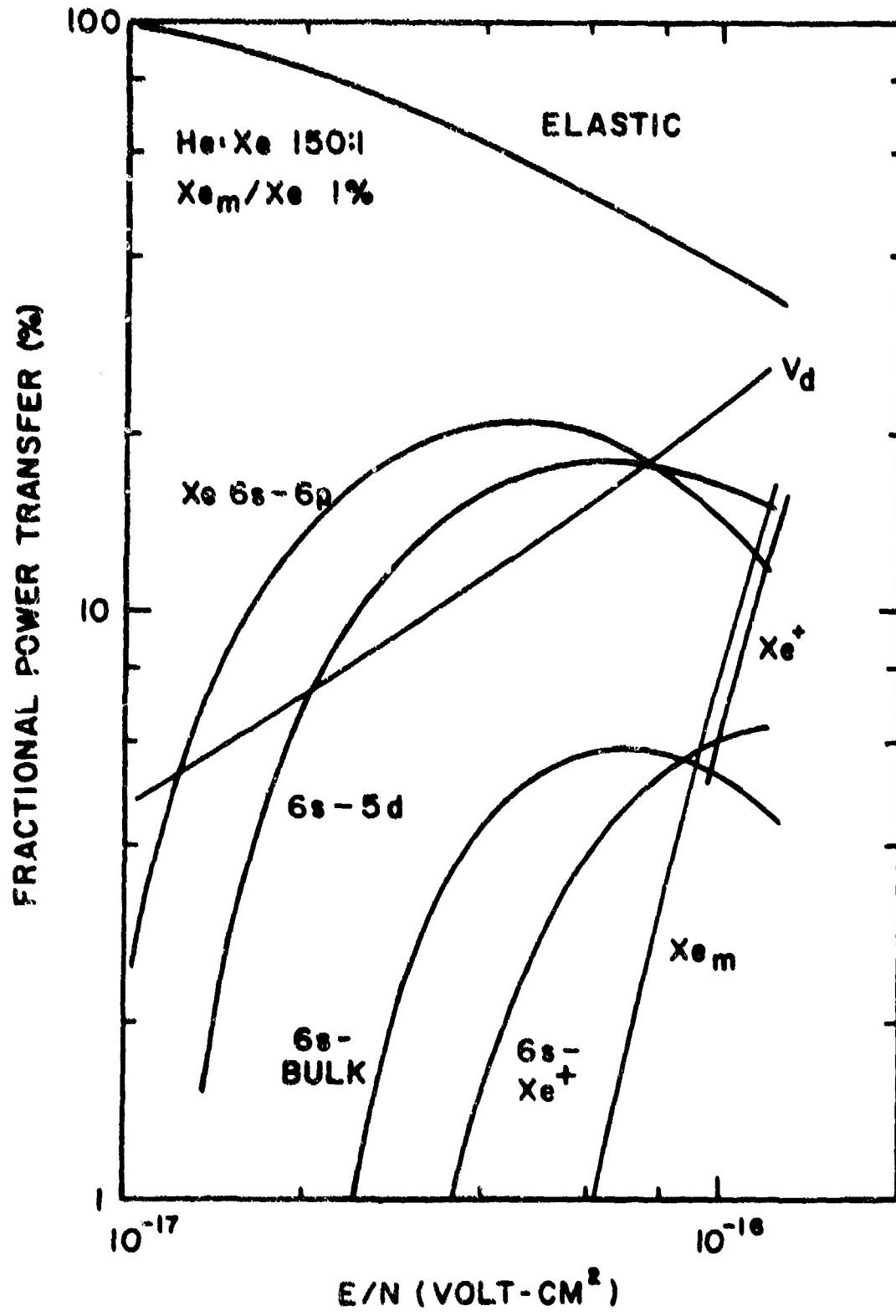
Figure 54. Power transfer and drift velocity curves for a 150:1
He/Xe mixture with Xe6s/Xe = 10^{-2}.

139

Figure 54 illustrates the total energy per pulse for a
124:1 ratio of helium to xenon as a function of total pres-
sure. Unlike the results for argon/xenon shown in Figure 30
the energy per pulse is relatively constant between 1 and 3
atmospheres and does not exceed ~ 11 mJ. Inserting a silicon
flat output coupler into the laser cavity will increase the
energy by ~ 50%.

Correlated measurements of the discharge current and
voltage and total laser output are shown in Figure 55 for a
150:1 helium/xenon mixture at 1 atmosphere total pressure and
an initial sustainer voltage of 23 kvolts. The current and
voltage curves are similar to those for argon/xenon, Figure 10,
except for the faster decay. The power output curve consists
predominantly of a single initial spike followed by a series
of very small spikes which together contain less than 10% of
the total energy. The laser output is on two lines only, 2.03
μm and 2.65 μm with 65% of the energy at 2.03 μm.

The time correlation of the power and discharge voltage
indicates that aside from the first initial peak, the laser
output is composed of spikes which immediately follow the
points of lowest E/N. This information is useful in formula-
ting a model for the system. The first power peak is undoubtedly
due to direct excitation of the xenon 5d levels along with radi-
ative cascade from higher excited states. Such a process is

140
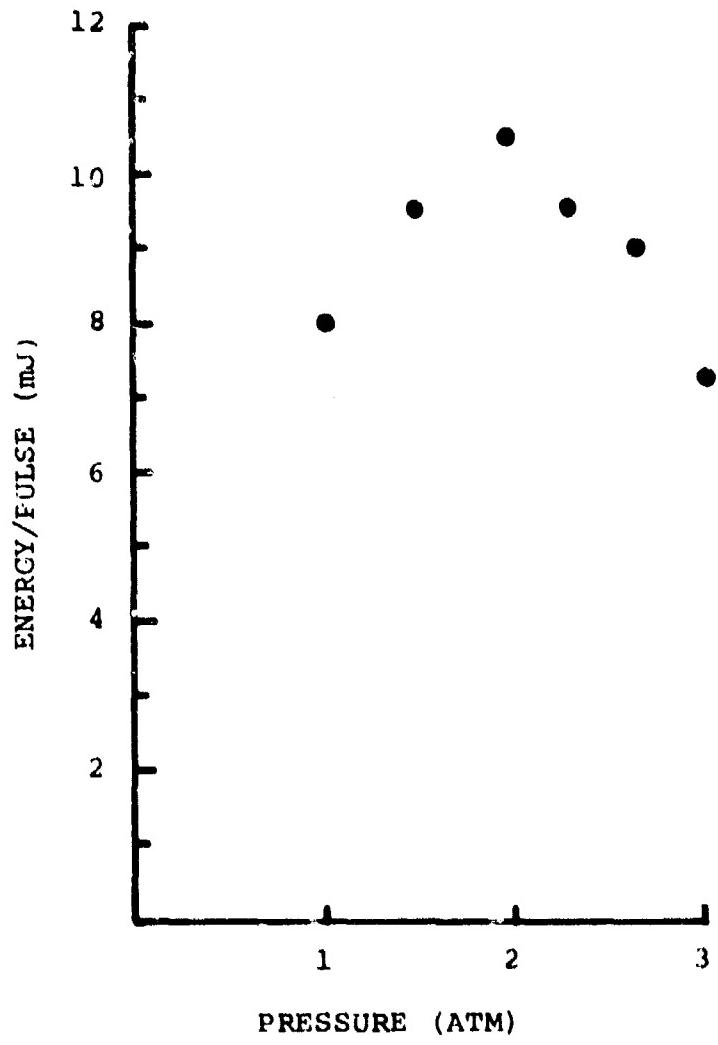
Figure 55. Total laser energy/pulse versus total pressures for a 124:1 He/Xe mixture.

141

consistent with the initial high E/N values of $\sim 1.5 \times 10^{-16}$ volt-cm^2. If we adopt Shuker's[72] explanation of the helium/xenon kinetics, then during the subsequent period of low E/N a reservoir of Xe$^+$ ions will be created via Penning ionization from helium atoms and molecules, and the neutral xenon states will be populated by collisional radiative recombination of Xe$^+$. The rate of collisional radiative recombination is temperature dependent so that the recombination will proceed faster for lower values of E/N. Additionally, since the recombination will be predominantly into the very highly excited states of Xe**, the neutrals produced by recombination will be more rapidly ionized at the higher E/N values. These considerations would indicate that the laser levels will be populated by recombination and radiative cascade only during the low E/N portions of the discharge, as observed in the series of spikes.

Since the current profile indicates that the electron and ion densities do not fall off as rapidly as the amplitude of the power peaks there must be some mechanism other than depletion of the ion populations which causes the laser to emit only one strong pulse. We believe that one mechanism may be radiative trapping of the 6p → 6s transition due to a large Xe6s density. The rate of depletion of Xe6s may be very slow since the HeXe* molecule will be very shallowly bound and

142

thereby subject to rapid collisional dissociation and because, due to its light mass, helium will be an inefficient third body for Xe_2^* production. As the discharge progresses the Xe6s population will increase resulting in a rapid reduction in the amplitude of each successive peak.

We can obtain some information about the likelihood of radiative trapping of the $6p(5/2)_2$ to 6s transition by observing the intensities of the fluorescence of the 9923 $\overset{o}{A}$, $6p(5/2)_2 \rightarrow 6s(3/2)_1$, and the 9045 $\overset{o}{A}$, $6p(5/2)_2 \rightarrow 6s(3/2)_2$, transitions. Calculations of the transition probabilities of these two lines based on the Coulomb model of Bates and Damgaard indicate an intensity ratio of 88:12 for 9923:9045 $\overset{o}{A}$. Measurements of the actual relative intensities show them to be approximately equal for most of the discharge and that initially the 9045 $\overset{o}{A}$ fluorescence is more intense. We attribute this anamolous behavior to trapping of at least the 9923 $\overset{o}{A}$ line.

We have made measurements of the fluorescence from a number of excited states in helium/xenon for comparison with the corresponding fluorescence in argon/xenon. In general the fluorescence is short-lived compared with that in argon/xenon and there is little structure on the fluorescence, unlike the highly modulated fluorescence in argon/xenon.

Figure 56 illustrates the time dependence of the fluorescence from the $6p(5/2)_2$ to $6s(3/2)_2$ transition at 9045 $\overset{o}{A}$. The first peak in both curves is due to fluorescence from e-beam

143
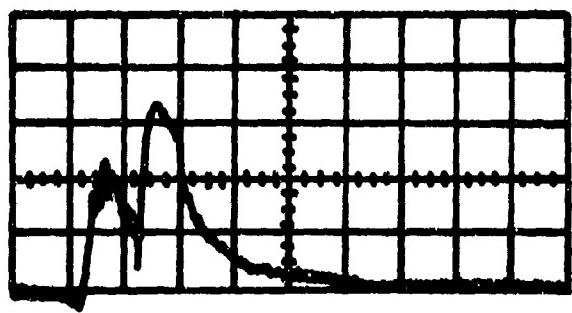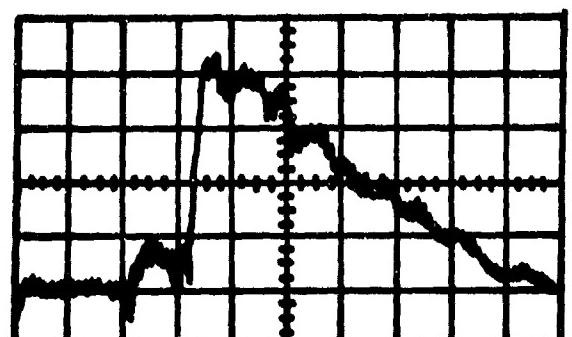
HeXe

500 nsec/div.

Ar-Xe

500 nsec/div.

Figure 56. Fluorescence profiles of the 9045 Å emission from the $6p(5/2)_2 - 6s(3/2)_2$ transition in xenon. The top curve is the fluorescence from a 124:1 He:Xe mixture at 2.4 atm. The bottom curve is the fluorescence from a 150:1 Ar/Xe mixture at 1 atm.

144

pumping alone and the second peak is due to the sustained discharge which began $\sim$ 500 nsec after the e-beam was initiated. The fluorescence from the 6p-6s transitions in helium/xenon typically exhibit comparable intensities on the e-beam pump and on the sustainer discharge. None of the xenon 6p-6s fluorescence lines exhibit the long-lived, high-modulated emission observed in argon/xenon mixtures.

It is apparent that the xenon excited state populations are depleted more rapidly in helium than in argon. The lack of a modulated fluorescence is consistent with the Boltzmann code calculation which predicted negligible power available for excitation of Xe6s. Since energy recirculation therefore is not a significant process in helium/xenon mixtures the helium/xenon laser will not operate as efficiently as the argon/xenon laser.

REFERENCES

1. R. Targ and M.W. Sasnett, "Xenon-Helium Laser at High Pressure and High Repetition Rate," Appl. Phys. Lett. 19, 537-539 (1971).

2. T.S. Fahlen and R. Targ, "High-Average-Power Xenon Laser," IEEE J. Quantum Electron. QE-9, 609 (1973).

3. P.L. Chapovsky, V.N. Lisitsyn and A.R. Sorokin, "High-Pressure Gas Lasers on ArI, XeI and KrI Transitions," Opt. Commun. 16, 33-36 (1976).

4. R.A. Olson and D.F. Grosjean, "Closed-Cycle Rare-Gas Electrical-Discharge Laser," (Systems Research Laboratories, Inc. AFAPL-TR-77-13, 1977).

5. L.A. Newman and T.A. DeTemple, "High Pressure Infrared Ar-Xe Laser System: Ionizer-Sustainer Mode of Excitation," Appl. Phys. Lett. 27, 678-680 (1975).

6. N. Sadeghi and J. Sabbagh, "Collisional Transfer Between the $6s'(1/2)_{0,1}$ and $6p(1/2)_1$ Xenon Levels," Phys. Rev. A16, 2336-2345, (1977).

7. C.W. Werner, E.V. George, P.W. Hoff and C.K. Rhodes, "Radiative and Kinetic Mechanisms in Bound-Free Excimer Lasers," IEEE J. Quantum Electron. QE-13, 769-783 (1977).

8. R.S. Mulliken, "Potential Curves of Diatomic Rare-Gas Molecules and Their Ions, with Particular Reference to Xe_2^*," J. Chem. Phys. 52, 5170-5180 (1970).

9. M.A. Heald and G.B. Wharton, Plasma Diagnostics with Microwaves (John Wiley, New York, 1965).

10. D.R. Bates and A. Damgaard, "The Calculation of the Absolute Strengths of Spectral Lines," Phil. Trans. Roy. Soc. (London) 242, 101-122 (1949).

11. L.S. Frost and A.V. Phelps, "Rotational Excitation and Momentum Transfer Cross Sections for Electrons in H_2 and N_2 from Transport Coefficients," Phys. Rev. 127, 1621-1633 (1962).

12. A.G. Englehardt and A.V. Phelps, "Elastic and Inelastic Collisional Cross Sections in Hydrogen and Deuterium from Transport Coefficients," Phys. Rev. 131, 2115-2128 (1963).

13. L.S. Frost and A.V. Phelps, "Momentum Transfer Cross
     Sections for Slow Electrons in He, Ar, Kr and Xe from
     Transport Coefficients," Phys. Rev. 136, A1538-A1545
     (1964).

14. D. Rapp and P. Englander-Golden, "Total Cross Sections
     for Ionization and Attachment in Gases by Electron Impact.
     I. Positive Ionization," J. Chem. Phys. 43, 1464 (1965).

15. A.J. Dixon, M.F.A. Harrision, and A.C.H. Smith, Abstracts
     of Papers of the Eighth International Conference of the
     Physics of Electronic and Atomic Collisions, ed. by B.C.
     Čobić and M.V. Kurepa (Institute of Physics, Belgrade,
     Yugoslavia, 1973), vol. 1, p. 405 (Reproduced in Refer-
     ence 16).

16. Estimated from D. Ton-That and M.R. Flannery, "Cross Sec-
     tions for Ionization of Metastable Rare-gas Atoms (Ne*,
     Ar*, Kr*, Xe*) and of metastable N$_2^*$, CO* Molecules by
     Electron Impact," Phys. Rev. A15, 517-526 (1977).

17. M. Schaper and H. Scheibner, "Absolute Determination of the
     Total Excitation Cross Sections of the Noble Gases by Elec-
     tron Impact," Beit. Plasma Phys. 9, 45-57 (1969).

18. M. Gryzinski, "Classical Theory of Atomic Collisions. I.
     Theory of Inelastic Collisions," Phys. Rev. 138, A336-
     A358 (1965).

19. E. Bauer and D. Bartky, "Calculation of Inelastic Electron-
     Molecule Collision Cross Section by Classical Methods,"
     J. Chem. Phys. 43, 2466-2476 (1965).

20. J. LeCalve and M. Bourene, "Pulsed Radiolysis of Argon-
     Nitrogen Mixtures. Measurement of the Metastable Argon
     De-excitation by Nitrogen," J. Chem. Phys. 58, 1446-1451
     (1973).

21. P.K. Leichner, E.T. Hall and K.E. Palmer, "Collisional and
     Radiative Excitation Transfers in Ar-Xe Mixtures," sub-
     mitted to Phys. Rev. A.

22. D.L. King, L.G. Piper and D.W. Setser, "Electronic Energy
     Transfer from Metastable Argon (4s $^3P_{0,2}$) to Xenon, Oxygen
     and Chlorine Atoms," J. Chem. Soc. Farad. Trans. II, 73,
     177-200 (1977).

147

23. Estimated from R. Johnson, J. McDonald and M.A. Biondi, "Thermal Energy Charge Transfer Rates from Ne^+, Ne_2^+, Ar^+ and Ar_2^+ Ions with Kr and Xe Atoms," to be published.

24. E. McDaniel, A. Dalgarno, E. Ferguson and L. Friedmann, _Ion-Molecule Reactions_ (Wiley-Interscience, New York) 1970, p. 338.

25. Estimated from B. Mahan, "Mechanism for Ion-Neutral Association Reactions," _J. Chem. Phys._ **43**, 3080-3082 (1965), and D.S. Smith, A. Dean and C. Plumb, "Three Body Conversion Reactions in Pure Rare Gases," _J. Phys. B_ **5**, 2134-2142 (1972).

26. Estimated from D.K. Bohme, N.G. Adams, M.M. Mosesman, D.B. Dunkin and E.E. Ferguson, "Flowing Afterglow Studies of the Reactions of the Rare-Gas Molecular Ions He_2^+, Ne_2^+, and Ar_2^+ with Molecules and Rare-Gas Atoms," _J. Chem. Phys._ **52**, 5094-5101 (1970).

27. Estimated from P. Kebarle, R.M. Haynes, S.K. Searles, "Mass Spectrometric Study of Ions in Xe, Kr, Ar, Ne at Pressures up to 40 torr: Termolecular Formation of the Rare-Gas Molecular Ions. Bond Dissociation Energy of Ar_2^+ and Ne_2^+," _J. Chem. Phys._ **47**, 1684-1691 (1967).

28. W.F. Liu and D.C. Conway, "Ion-Molecule Reactions in Ar at 296, 195, and 77°K," _J. Chem. Phys._ **62**, 3070-3073 (1965).

29. C.W. Werner, E. Zamir and E.V. George, "Pressure Dependence of the Electron Density in Electron-Beam-Excited Rare-Gas Plasmas," _Appl. Phys. Lett._ **29**, 236-239 (1976).

30. M. Rokni, J.H. Jacob, and J.A. Mangano, "Absorption in Ne- and Ar-Rich XeF^* Laser Mixtures," _Appl. Phys. Lett._ **32**, 622-623 (1978).

31. Calculated from $ArXe^+$ potential energy curves of H. Powell, A. Szöke and N. Winter, "Spectroscopy and Kinetics of Mixed Rare-Gas Ions," 10th International Quantum Electronics Conference, Atlanta, 1978.

32. H. Helm, "Formation of Xe_3^+ Ions in Xenon at Temperatures Between 210 and 293°K," _Phys. Rev._ **A14**, 680-684 (1976).

33. Estimated from References 29 and 32.

34. Y. Shiu and M.A. Biondi, "Dissociative Recombination in Argon: Dependence of the Total Rate Coefficient and Excited-State Production on Electron Temperature," <u>Phys. Rev.</u> A. (1978) to be published.

35. J.N. Bardsley and M.A. Biondi, "Dissociative Recombination," in <u>Advances in Atomic and Molecular Physics</u>, (Academic Press, New York) 1970, Vol. 6, p. 1.

36. J.N. Bardsley, private communication.

37. Y. Shiu, M.A. Biondi and D.P. Sipler, "Dissociative Recombination in Xenon: Variation of the Total Rate Coefficient and Excited-State Production with Electron Temperatures," <u>Phys. Rev.</u> A15, 494-498 (1977).

38. 10^{-26} cm^3 sec^{-1} at 300°K with a $T_e^{-5/2}$ dependence: H.S.W. Massey, E.H.S. Burhop and H.B. Gilbody, <u>Electronic and Ionic Impact Phenomena</u>, Vol. III (Oxford University Press, London, 1971).

39. 10^{-12} cm^3 sec^{-1} at 300°K with a $T_e^{-.7}$ dependence: M. Biondi in <u>Principles of Laser Plasmas</u>, ed. by G. Bekefi (Wiley Interscience, New York, 1976) p. 128.

40. R. Gutcheck and E. Zipf, "Collision Deactivation of Metastable Ar($^3P_{0,2}$) Atoms and N$_2$(A$^3\Sigma_u^+$) Molecules," <u>Bull. Am. Phys. Soc.</u> 17, 395 (1972).

41. R.M. Hill, R.A. Gutcheck, D.L. Huestis, D. Mukherjee and D.C. Lorents, "Studies of E-beam Pumped Molecular Lasers," (SRI International, Technical Report MP74-39, 1974).

42. A. Fontijn, "Recent Progress in Chemi-Ionization Kinetics," <u>Pure and Appl. Chem.</u> 39, 287-306 (1974).

43. Estimated to be gas kinetic.

44. Taken to be rate of Ar$_2^*$ + Ar$_2^*$.

45. C. Klots and L. Sieck, "Argon Sensitized Formation of Xe$_2^+$: A New Mechanism for the Jesse Effect," <u>Chem. Phys. Lett.</u> 27, 71-72 (1974).

46. A. Johnson and J. Gerardo, "De-Excitation Rates for Excited Xenon Molecules," <u>J. Chem. Phys.</u> 59, 1738-1741 (1973).

47. Assumed to be same as the rate for the corresponding ion reaction.

48. J. Keto, R. Gleason and G. Walters, "Production Mechanisms and Radiative Lifetimes of Argon and Xenon Molecules Emitting in the Ultraviolet," Phys. Rev. Lett. 33, 1365-1368 (1974).

49. T.D. Nguyen and N. Sadeghi, "Rate Coefficients for Collisional Population Transfer Between $3p^54p$ Argon Levels at 300°K," Phys. Rev. A, (1978) to be published.

50. Estimated from rates in Reference 22.

51. J. Gerardo and A.W. Johnson, "Formation and Decay of Xenon Dimers in Photo-Excited Xenon and Xenon-Noble Gas Mixtures," 28th Gaseous Electronics Conference, Rolla, Missouri, 1975.

52. R.I. Rudko and C.L. Tang, "Spectroscopic Studies of the Ar^+ Laser," J. Appl. Phys. 38, 4731-4739 (1967).

53. D.C. Lorents, D.J. Eckstrom and D.L. Huestis, "Excimer Formation and Decay Processes in Rare Gases," (SRI International, Technical Report MP73-7, 1973).

54. T. Oka, K.R. Rao, J. Redpath and R. Firestone, "Mechanisms for the Decay and Spontaneous Radiative Decay Constants of the Lowest-lying Attractive Excited States of Ne_2, Ar_2 and Kr_2," J. Chem. Phys. 61, 4740-4746 (1974).

55. R.E. Gleason, T.D. Bonifield, J.W. Keto and G.K. Walters, "Electronic Energy Transfer in Argon-Xenon Mixtures Excited by Electron Bombardment," J. Chem. Phys. 66, 1589-1593 (1977).

56. O. Cheshnovsky, B. Raz and J. Jortner, "Electronic Energy Transfer in Rare Gas Mixtures," J. Chem. Phys. 59, 3301-3307 (1973).

57. P. Moerman, R. Boucique and P. Mortier, "Pressure Dependent Decay of the Ultraviolet Continuum of Argon," Phys. Lett. 49A, 179-180 (1974).

58. H.T. Powell and A. Szöke, "Kinetics of E-beam Excited Ar/Xe Mixtures," 30th Gaseous Electronics Conference, Palo Alto, CA, 1977.

59. D.W. Setser, "Excited State Reaction Kinetics," 30th Gaseous Electronics Conference, Palo Alto, CA, 1977.

60. H. Statz, C.L. Tang and G.F. Koster, "Approximate Electromagnetic Transition Probabilities and Relative Electron Excitation Cross Sections for Rare-Gas Masers," J. Appl. Phys. 34, 2625-2632 (1963).

61. L. Allen, D.G.C. Jones and D.G. Schofield, "Radiative Lifetimes and Collisional Cross Sections for XeI and II," J. Opt. Soc. Am. 59, 842-847 (1969).

62. M.J. Seaton, "The Impact Parameter Method for Electron Excitation of Optically Allowed Atomic Transitions," Proc. of Phys Soc. 79, 1105-1117 (1962).

63. H.E. Saraph, "Cross Sections for n→n+1 Transitions in Hydrogen Produced by Electron Impact," Proc. Phys. Soc. 83, 763-768 (1964).

64. C.W. Gear, "The Automatic Integration of Ordinary Differential Equations," Comm. ACM, 14, 176-179 (1971).

65. J.D. Cobine, Gaseous Conductors (Dover, New York, 1958) p. 217.

66. M.J. Berger and S.M. Seltzer, "Tables of Energy Losses and Ranges of Electrons and Positons," NASA Report No. SP 3012 (1964).

67. L.R. Peterson and J.E. Allen, Jr., "Electron Impact Cross Sections for Argon," J. Chem. Phys. 56, 6068-6076 (1972).

68. "DARPA-NRL Laser Program Semiannual Technical Report to Defense Advanced Research Projects Agency, 1 April 1977-30 September 1977," NRL Memorandum Report 3753 (1978).

69. Y. Tanaka, K. Yoshimo and D.E. Freeman, "Emission Spectra of Heteronuclear Diatomic Rare Gas Positive Ions," J. Chem. Phys. 62, 4484-4496 (1975).

70. C.J. Chen, "Collisional-radiative Electron-ion Recombination Rate in Rare-Gas Plamas," J. Chem. Phys. 50, 1560-1566 (1969).

71. A. Gilardini, Low Energy Electron Collisions in Gases, (Wiley-Interscience, New York, 1972). p. 337.

72. R. Shuker, Y. Binur and A. Szöke, "Studies of Afterglows in Noble-gas Mixtures: A Model for Energy Transfer in He/Xe$^+$," Phys. Rev. $\underline{A12}$, 515-521 (1975) and R. Shuker, A. Szöke, E. Zamir and Y. Binur, "Energy Transfer in Noble-gas Mixtures: Penning Ionization in He/Xe," Phys. Rev. $\underline{A11}$, 1187-1192 (1975).

73. R.W. Crompton, M.T. Elford and A.G. Robertson, "The Momentum Cross Section for Electrons in Helium Derived from Drift Velocities at 77°K," $\underline{Aust.\ J.\ Phys.}$ $\underline{23}$, 667-681 (1970).

74. G.T. Schulz and R.E. Fox, "Excitation of Metastable Levels in Helium Near Threshold," Phys. Rev. $\underline{106}$, 1179-1181 (1957).